Virginia Commonwealth University
VCU Scholars Compass

Theses and Dissertations

Graduate School

2012

# Efficiency droop mitigation and quantum efficiency enhancement for nitride Light-Emitting Diodes

Xing Li
*Virginia Commonwealth University*

Follow this and additional works at: https://scholarscompass.vcu.edu/etd

Part of the Engineering Commons

© The Author

Downloaded from
https://scholarscompass.vcu.edu/etd/395

This Dissertation is brought to you for free and open access by the Graduate School at VCU Scholars Compass. It has been accepted for inclusion in Theses and Dissertations by an authorized administrator of VCU Scholars Compass. For more information, please contact libcompass@vcu.edu.

VIRGINIA COMMONWEALTH UNIVERSITY

# *Efficiency droop mitigation and quantum efficiency enhancement for nitride Light-Emitting Diodes*

A research dissertation submitted in partial fulfillment of the requirements for the degree
of Doctor of Philosophy in Electrical and Computer Engineering at
Virginia Commonwealth University

By

Xing Li

**Committee in charge**

Prof. Morkoç, Hadis
Prof. Bandyopadhyay, Supriyo
Prof. Baski, Alison
Prof. Özgür, Ümit
Prof. Reshchikov, Mikhail
Dr. Vitaliy Avrutin

July 2012

# Table of contents

# Acknowledgement

This thesis would not have been possible unless the help and support of many people who are gratefully acknowledged here.

I want to express my great gratitude to my dedicated advisor Professor Hadis Morkoç for inspiration and mentoring. He has provided precious and deep ideas, comments and critiques with his profound knowledge in nitride semiconductors and rich research experiences. I am very much thankful to his help during my PhD study.

I would like to thank other committee members: Prof. Supriyo Bandyopadhyay, Prof. Alison Baski, Prof. Ümit Özgür, Prof. Mikhail Reshchikov and Dr. Avrutin Vitaliy. It is a great honor to have them on my committee. Thank you for participating in my PhD journey and your valuable comments and suggestions.

Appreciation is also due to all research collaborators in my lab and other universities. Thanks my lab fellows Xianfeng Ni, Fan Zhang, Serdal Okur, Congyong Zhu, Huiyong Liu for their help on my experiments. Thanks Prof. K. Jarašiūnas for his profound suggestions on explaining physics mechanism of carrier dynamics in the GaN based light emitting diodes (LEDs). To Andy Yankovich from University of Wisconsin, I appreciate his efforts on the scanning transmission electron microscope (STEM) investigations on the LED samples.

Finally, I dedicate my thesis to my parents for their unconditional love and support. Their high expectations have been the real driving forces behind me for so many years. More importantly, I would thank my wife Jiannan Wang, thank you for walking me through my PhD study and beyond and giving me the endless supports in every possible way. I am also very thankful to my parents-in-law for giving me encouragement and all the supports.

# List of Tables

# List of Figures

# Abstract

In the past decade, GaN-based nitrides have had a considerable impact in solid state lighting and high speed high power devices. InGaN-based LEDs have been widely used for all types of displays in TVs, computers, cell phones, etc. More and more high power LEDs have also been introduced in general lighting market. Once widely used, such LEDs could lead to the decrease of worldwide electrical consumption for lighting by more than 50% and reduce total electricity consumption by > 10%.

However, there are still challenges for current state-of-the art InGaN-based LEDs, including 'efficiency droop' issues that cause output power quenching at high current injection levels (> 100 A/cm$^2$). In this dissertation, approaches were investigated to address the major issues related to state-of-the-art nitride LEDs, in particular related to (1) efficiency droop investigations on *m*-plane and *c*-plane LEDs: enhanced matrix elements in *m*-plane LEDs and smaller hole effective mass favors the hole transport across the active region so that *m*-plane LEDs exhibit 30% higher quantum efficiency and negligible efficiency droop at high injection levels compared to *c*-plane counterparts; (2) engineering of InGaN active layers for achieving high quantum efficiency and minimal efficiency droop: lower and thinner InGaN barrier enhance hole transport as well as improves the quantum efficiencies at injection levels; (3) double-heterostructure (DH) active regions: various thicknesses were also investigated in order to understand the electron and hole recombination mechanism. We also present that using multi-thin DH active regions is a superior approach to enhance the quantum efficiency compared with simply increasing the single DH thickness or the number of quantum wells (QWs, 2 nm-thick) in multi-QW (MQW) LED structures due to the better material quality and higher

density of states. Additionally, increased thickness of stair-case electron injectors (SEIs) has been demonstrated to greatly mitigate electron overflow without sacrificing material quality of the active regions. Finally, approaches to enhance light extraction efficiency including using Ga doped ZnO as the *p*-GaN contact layer to improve light extraction as well as current spreading was introduced.

# Chapter 1 Introduction

## 1.1 Motivation

III-nitride is one of the most promising materials for opto-electronics in the blue to the ultra-violet (UV) spectrum as well as applications in high frequency and power electronics. GaN is a wide bandgap material characterized by a parabolic lowest conduction band separated by ~ 1.4 eV from the nearest satellite valley. GaN combined AlN and InN provide variable semiconductors with bandgaps ranging from 0.7 eV (InN) and up to 6.026 eV for AlN. Ternary alloys allow possible realization of whole spectral region covering visible light to deep UV region. The rule of thumb considerations predict that electron velocity saturation in GaN should occur near the onset of strong emission of longitudinal optical (LO) phonons with energy ~ 92 meV, which theoretically accounts for a saturation velocity ~ $3\times10^7$ cm/s. And beneficial to their high electron mobility (typically ~ 1500 $cm^2$/Vs at room temperature for AlGaN/GaN high electron mobility transistors (HEMTs) grown by metaorganic chemical vapor deposition (MOCVD) ), high breakdown field, and high thermal conductivity, GaN based material system has been widely used in high power and frequency electronics. Tremendous improvements have been achieved in GaN based material growth and devices, especially InGaN based LEDs employed in display and general lighting. LEDs differ from traditional light sources in the way they generate light emission. A typical solid state LED is semiconductor diode consisting of a chip of semiconductor material, *i.e.*, InGaN/GaN, treated to create a p-n junction with MQW active region or DHs.  When forward bias was applied, current flows from p-side to the n-side. Electrons and holes flow into the junction, where they either recombine radiatively to emit light or non-radiatively in the form of heating. **Figure 1.1** shows the schematic of electron and hole recombination in the MQW active region.

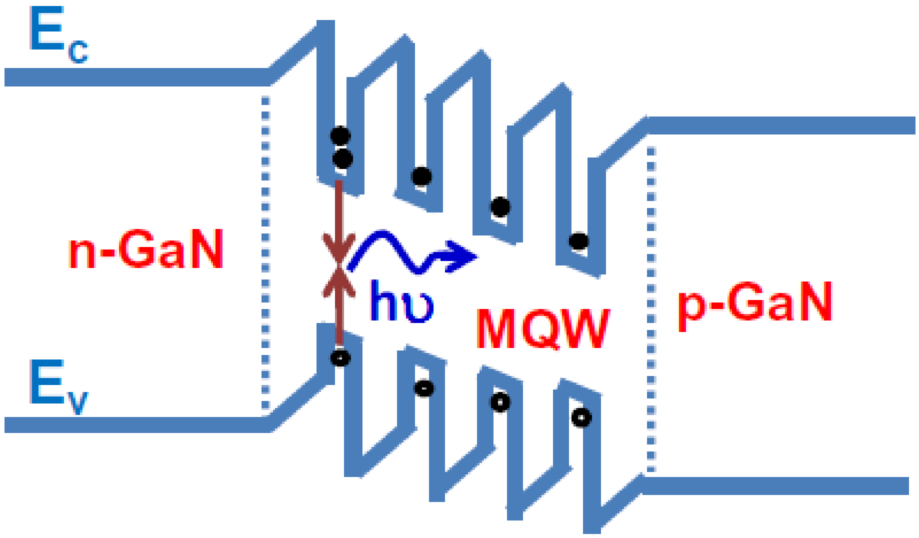

**Figure 1.1** Schematic of the energy band structures for a typical MQW LEDs.

Compared to the traditional incandescent and compact fluorescent lamps, sold state LEDs are more efficient (luminous efficacy above ~100 lm/W), reliable (lifetime > 100,000 hours), and environmentally-friendly. In **Furthermore,** in the realm of energy crisis even little percentage of energy savings could play a crucial role.

**Table 1-1**, cost comparison was made to compare different light technologies. We can see that LED light source can only save 15% of total cost compared to fluorescent lights however it can save more than 30% of energy, which would increase further as the efficacy continues improving. This is obviously very promising under the context of energy saving worldwide. Furthermore, in the realm of energy crisis even little percentage of energy savings could play a crucial role.

**Table 1-1** LED cost comparisons with incandescent and fluorescent light source

| | Incandescent | Fluorescent | LEDs |
|---|---|---|---|
| Purchase price ($) | 2 | 4 | 20 |
| Power usage (W) | 60 | 13 | 9 |
| Lumens | 660 | 660 | 900 |
| Lumens/Watt | 11 | 50.8 | 100 |
| Lifespan (hours) | 2,000 | 8,000 | 25,000 |
| Bulb cost over 10 years - @ 6hours/day ($) | 21.9 | 10.94 | 17.52 |
| Energy consumed over 10 years-@15cents/kWhr ($) | 197.10 | 42.71 | 29.57 |
| Total ($) | 219 | 53.66 | 47.09 |

Although the cost this emerging technology is an issue to be addresses, one can virtually certain that the cost of GaN related technologies will drop by orders of magnitude as this technology matures. The U.S. Department of Energy describes SSL as a pivotal emerging technology that promises to fundamentally change the future of lighting.

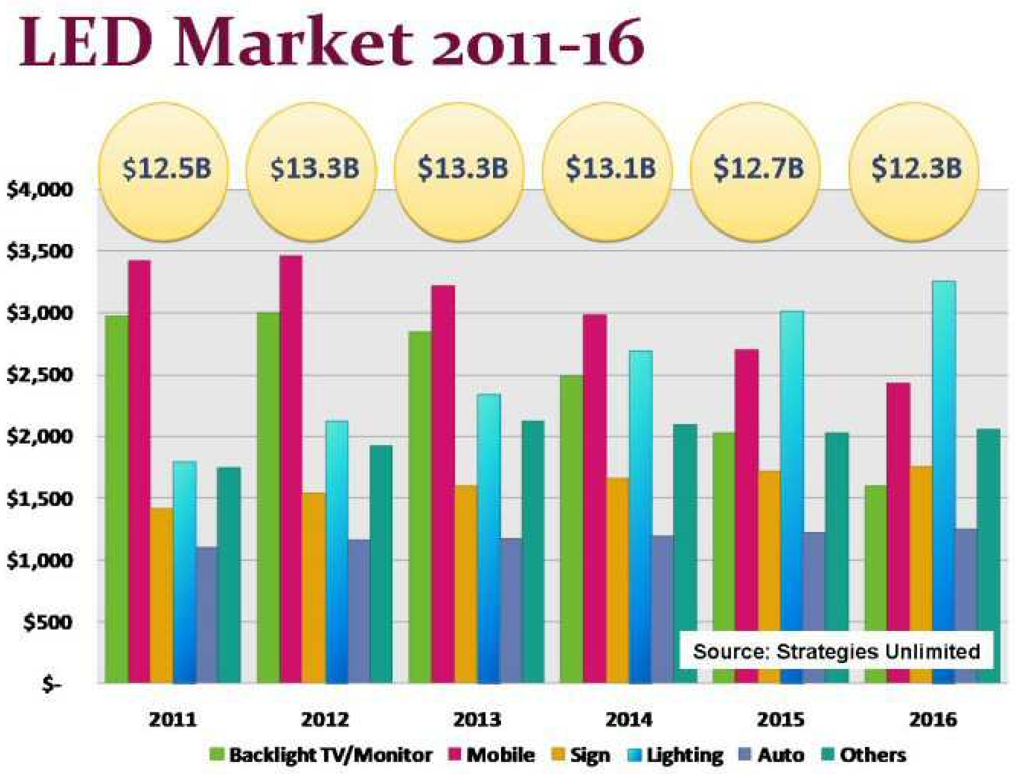

**Figure 1.2** Globe LED market predicated by Strategies Unlimited

As presented in

**Figure 1.2**, the 2011 LED market size is estimated about $12.5 billon. Among the applications, currently about 27.2% of total sale accounted for mobile electronics, 24% for TV/monitors, and 14.4% for general lighting. It is expected that LEDs for general lighting will grow significantly in the next few years. To 2016, the percentage will increase to about 30% for the general light applications. However, challenges are also still prevailing in the process of LED market growth aside of high cost issues including LED performance at high power levels.

### 1.1.1 LED performance metrics

Luminous efficacy (particularly at high injection levels) and color quality are two important technical parameters for the quantification of LEDs.

(1) Luminous efficacy

Energy efficiency of LEDs is measured in lumens per watt (lm/W), which is luminous flux in lumens divided by the applied current and forward voltage. Currently, typical commercial high power LED luminous efficacy is about 140 lm/W at 350 mA forward current.

(2) Color quality

The correlated color temperature (CCT) and color rendering index (CRI) are two basic parameters to qualify the color quality of LEDs. CCT refers to the appearance of a theoretical black body heated to high temperatures. As the black body gets hotter, it turns red, orange, yellow, white, and finally blue. Usually, the optimized white LEDs require CCT of 3000-3500 K.

(3) Color rendering index (CRI)

CRI is a quantitative measure of the ability of light source to reproduce the colors of various objects faithfully in comparison with an ideal light source. The test procedure was established by the International Commission on Illumination (CIE). CRI is calculated by measuring the difference between the lamp in question and a reference lamp in terms of how they render the eight color samples shown in **Figure 1.3**.

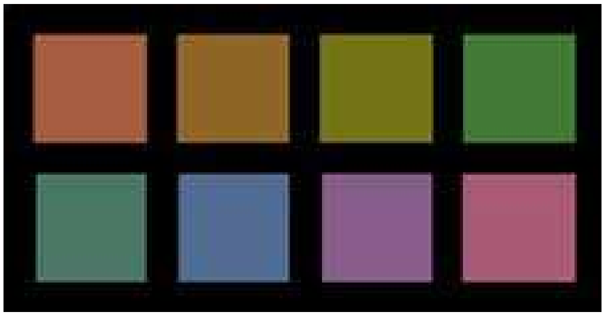

**Figure 1.3** Eight standard color samples used in the test-color method

### 1.1.2 LED performance status

Over the past decades, GaN based LEDs have achieved tremendous improvement in term of luminous efficiency from deep UV region, *i.e.*, 210 nm AlN deep UV diodes, to visible light, *i.e.*, amber and red LEDs. Typical white LEDs used for solid state lighting generally employed high quantum efficiency (Nichia achieved as high as 84% EQE)[1] blue LEDs (460-480 nm with longer wavelength more warm light can be achieved albeit the efficiencies go down) to pump yellow phosphors, which were called phosphor based white LEDs. A common yellow phosphor material is cerium doped yttrium aluminium garnet ($Ce^{3+}$: YAG). In phosphor based white LEDs, a fraction of blue light undergoes the Stokes shift being from shorter wavelengths to longer. Depending on the color of the original LED, phosphors of different colors can be employed. If several phosphor layers of distinct colors are applied, the emitted spectrum is broadened, effectively raising the CRI value of a given LED. Phosphor based white LEDs suffer from efficiency loss due to the heat loss from Stokes shift (usually ~ 10% for YAG) and also other phosphor related degradation issues. Therefore, usually with increasing CRI, the luminous flux as well as efficacy decreased due to the severe loss existing in multi- different color phosphor layers.

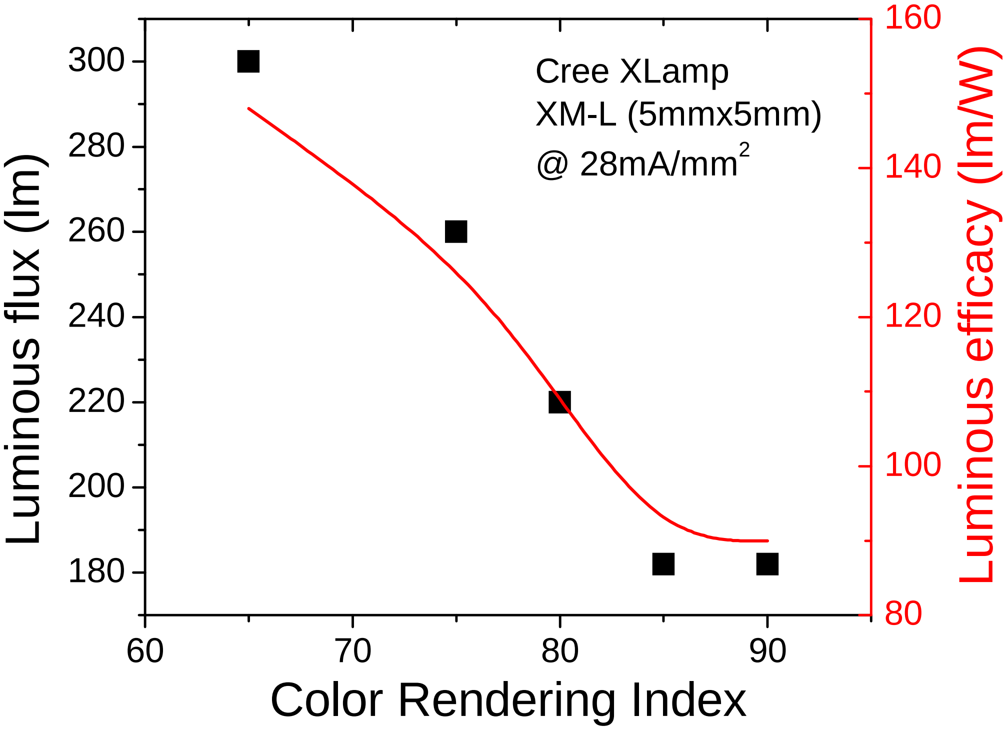

**Figure 1.4** Cree XLamp XM-L LED lamp luminous flux and efficacy changed with the CRI.

As shown in **Figure 1.4**, with increasing CRI from 65 to 90, the Cree XLamp luminous efficacy was reduced from 150 to 90 lm/W. Generally, upon to now, most commercial white LEDs have achieved above 100 lm/W efficacy with CRI ~ 75. Most recently, Osram claims to have set a new laboratory record of ~ 142 lm/W for the efficiency of a warm white LEDs operated under current density of 35 A/cm$^2$ with CRI 81 and CCT 2775 K[2].

### 1.1.3 LED wavelength dependent efficiency

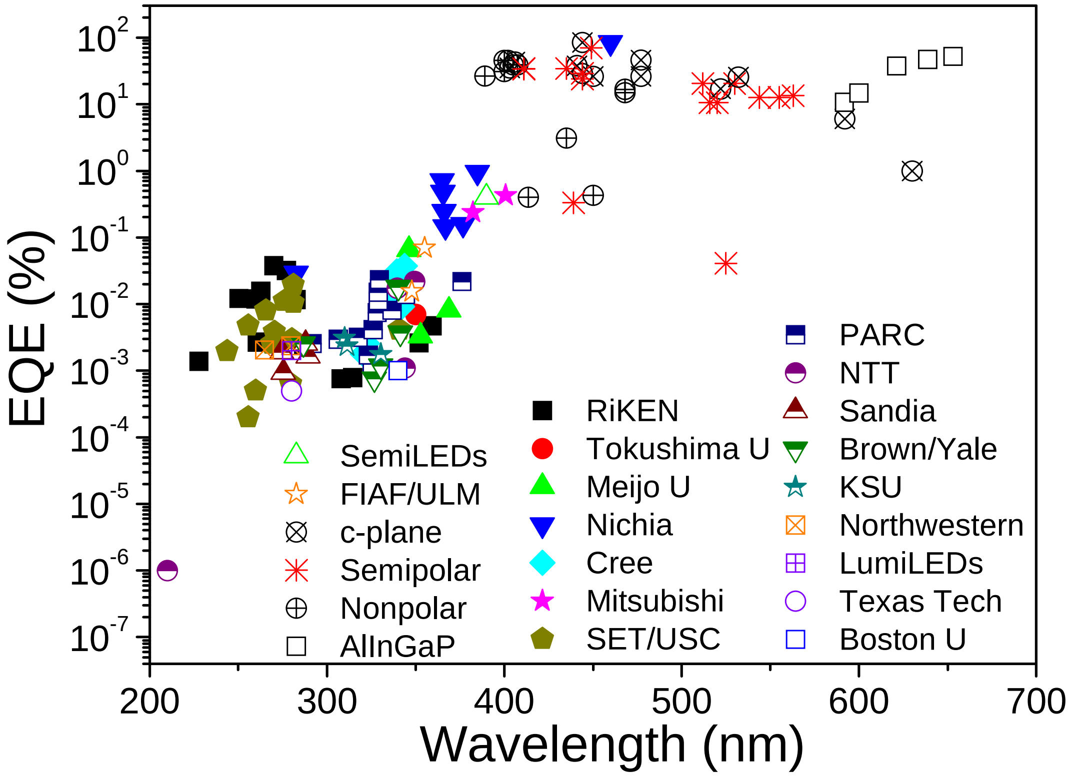

**Figure 1.5** External quantum efficiency (EQE) as a function of LED emission wavelengths (from deep ultraviolet to red) for polar, non-polar and semi-polar GaN based LEDs. AlInGaP based red LEDs are also shown for comparison[3,4,5].

As we all know, wurtzite c-plane GaN exhibit strong non-zero spontaneous polarization due to the deviation of lattice constant ratio c/a from the ideal ratio 1.633. This combines with piezoelectric polarization due to the growth on the lattice-mismatched substrates can substantially cause electron and hole wavefunction separation and thereby reduce radiative recombination rate within the LED active regions. The polarization field effect becomes more pronounced by pushing the emission wavelength to green and red in a way of increasing In composition or active layer thickness. Due to the accumulated strain in the active layer with high In content and temperature sensitive In incorporation rate, growth of thicker high quality In-rich InGaN layer becomes very challenging. Moreover, the increase of active layer thickness as well as In composition will result in the increase of electric field in the active layer. Therefore, extending the emission wavelength from blue to green can substantially degrade device quantum efficiency and its performance. As shown in **Figure 1.5**, the EQE was reduced down to ~ 20% when the wavelength increased to 520 nm in the green region. **Figure 1.5** also indicated that for nitride based LEDs the peak EQE is achieved at wavelength around 460 nm, which has been widely used for phosphor based white LED pumping source. Efforts need to be made to boost the quantum efficiency in the deep UV, UV and red emission regions.

## 1.2 Carrier dynamics in LEDs

The recombination of electrons and holes within the active region could be either radiative or non-radiative. Based on the rate equation, the Shockley-Read-Hall (SRH) non-radiative recombination rate can be expressed as[6]

$$R_{SRH} = \frac{(pn - n_i^2)}{\tau_{nr}(n + p + 2n_i)}$$ **Equation 1-1**

In n-type InGaN active region (assuming background carrier concentration $n_0 = 10^{17}\,cm^{-3}$),

$$R_{SRH} = \frac{(n_0 p_0 + \Delta n(n_0 + p_0) + \Delta n^2 - n_i^{\,2})}{\tau_{nr}(n_0 + p_0 + 2\Delta n + 2n_i)} \approx A\frac{(\Delta n n_0 + \Delta n^2)}{(n_0 + 2\Delta n)}$$ **Equation 1-2**

, where $\Delta n$ is the excess electron concentration, A is the SRH recombination coefficient. At high injection levels, $\Delta n \gg n_0, p_0, n_i$, $R_{SRH} = \frac{1}{2} A\Delta n$ ; At low injection levels, $\Delta n \ll n_0, n_0 \gg p_0$, $R_{SRH} = A\Delta n$ .

The bimolecular radiative recombination rate is described as

$$R = Bnp = B(n_0 + \Delta n)(p_0 + \Delta p) = B\Delta n(n_0 + \Delta n)$$ **Equation 1-3**

, where $B$ is the bimolecular radiative recombination coefficient. At low injection currents, $\Delta n \ll n_0$, $R = B\Delta n^2 \approx Bn^2$ . At high injection, $\Delta n \gg n_0$ , $R = B\Delta n n_0$ . Neglecting other types of carrier loss such as Auger recombination and carrier spillover, which will be covered in Chapter 2 and assuming integrated PL intensity (light output) is proportional to the radiative recombination rate as

$$I_{PL} = \eta_c B(n_0 + \Delta n)\Delta n$$ **Equation 1-4**

,where $\eta_c$ is the extraction efficiency assumed to be unity in the following calculations for simplifying.

The generation rate G by optical laser excitation can be expressed as

$$G = P_{laser}(1 - R)\alpha / (A_{spot} h\nu)$$ **Equation 1-5**

, where $P_{laser}$ is the excitation laser power incident on the sample surface, R is the Fresnel reflection on the sample surface which can be measured, $\alpha$ is the absorption coefficient, $A_{spot}$ laser spot size on the sample surface (100 µm in diameter), $h\nu$ is the laser excitation energy (3.22 eV). Combing **Equations 1-4** and **1-5**, we can calculate integrated PL intensity as a function of laser excitation power. **Figure 1.6** shows the calculated PL intensity versus excitation laser power density with changing background carrier concentration $n_0$. We can see that with increasing $n_0$ from $10^{16}$ cm$^{-3}$ to $10^{18}$ cm$^{-3}$ the PL intensity is increased at low injection levels and further increasing to $10^{19}$ cm$^{-3}$ saturate the PL intensity at low injection levels. This can be explained by the carrier diffusion phenomena. With higher carrier concentrations, the carrier diffusion into the active region becomes more pronounced ascribed to the carrier density gradient and thus the possibility of radiative recombination is increased offering more light output. However, at higher injection levels, the excess electron concentration $\Delta n$ exceeds the background carrier concentration and thus the PL intensity saturates to a same level. Moreover, we should note that at low $n_0$ = $10^{16}$ cm$^{-3}$, the slope of light output vs. laser power density is about 2 while it becomes 1 at high injection levels, which indicates the recombination dynamics transition from non-radiative to radiative recombination (dominant at high injection levels)[7]. With increasing $n_0$, the slope changed to 1 all the way through the whole laser excitation regions.

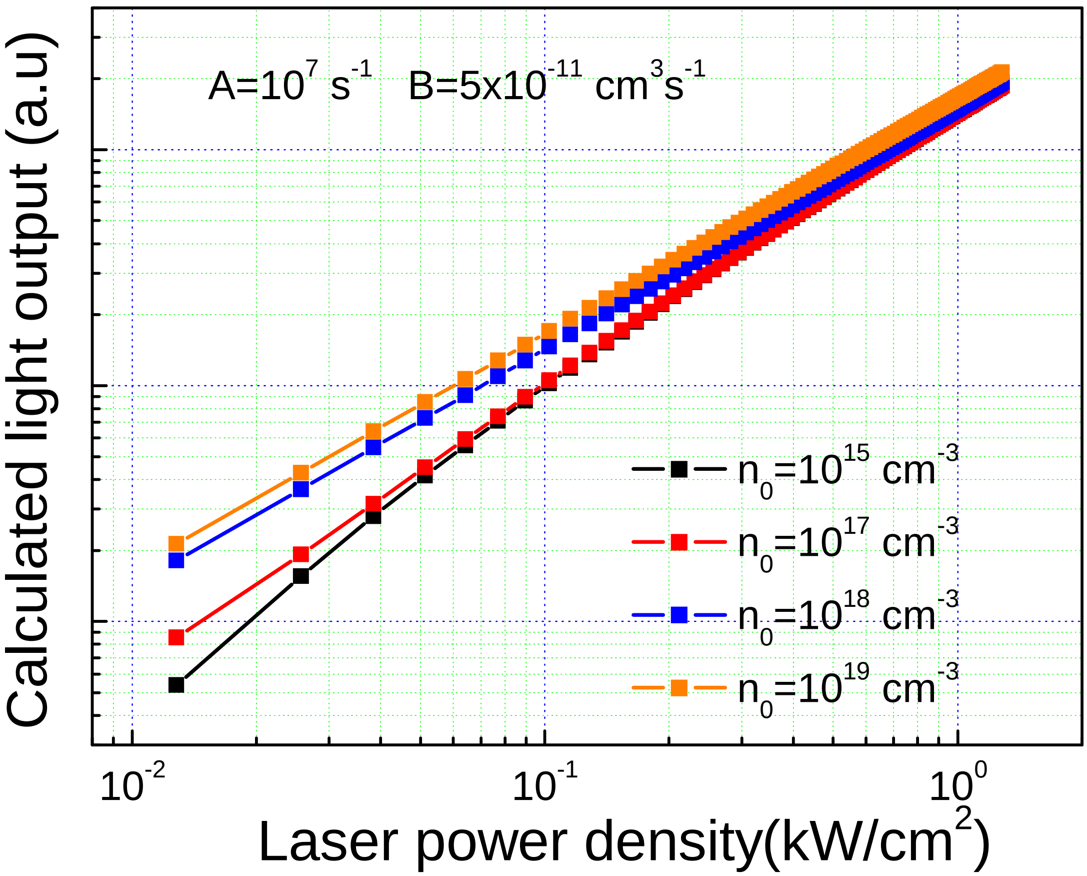
A=10^7 s^-1 B=5x10^-11 cm^3s^-1
Calculated light output (a.u)
Laser power density(kW/cm^2)
10^-2
10^-1
10^0
n_0=10^15 cm^-3
n_0=10^17 cm^-3
n_0=10^18 cm^-3
n_0=10^19 cm^-3

**Figure 1.6** the calculated light output (integrated PL intensity) as a function of laser power density with varying background carrier concentration.

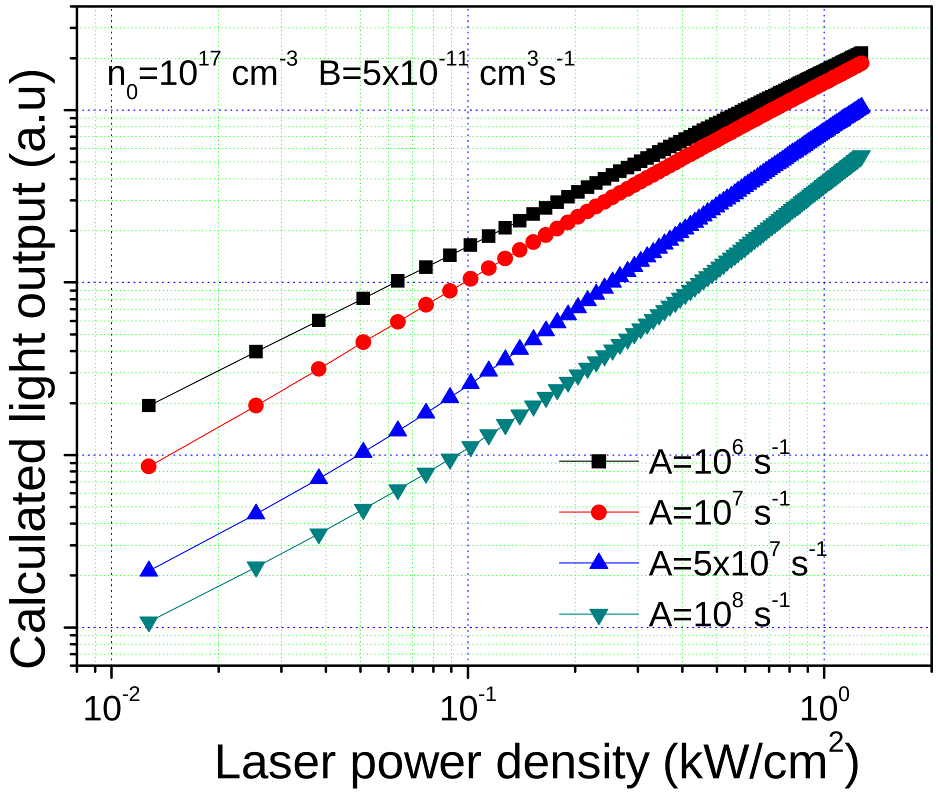

**Figure 1.7** the calculated light output (integrated PL intensity) as a function of laser power density with A coefficients.

**Figure 1.7** presents the calculated light output vs. laser power density with varying A coefficients. As expected, with smaller A coefficients, the light output is increased at low injection levels due to the reduced non-radiative recombination rate. In order to better understand the carrier recombination mechanics based on the rate equation, we extracted the light output loss part (negative parts in the **Equation 1-4**) and gain part (positive parts in the **Equation 1-4**). For simplifying, we assumed

$$A\frac{(\Delta n n_0+\Delta n^2)}{(n_0+2\Delta n)}\approx A\Delta n \qquad \textbf{Equation 1-6}$$

Then from $G = A\Delta n + B\Delta n(n_0 + \Delta n)$, we can obtain

$$\Delta n = \frac{-A - Bn_0 + \sqrt{A^2 + 2ABn_0 + B^2 n_0^2 + 4GB}}{2B}$$ **Equation 1-7**

Substituting **Equation 1-7** in to the integrated PL intensity (light output) expression $I_{PL} = \eta_c B(n_0 + \Delta n)\Delta n$, the loss part of the PL intensity is expressed as

$$I_{PL}(loss) = -\frac{1}{2}\left[ n_0(A + Bn_0) + \frac{A + Bn_0}{B}\sqrt{A^2 + 2ABn_0 + B^2 n_0^2 + 4GB} \right]$$ **Equation 1-8**

Hence we obtained $I_{PL}(gain) = I_{PL} - I_{PL}(loss)$.

The calculated results are shown in **Figure 1.8**. As we can see, with increasing the injection, the loss of the light output increased accordingly due to the non-radiative loss.

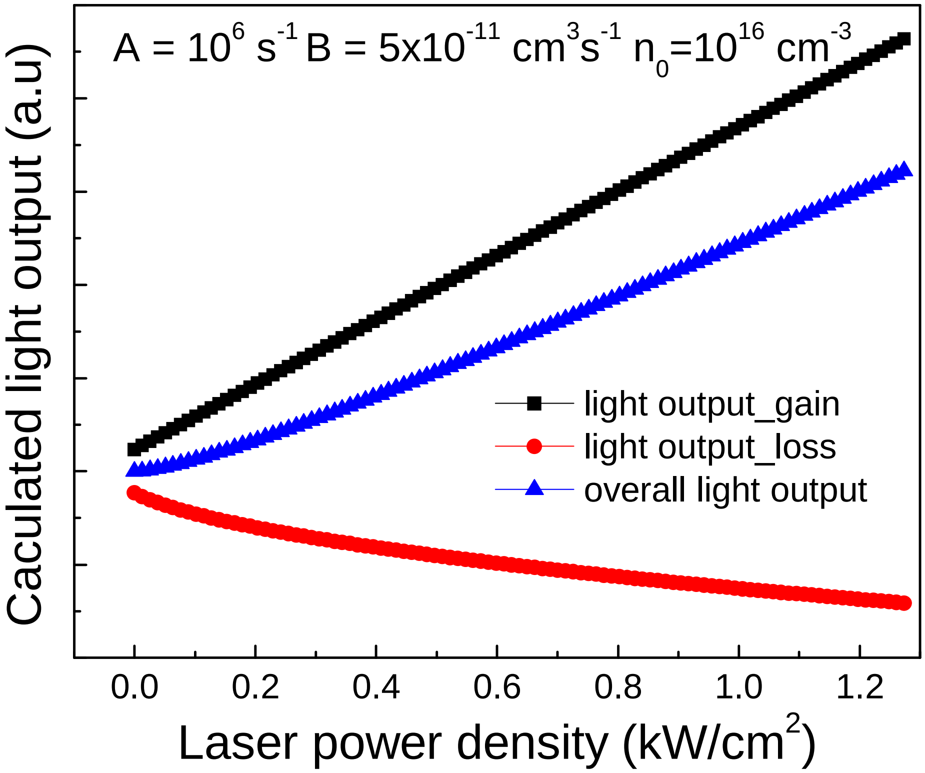

**Figure 1.8** Calculated light output loss and gain parts versus laser power density

Similarly, for the electrical injection case, the rate equation can be expressed as

$$\frac{dn}{dt} = A\frac{(\Delta n n_0 + \Delta n^2)}{(n_0 + 2\Delta n)} + B\Delta n(n_0 + \Delta n) - \frac{J}{qd} = 0$$ **Equation 1-9**

, where $q$ is the electron charge, $d$ is the thickness of the active layer, and $J$ is the injected current density. At equilibrium,

$$\frac{J}{qd} = A\frac{(\Delta n n_0 + \Delta n^2)}{(n_0 + 2\Delta n)} + B(\Delta n + n_0)\Delta n$$ **Equation 1-10**

The EL intensity can be written as

$$I_{EL} = \eta_c B\Delta n(n_0 + \Delta n)$$ **Equation 1-11**

Again, assume $\eta_c = 1$ for the following calculations for simplifying.

**Figure 1.9** shows the calculated EL intensity versus injected current density with varying background carrier concentration $n_0$. Similar conclusions as that shown in **Figure 1.6** can be drawn.

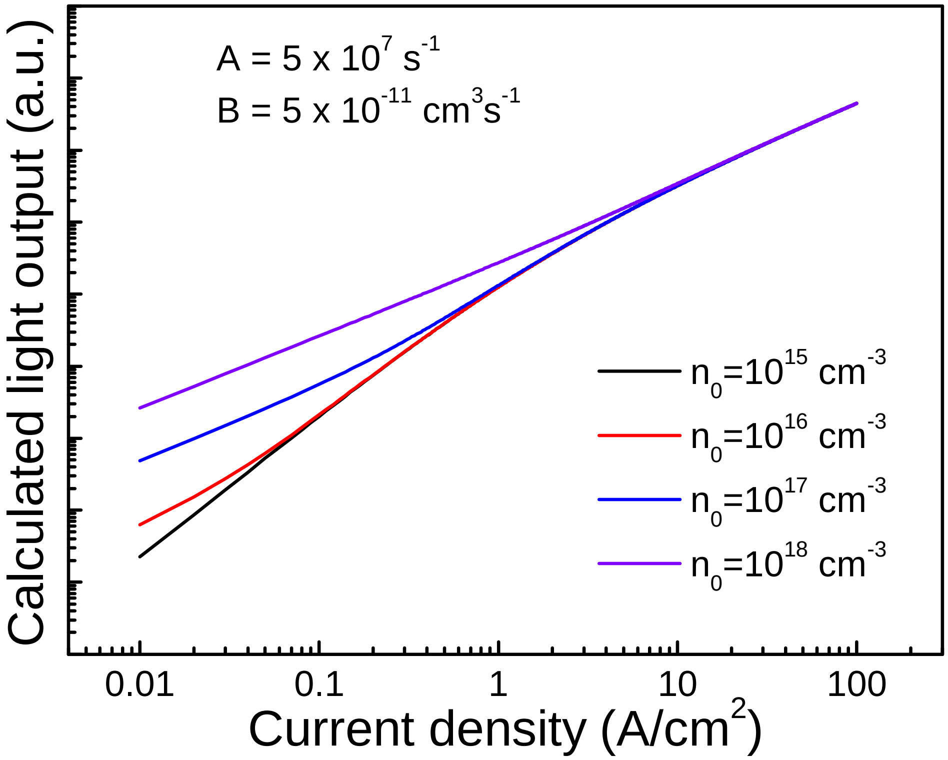

**Figure 1.9** The calculated light output (EL intensity) as a function of injected current density with varying background carrier concentration $n_0$.

Another type of nonradiative recombination is Auger recombination, in which the energy given off by the recombination of electron and hole is used to excite another carrier to a higher energy which in turn thermalizes down to lower energy state by phonon emission. The Auger recombination rate is given by $C\Delta n^3$, which deems as negligible in wide bandgap GaN and thus was neglected here for calculation.

An additional form of carrier loss mechanism, which is also deemed as most important one, is carrier overflow or spillover, especially for electrons as they are lighter in terms of effective mass (0.2 $m_0$ in GaN). The electrons that gained extra kinetic energy through band discontinuity can escape the active region, ending up with recombining at the p-region or the contact and not contributing to the desired emission in the active region. Combining with calculated results, we can conclude that in order to achieve high quantum efficiency for high power LEDs requiring large current injection, both nonradiative recombination and carrier overflow or spillover should be minimized.

## 1.3 Scope of research

The research presented here concentrated primarily on LED structure designs to enhance the quantum efficiency as well as mitigating the efficiency droop at high injection levels.

The dissertation is organized as follows: Chapter 2 is a discussion of efficiency droop issues persisted in the InGaN based LEDs. A review of the major causes will be included. Our proposed mechanism will also be introduced and discussed.

Chapter 3 focuses on how to mitigate efficiency droop. Various active region structure designs will be presented and their effects on efficiency droop will be discussed. The comparison of LED performance grown on c-plane and m-plane substrates provided additional insight on efficiency droop caused by poor hole transport. We proposed that m-plane LED offers higher quantum efficiency and reduced efficiency droop. In Chapter 4, we will demonstrate higher quantum efficiency can be achieved by using multi-DH structures compared with single DH and multi quantum wells (MQWs). Under this realm, we will also present with optimized SEI thickness the EQE can be further improved for thin active regions such as single 3 nm DH due to the much reduced electron overflow with increasing SEI thickness. Finally conclusions and suggestions for future work will be presented in Chapter 5.

# Chapter 2 Efficiency droop investigations

## 2.1 Introduction to the efficiency droop

InGaN based light emitting diodes (LEDs) are becoming widely used for indoor and outdoor lighting, and displays with internal quantum efficiency (IQE) and optical extraction efficiency in high performance devices being in the range of 80%[8]. Blue InGaN based LEDs operating at low injection levels with optimized packaging are capable of luminous efficiencies over 200 lm/W at research/development level. However, LEDs suffer from the reduction of efficiency at high injection current levels. As shown in **Figure 2.1**, a commercial LED die produced by Cree, Inc shows as high as 135 lm/W at 350 mA operation current while it reduced down to 85 lm/W when the operation current exceeding 1.5 A. To account for the efficiency droop, various models have been proposed, including current roll-over[9], carrier injection inefficiency due in most part to relatively low hole concentration in the *p*-layer[10,11,12], polarization field[13,14], Auger recombination[15], and junction heating[16]. Normally, Auger recombination is expected to be relatively small in wide band gap semiconductors[17], as verified by fully microscopic many body models[18]. Meanwhile our optical excitation experiments in which carriers are only excited and thus recombine in MQWs showed no efficiency droop even at the maximum excitation density employed (carrier generation rate $3.7\times10^{31}$ $\text{cm}^{-3}\text{s}^{-1}$ approximately)[19]. One would normally assume that this observation would be sufficient to conclude that the efficiency droop is related to the skewed carrier injection due to the disparity of hole and electron concentrations, large hole effective mass, and carrier spillover instead of the Auger recombination. As reported, Xie *et al.* [19] employed either *p*-type doped InGaN barriers or lightly *n*-type doped GaN electron injection layer just below the MQWs to achieve comparable levels of electron and hole injection and observed mitigation of the droop, which suggest poor hole transport and injection through the barrier being the responsible mechanism, thereby leading to serious electron leakage. Ni *et al*. offered further supporting data for the hole impediment model proposed in Ref.19 by investigating the efficiency droop in double heterostructure (DH) LEDs with different active layer thicknesses both theoretically and experimentally[20]. Furthermore, carrier leakage in rate equation models has already been shown to better explain carrier recombination and loss in InGaAsP lasers having low acceptor concentrations in the p-InP layer and InGaN green LEDs[21,22].

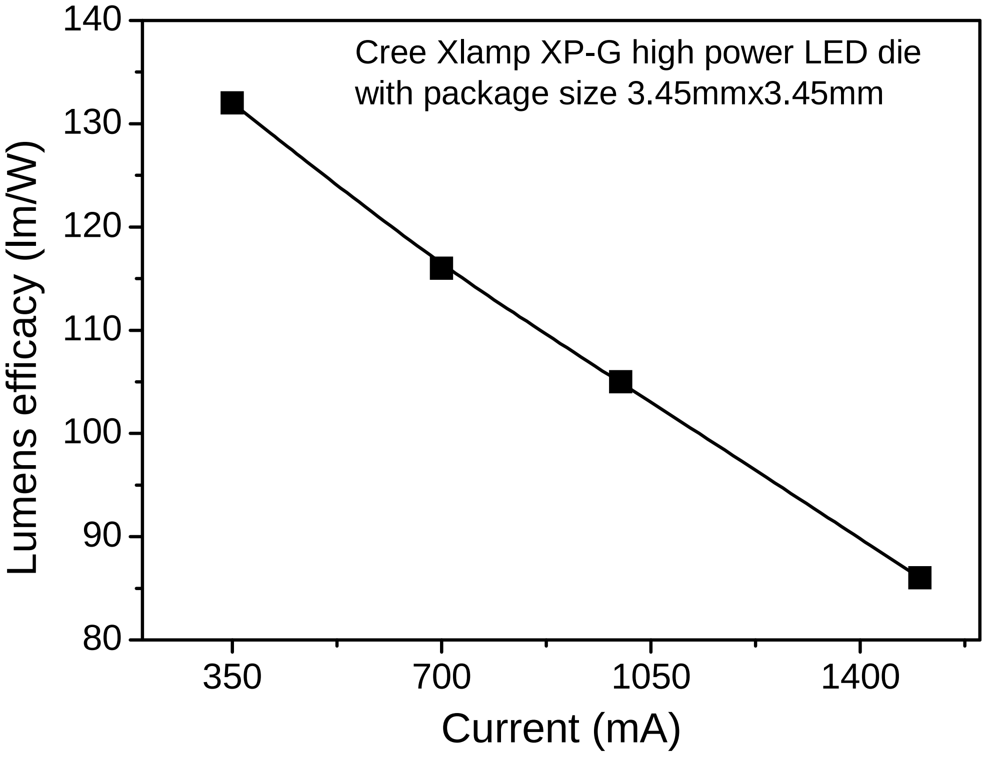

**Figure 2.1** Cree Xlamp XP-G high power LED die lumens efficacy as a function of operation current

We also propose the electron overflow or spillover to be the dominant mechanism responsible for the efficiency loss issue. The term "spillover electrons" refers to the electrons which escape the active region without participating in any recombination process, radiative and non-radiative alike, and end up recombining in the p-GaN region or make it to the p-contact if the minority carrier lifetime in that region permits it. We will propose a possible solution (using staircase electron injector) to eliminate the electron overflow differing conventional approaches.

## 2.2 Carrier spillover versus Auger loss

Using the assumption that the recombination region is much thinner than the natural diffusion length of minority carriers for DH or MQW LEDs, the recombination rate equation under steady state is typically described as $An + Bn^2 + Cn^3 = J / qd$ . The term $C$ represents Auger nonradiative coefficients. Therefore, in the absence of carrier spillover the IQE can be written as $\eta_{\text{int}} = \tau_{eff} / \tau_r = Bn^2 / (An + Bn^2 + Cn^3)$ . If it were possible to measure IQE *vs.* the injected current density $J$, one could obtain $A$, $B$, and $C$ coefficients through a third order polynomial fitting, albeit without a unique solution. The collected radiative power can also be measured vs. the optical excitation power from which A and C coefficients can be deduced for a given B coefficient assuming that the extraction and collection efficiency remains the same for all excitation levels[23]. Let us now turn our attention to calculating $A$ and $B$ coefficients first. Assuming a trap density of $N_t \approx 10^{16}$ cm$^{-3}$, a capture cross section of $\sigma = 10^{-15}$ cm$^2$ for this particular trap, and a thermal velocity of $v_{th}$ = $5\times10^{6}$ cm/s, which are reasonable, $A$ coefficient is found to be $A = 1/\tau_{nr} = \sigma v_{th} N_t$ = $5\times10^{7}$s$^{-1}$, which is consistent with other report[24] where this coefficient is extracted from a fitting of the light output dependence on the injection current density. For a detailed calculation of the $B$ coefficient, one can refer to Ref. 19, but in a simple sense, $B = G/n_i^2 \approx 4.1\times10^{-9}$ cm$^{3}$s$^{-1}$ for GaN, where $G$ is the generation rate per unit volume and $n_i$ is the intrinsic carrier concentration. Doing so leads to a $B$ coefficient value for $In_{0.2}Ga_{0.8}N$ of approximately $1.2\times10^{-10}$ cm$^{3}$s$^{-1}$. These calculated $A$ and $B$ values will serve as reference ranges for those extracted from fits to the curves of the light output *vs.* injection current density in order to reduce the error in values obtained from the polynomial fitting.

According to Ref. 25 and as shown in **Figure 2.2**, the calculated $C$ values for both LEDs are already out of the expected range of $1.4\times10^{-30}$ cm$^{6}$s$^{-1}$ to $2\times10^{-30}$ cm$^{6}$s$^{-1}$ predicted in Ref. 15.

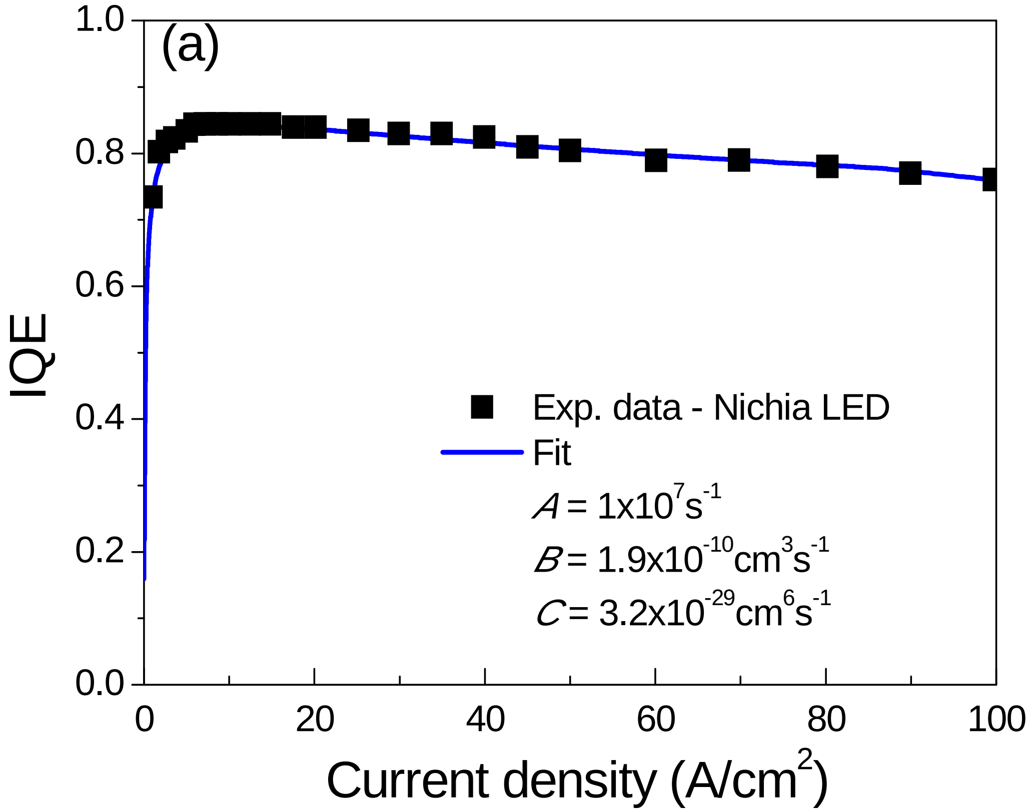
(a)
IQE
1.0
0.8
0.6
0.4
0.2
0.0
0
20
40
60
80
100
Current density (A/cm$^2$)
Exp. data - Nichia LED
Fit
$A = 1\text{x}10^{7}\text{s}^{-1}$
$B = 1.9\text{x}10^{-10}\text{cm}^{3}\text{s}^{-1}$
$C = 3.2\text{x}10^{-29}\text{cm}^{6}\text{s}^{-1}$

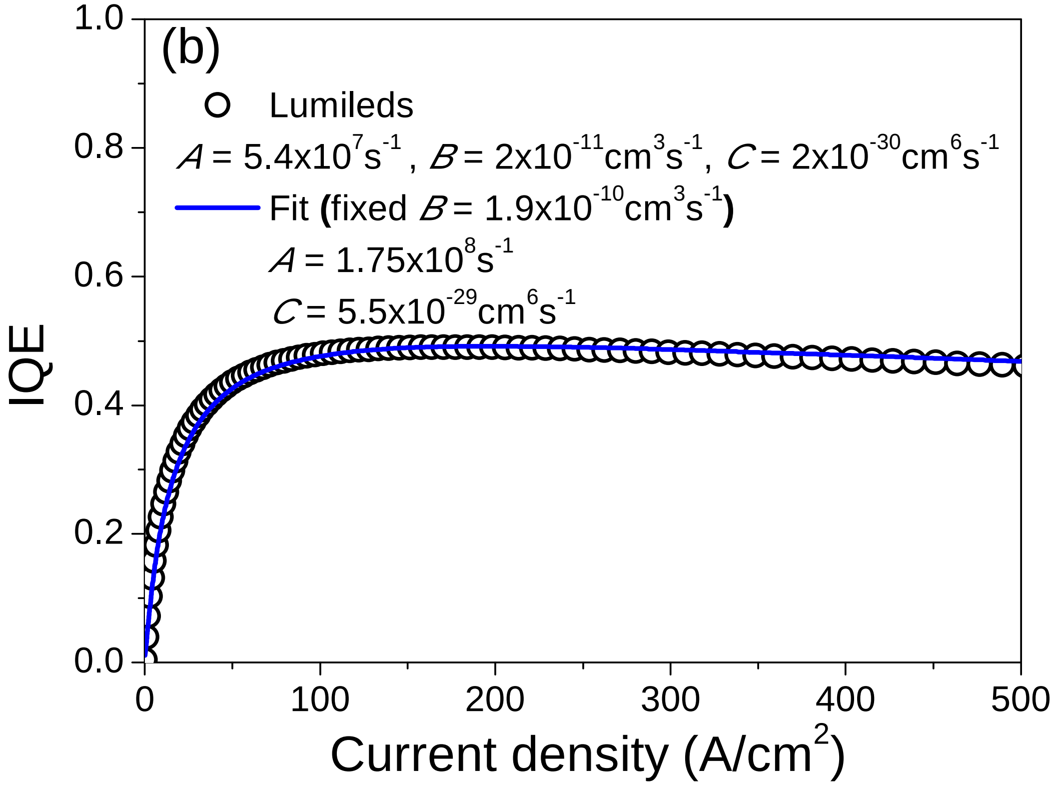
(b)
IQE
1.0
0.8
0.6
0.4
0.2
0.0
0
100
200
300
400
500
Current density (A/cm$^2$)
Lumileds
$A = 5.4\text{x}10^{7}\text{s}^{-1}$, $B = 2\text{x}10^{-11}\text{cm}^{3}\text{s}^{-1}$, $C = 2\text{x}10^{-30}\text{cm}^{6}\text{s}^{-1}$
Fit (fixed $B = 1.9\text{x}10^{-10}\text{cm}^{3}\text{s}^{-1}$)
$A = 1.75\text{x}10^{8}\text{s}^{-1}$
$C = 5.5\text{x}10^{-29}\text{cm}^{6}\text{s}^{-1}$

**Figure 2.2** Calculated IQE vs. current density for the case Auger term is figured in. The two sets of A, B and C values agree well with the LEDs from (a) Manufacturer I and (b) Manufacturer II.

The fits to the experimental data indicate that when the *B* coefficient is modified, *A* and *C* coefficients can be adjusted accordingly to represent the IQE data from all LEDs investigated here. Furthermore, the question that arises is whether the efficiency degradation is really caused by Auger recombination or can be explained by other processes such as carrier spillover or a combination of the two.

To investigate whether the carrier spillover might be responsible for the efficiency droop as opposed to the Auger recombination, the recombination rate equation under steady state was modified as $(J - J_{spillover})/qd = An + Bn^2 + Cn^3 + J_{spillover}/qt$ . When an empirical dependence of the spillover current on the injection current is chosen as $J_{spillover}=kJ^b$ (power series/Taylor series) with $k$ and $b$ being fitting parameters, and $t = d$[26] ($n^3$ like dependence if the radiative current dependence on electron density is used), reasonable fits to the experimental data from different LEDs can be obtained without the Auger term ($C = 0$) but with spillover term, as shown in **Figure 2.3**. These results indicate that efficiency droop in blue LEDs can be empirically described by carrier spillover without the need for Auger recombination.

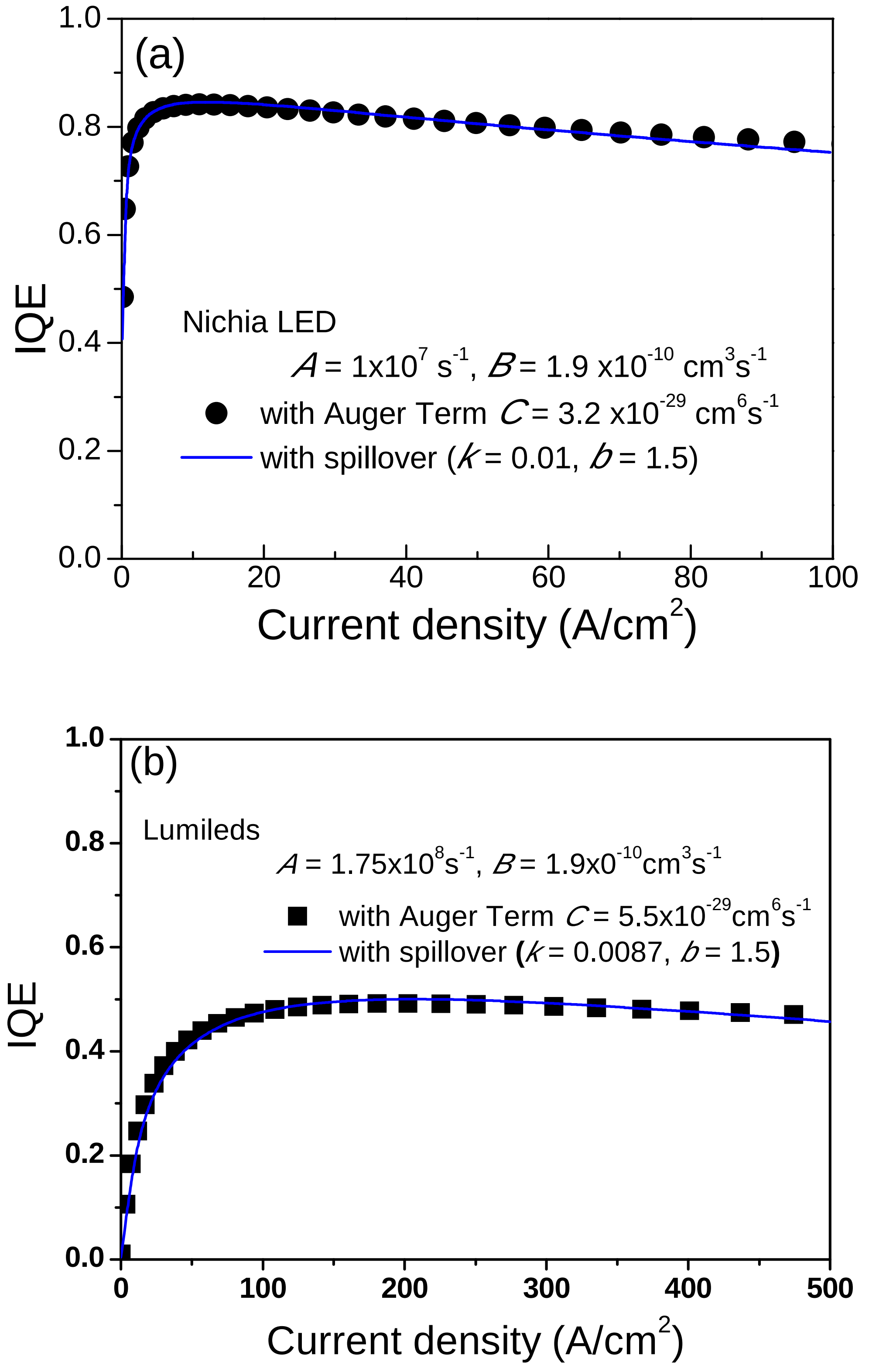

**Figure 2.3** Calculated IQE vs. injection for the case carrier spillover term is figured in.

The spillover terms agree well with the LEDs from (a) Manufacturer I and (b) Manufacturer II.

In order to really delineate the effect of carrier spillover at high injection levels, our earlier experiments pointing to the efficiency droop in either multiple quantum well (MQW) or DH LEDs suggest that poor hole transport might mainly be responsible for the observed efficiency droop. In terms of MQW LEDs, efficiency droop in samples with different barrier thickness was investigated. As shown in **Figure 2.4**, the LED sample with 6 periods of 12 nm-thick $In_{0.01}Ga_{0.99}N$ barriers and 2nm-thick $In_{0.14}Ga_{0.86}N$ wells shows an obvious efficiency droop for pulsed current densities beyond 300 $Acm^{-2}$. In contrast, samples having the same type of wells (2 nm-thick $In_{0.14}Ga_{0.86}N$) but barriers with reduced thickness (3nm) show almost no droop with increasing injection current once the maximum efficiency is nearly attained. These results suggest that reducing the barrier thickness can favor efficient hole transport through the active region, which consequently reduces the efficiency droop. More detailed and optimized experimental results will be provided in the following chapters.

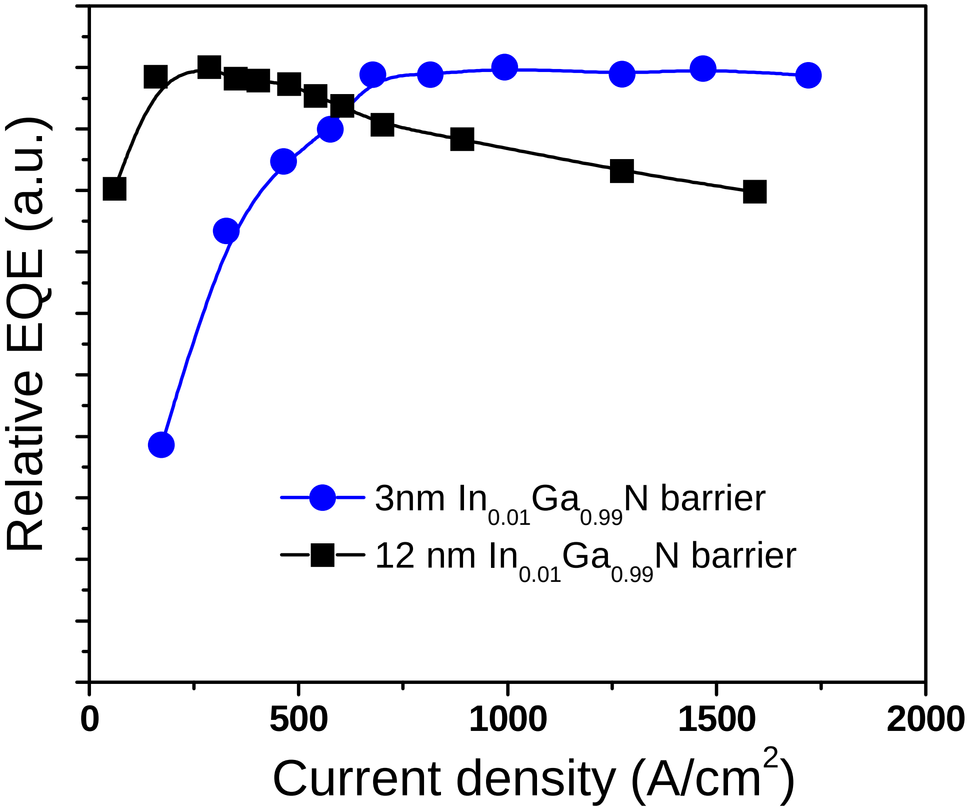

**Figure 2.4** Relative EQE for 6 period MQW-LEDs with 2 nm-thick $In_{0.14}Ga_{0.86}N$ wells with different barrier thickness: 12 nm- and 3nm -thick $In_{0.01}Ga_{0.99}N$.

## 2.3 Experimental proof: electron blocking layer effect

### 2.3.1 Motivations

The AlGaN EBL was usually introduced into the GaN based LEDs in order to eliminate the electron spillover to the p-GaN side due to the kinectic energy gained by band gap discontinuity and applied electrical field. The AlGaN EBL layer set here can provide barrier to reduce electron spillover. However, as we will discuss later, the polarization charges existing in the interface between AlGaN and GaN can lower down the barrier height and also AlGaN can reduce the hole injection efficiency further than it already has. However, the original idea of this section was to investigate the EBL effects on the quantum efficiency of LEDs grown on both c- and m-orientations aiming for the principle understanding of electron spillover process. Therefore, the LEDs with MQW active regions with and without p-type EBL were designed and grown on c-plane GaN templates and HVPE grown m-plane freestanding wafers. The relative EQE was measured and compared.

### 2.3.2 Experimental procedures

All LED structures were grown on freestanding m-plane and c-plane bulk GaN substrates in a vertical low-pressure metalorganic chemical vapor deposition (MOCVD) system. They are composed of 6 period 2 nm $In_{0.14}Ga_{0.86}N$ quantum wells with 12 nm $In_{0.01}Ga_{0.99}N$ barriers, and a 60 nm Si-doped ($2\times10^{18}$ $cm^{-3}$) $In_{0.01}Ga_{0.99}N$ underlayer just beneath the active region for improved quality. A ~10 nm $p$-$Al_{0.15}Ga_{0.85}N$ electron blocking layer was deposited on top of the active quantum well region. The Mg-doped *p*-GaN layer that followed is about 100 nm thick having $7\times10^{17}$ $cm^{-3}$ hole concentration for the c-plane variety, as determined by Hall measurements on a calibration sample, which is expected to be higher for the m-plane orientation due to lighter hole effective mass for the same Mg chemical content. Due to the fact that the m-plane LED sample is extremely small, we did not perform Hall measurements. Further details and the schematic of the LED structures can be found in Ref.19. After mesa (250 μm diameter) etching, Ti/Al/Ni/Au (30/100/40/50 nm) metallization annealed at 800 ºC for 60 seconds was used for *n*-type ohmic contacts and 5 nm/5 nm Ni/Au contacts were used for the semi-transparent *p*-contacts. Finally, 40/50 nm Ni/Au contact pads were deposited on the top of part of the mesa. The 500 μm-thick *m*-plane freestanding GaN templates, produced at

Kyma Technologies, Inc., have a threading dislocation density of <5x$10^6$ cm$^{-2}$ and are off-cut by 0.2° towards the GaN *a*-axis and 0.3° towards the GaN *c*-axis. The *c*-plane freestanding GaN is around 250 $\mu$m thick.

### 2.3.3 Results and discussions

The IQE values were extracted from the excitation-dependent PL studies with resonant excitation at room temperature using a frequency-doubled 80 MHz repetition rate femtosecond Ti:Sapphire laser. The excitation laser wavelength was 370 nm whose energy is below the bandgap of the quantum barriers and top GaN, but higher than that of the active regions. In this scenario, the photo-excited electron-hole pairs are generated only within the quantum wells where they are forced to recombine either radiatively or nonradiatively. In terms of efficiency determination, we have used a procedure similar to that described in Ref. 23. Later on, we will introduce temperature dependent PL measurement methods to determine IQE which was proved to be more reliable and straightforward.

**Figure 2.5** shows IQE values of all LED samples vs. the induced carrier concentration calculated from the resonant PL measurements using excitation power-dependence. The IQE values of c-plane LEDs are very similar (~ 45 %) in whole range of carrier concentration over $1 \times 10^{18}$ cm$^{-3}$ regardless of having EBL or not, which indicated that the optical quality of the as grown layers with and withour EBL are comparable. Compared to the IQE of c-plane LEDs, m-plane LED shows much higher IQE at the same carrier concentration attributed to advantages of non-polar orientation such as absence of polarization fields, higher hole concentration induced by small hole effective mass, and larger optical matrix elements relative to its c-plane counterpart, resulting in improved performance of MQWs.[27] We should note that the m-plane LED without EBL shows even higher IQE values than the one with EBL, which might be attributed to the quality variations between two m-plane bulk substrates.

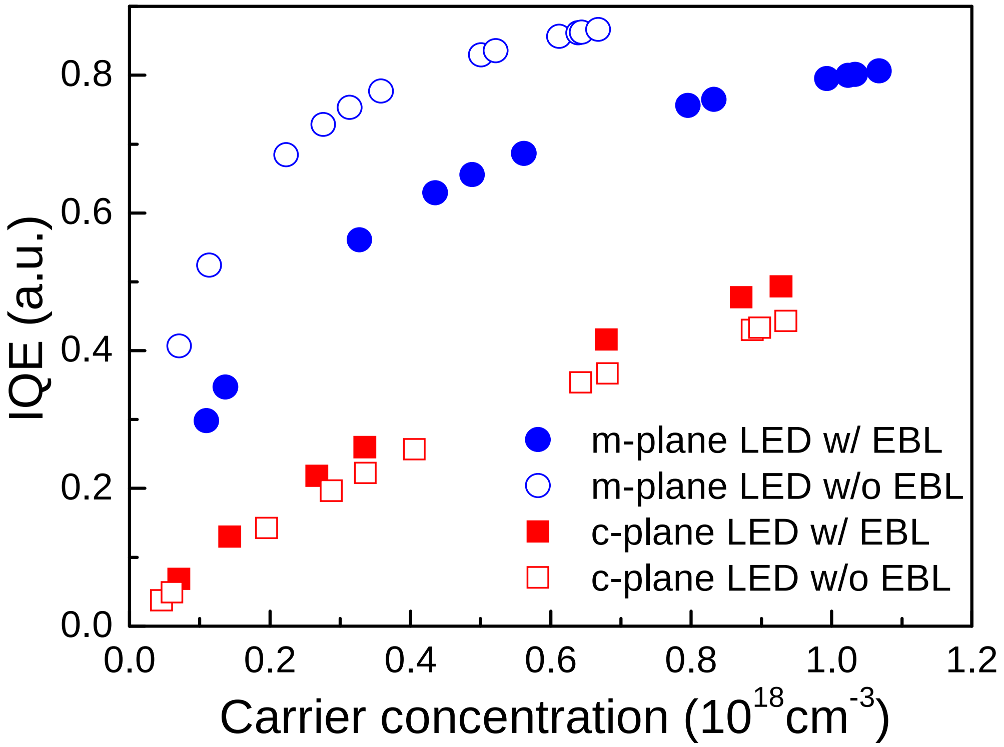

**Figure 2.5** IQE values of c- and m-plane LEDs with and without EBL vs. the induced carrier concentration calculated from the resonant PL measurements using excitation power-dependence. For the calculation of carrier concentrations, the B value was assumed to be $1\times10^{-11}$ cm$^3$s$^{-1}$.

However, regarding to the EQE performance for these two sets of LEDs, different pictures can be found. **Figure 2.6** shows relative EQE values of all LED samples vs. current density applied by the pulsed current source (0.1% duty cycle). The m-plane LED with EBL shows EQE peaks at higher current level (300 A/cm$^2$) than the c-plane LED with EBL (150 A/cm$^2$). And in terms of efficiency droop ratio the former also has much lower EQE decreasing slope with current increasing than the latter, resulting in 2 times higher EQE in m-plane LED than c-plane LED at very high current density (over 2000 A/cm$^2$). Among many mechanisms causing this different device performance, electron spillover to p-GaN is believed to be a main reason. It should be noted that regardless of crystal orientation, the LEDs with EBL shows much higher relative EQE than those without EBL. The fact that m-plane LED, which is free from polarization effect, after removing EBL suffers severe EQE drop indicates that electron leakage over the electron blocking layer is a main origin of the efficiency droop.

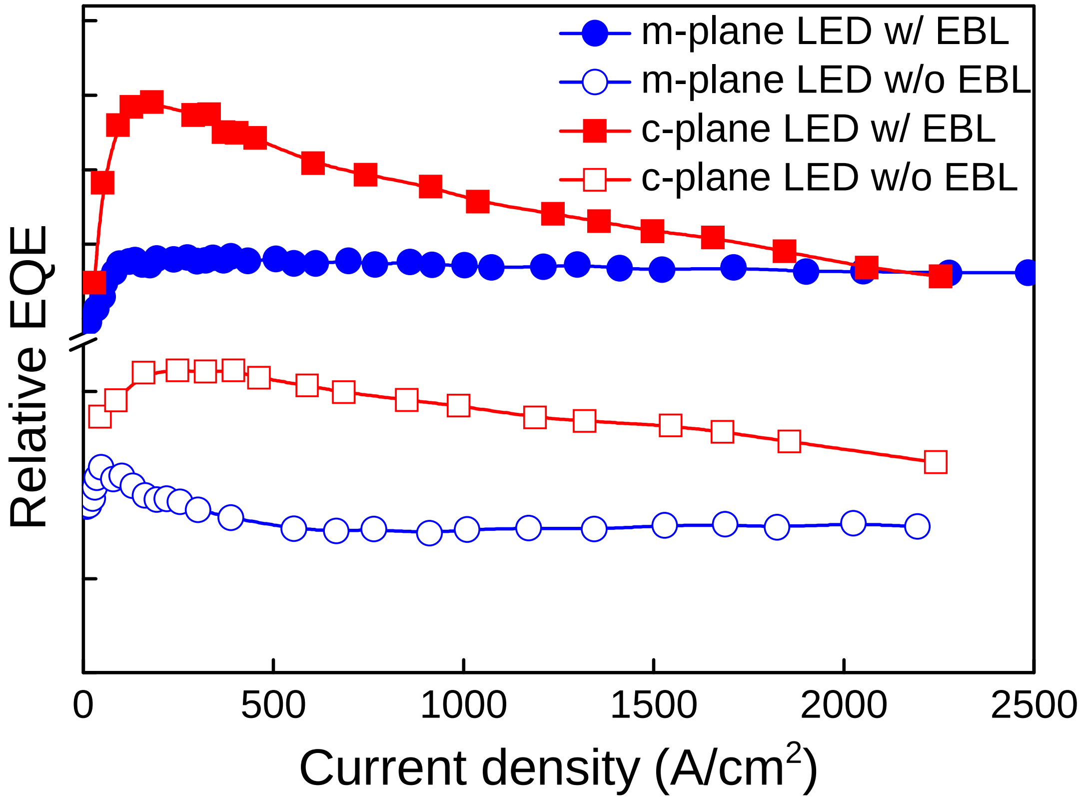

**Figure 2.6** Relative EQE values of c- and m-plane LEDs with and without EBL as a function of current density applied by the pulsed current source**.**

### 2.3.4 Conclusions

IQE of m-plane LED from excitation power dependent PLs was much higher than c-plane LED under the resonance excitation condition, which is indicative of superiority of m-plane QWs. Relative EQE of c- and m-plane LEDs with EBL showed much better performance in terms of the maximum EQE and the efficiency droop than those without EBL. The fact that m-plane LED, of which QWs are free of polarization, without EBL shows worse performance indicates that electron spillover to p-GaN side is the main reason of the efficiency droop in LEDs at high current level.

# Chapter 3 Ways to mitigate efficiency droop

## 3.1 Hot electron overflow model

### 3.1.1 Brief introduction to the model

In previous work completed by Dr. Xianfeng Ni, electron overflow caused by thermionic emission can be neglected even in the structure without EBL. We must therefore turn our attention to non-equilibrium electrons, in other words hot electrons, inside the $In_{0.15}Ga_{0.85}N$ (the particular composition used in our experiments) active region. The injected hot electrons can traverse the active layer by ballistic or quasi-ballistic transport and recombine in the p-GaN region instead of the active region. We should note that the nonradiative recombination is prevalent in p-type GaN due to extremely long lifetime. Dr. Ni used first-order estimation of the hot electron effect and explained our experimental data with varying barrier height of the EBL. The calculation assumes that the electrons obey the Fermi-Dirac distribution in the n-GaN layer before they are injected into the active region. The electrons acquire the additional kinetic energy equal to the conduction band offset between *n*-GaN and $In_{0.20}Ga_{0.80}N$ ($\Delta E_{c},$ ~0.5eV in this case) upon injection. These hot electrons would either undergo thermalization and lose their excess energy mainly through interaction with LO-phonons[28] or avoid thermalization and escape the InGaN region as depicted in **Figure 3.1**.

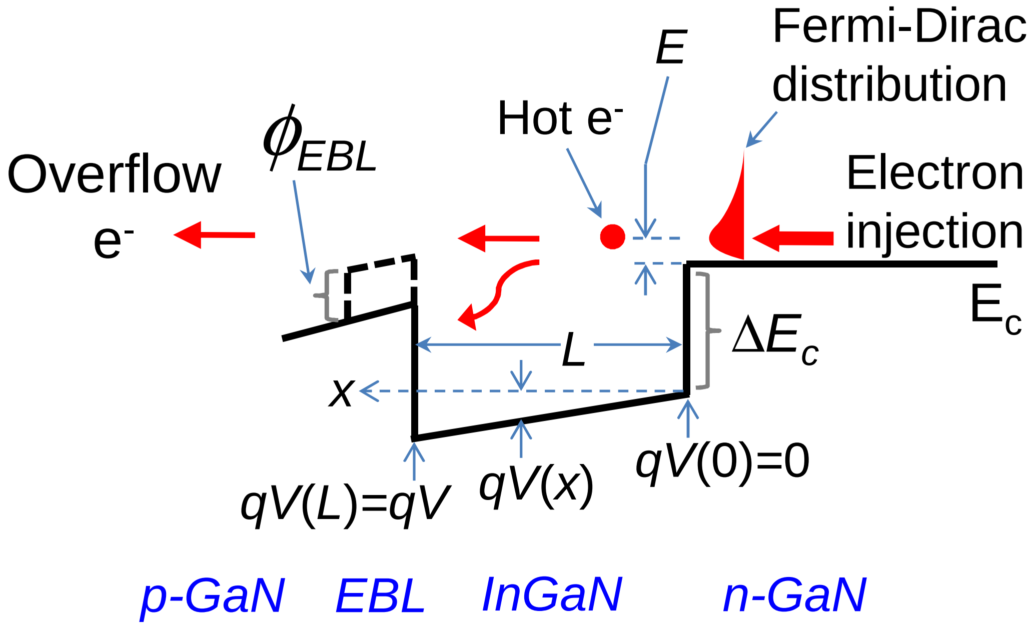

**Figure 3.1** Schematic of electron overflow caused by ballistic or quasi-ballistic electron transport across the InGaN active region. The electrons gain a kinetic energy after being injected into InGaN, which equals to $E+\varDelta E_c+qV(x)$. These hot electrons will either traverse the active region ballistically and quasi-ballistically, escape recombination inside InGaN, and contribute the electron overflow current, or be thermalized and captured inside the active region through interactions with LO-phonons.

His calculations on the hot electron overflow took into account the ballistic electrons, representing those that experience no scattering in the active region, and the quasi-ballistic electrons that experience one scattering event (i.e. quasi-ballistic motion involving either LO phonon emission or absorption), and two scattering events (4 combinations of two scattering events involving LO phonon emission and absorption). Those experiencing multiple energy loosing scattering events are eventually thermalized. In the calculations the electrons are categorized according to their scattering events that they experience: no scattering, one scattering event (one LO phonon emission or one LO phonon absorption), etc. He also demonstrated that the calculated contribution of electrons undergoing two scattering events to the overflow is less than 1% of the total injected electrons and can be neglected for a 6 nm thick active region as in our experimental device structures. Based on the following three scattering events: (1) – no scattering, (2) – one phonon emission, (3) – one phonon absorption, the hot electron overflow can be estimated. As shown in **Figure 3.2** (a), the calculated electron overflow portion is reduced substantially for the m-plane LED (lack of polarization field) with 15% AlGaN EBL compared to that of without EBL, which is correlated well with the experimental data presented above in section 2.3. As indicated in **Figure 3.2** (b), the calculated overflow current increases with the applied voltage. Particularly, with highest bias applied 16V, the structure without EBL exhibits almost 80% of electron overflow. In other word, only 20% of electron can be recombined inside the active region including both radiative and non-radiative recombination.

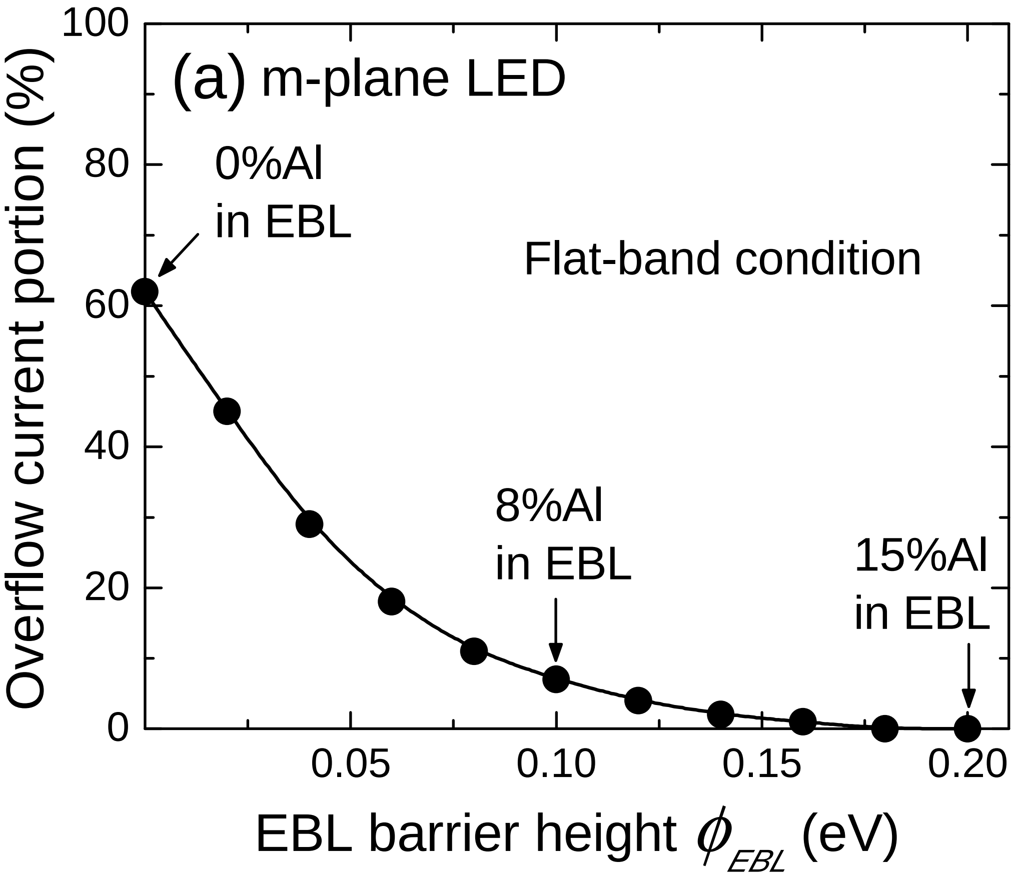
(a) m-plane LED
0%Al
in EBL
Flat-band condition
8%Al
in EBL
15%Al
in EBL
Overflow current portion (%)
0
20
40
60
80
100
0.05
0.10
0.15
0.20
EBL barrier height $\phi_{EBL}$ (eV)

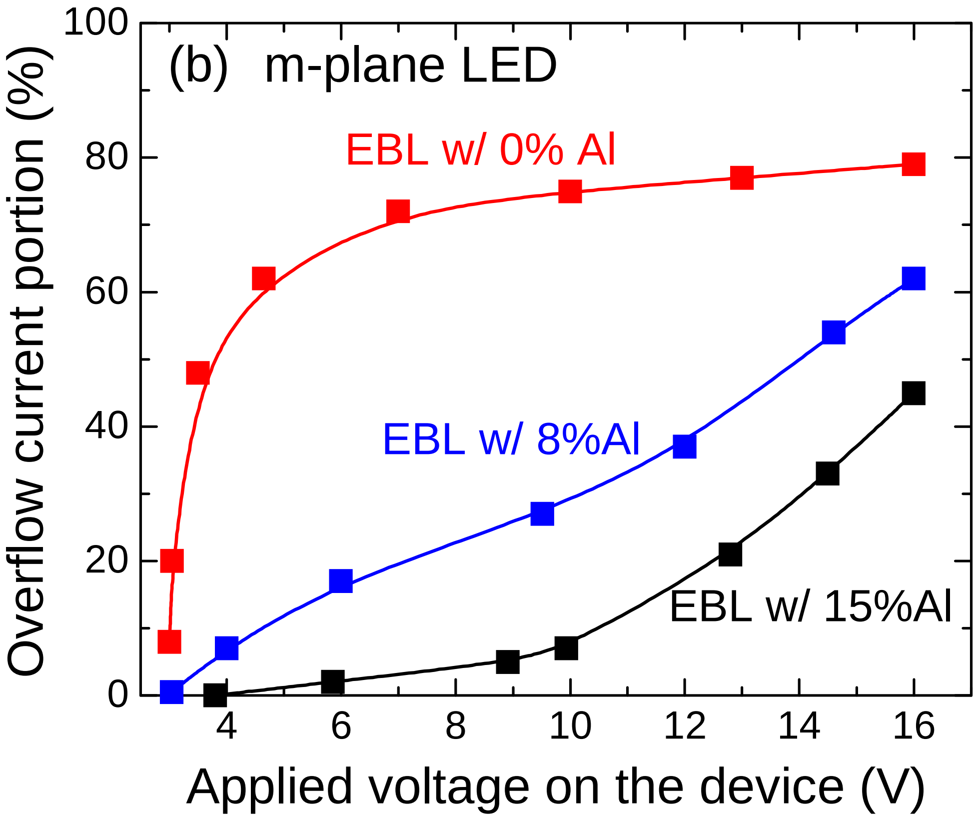

**Figure 3.2** (a) Calculated ratio of the overflow electron current to the total current as a function of the EBL barrier height ($\phi_{EBL}$) in non-polar m-plane LEDs, assuming flat-band conditions in the active region (i.e. 0V net potential drop across the InGaN active region after the applied external voltage compensates the built-in potential, which is ~0.5V), corresponding to 3.8, 4.0, and 4.7 V externally applied bias for the LEDs with 15%, 8%, and 0% Al in the EBL, respectively. (b) Calculated ratio of overflow electron current to the total current as a function of the applied voltage (forward direction) across the m-plane LEDs with three types of EBLs: 0% Al, 8% Al and 15% Al. The symbols in (a) and (b) represent the calculated points whereas the lines are guides to the eye.

### 3.1.2 Stair-case injector (SEI) designs

In this section, we will concentrate on the designs of the SEI structures for optimum impact. Theoretically, thicker SEI can provide more possibilities for electrons to thermalize down to be able to enter the active region. However, due to the growth technical limitations, thicker InGaN SEI layers have better chance to be relaxed and thus more threading dislocations could be generated and penetrated into the active region leading to the much increased non-radiative recombination. Based on the electron overflow model, Ni calculated the percentage of electron overflow with varying SEI step height ($\Delta E_c$) and thickness (*d*) with one layer intermediate SEI structure. The schematic structure is shown in **Figure 3.3**.

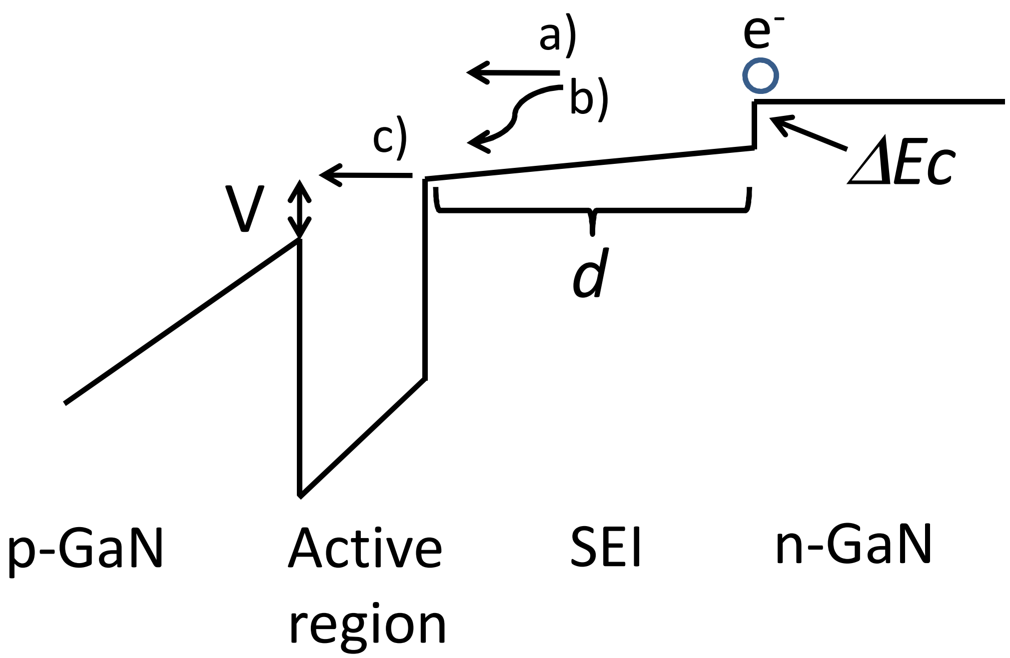

**Figure 3.3** A schematic for the conduction band of a LED with a one-intermediate layer SEI (of thickness d and step height $\Delta E_c$). After being injected into the SEI from the n-GaN region, some electrons will have ballistic and quasi-ballistic, while the others

(experiencing two or more scattering events) are considered to be thermalized in the SEI. For the calculations, the conduction band discontinuity between the active region and p-GaN is assumed to be 0.5eV, and no EBL is employed.

**Table 3-1**. Calculated electron overflow percentiles for a one-layer SEI, with varying SEI step height ($\Delta E_c$) and SEI thickness (*d*).

| $\Delta E_c$ (eV) | *d* = 3 nm | *d* = 9 nm | *d* = 15 nm |
|---|---|---|---|
| 0.1 | 36% (70%) | 18% (66%) | 11% (61%) |
| 0.2 | 37% (52%) | 18% (38%) | 11% (21%) |
| 0.3 | 39% (51%) | 21% (36%) | 11% (22%) |
| 0.4 | 41% (52%) | 24% (39%) | 13% (26%) |
| 0.5 | 42% (53%) | 26% (42%) | 18% (29%) |

The calculated percentiles of electron overflow for the one-intermediate layer SEI with varying step height ($\Delta E_c$) and thickness (*d*) are shown in Table 3-1. Under the flat-band condition (*i.e.* the net potential drop across the active region V = 0), the 15 nm-thick SEIs with step heights of 0.1, 0.2, and 0.3eV all result in a minimum overflow percentile of 11% among the cases included in the table. It should be noticed that the 0.5 eV step height case, which basically corresponds to an increased active region thickness that would enhance thermalization of electrons within the active region, results in an increased electron overflow percentile of 18%. Under the bias corresponding to V=0.1V drop across the active region, the overflow for the 15 nm-thick SEI having a step height of 0.1eV increases to 61% due to a significant increase of overflow contribution from the electrons thermalized in the SEI but traversing the active region ballistically and or quasi-ballistically without recombination since the applied bias lowers the conduction band of p-GaN to the same level as that of the SEI. For the same bias condition corresponding to V=0.1V, the SEI structures with the step heights of 0.2eV or 0.3eV and a thickness of 15nm have comparable electron overflow percentiles (21% *vs*. 22%), and therefore, both could be regarded as the optimum one-layer SEI design for this particular SEI thickness. However, at higher applied voltages (e.g. V=0.2V) across the active region, it is expected that a 0.3eV or larger step height will yield a minimum overflow percentile. These results suggest that for the one-intermediate layer SEI case, a sufficiently large step height and a larger SEI thickness will reduce the electron overflow (an optimum step height for the SEI would provide a balance between the gained electron kinetic energy in the staircase region and the overflow contribution from the electrons thermalized within the SEI). However, growth related issues as mentioned earlier should also be taken into consideration when optimizing the SEI layer stack, which will be discussed in details later.

### 3.1.3 Why SEI not EBL

A universal solution in the InGaN based LED structures to prevent electron overflow is to employ *p*-AlGaN EBL. However, it should be noted that the EBL is known to impede hole injection due to the valence band offset between it and *p*-GaN. Moreover, the AlGaN EBL is located on top of the InGaN barrier of the active region, and the lattice mismatch between AlGaN and InGaN generates piezoelectric polarization field in addition to differential spontaneous polarization fields, they pull down the conduction band at the AlGaN/InGaN interface. As a result, the effective barrier height of the AlGaN EBL is a compromise, and the electron overflow is not effectively suppressed.[29] The effective barrier height of the AlGaN EBLs can be bolstered with higher Al composition at the expense of generation of additional strain-induced defects and larger piezoelectric polarization field. The larger built-in field might lead to band bending and poor carrier confinement and hence could degrade the radiative recombination rate at higher injection levels. Moreover, *p*-type doping in AlGaN is very difficult owing to the high activation energy of Mg acceptor in AlGaN layer (~ 400 meV for 30% Al[30]). As such, the *p*-type EBL conductivity will be reduced and device performance degraded.

As discussed in previous section, SEI can reduce the electron spillover by gradually thermalizing down the hot electrons without blocking hole injection. Experimentally, we have successfully reduced the electron overflow and the associated efficiency loss by inserting, before the InGaN active region, an InGaN SEI with a step-like increased indium composition to act as an "electron cooler".[31,32] LED structures grown on non-polar *m*-plane bulk GaN with 6-nm DH active region show almost identical dependence of EQE on current density when they contain either a three-layer SEI only or both the SEI and an EBL, while the first-order calculations of the electron overflow at different applied forward voltage lead to a high overflow percentage from 60% to 90% for the LEDs without any SEI and EBL and this percentage can be significantly reduced down to 10-20% by inserting the SEI only. Furthermore, the first order calculation for the *c*-plane 6-nm DH LEDs reveals that the electron overflow for the LED with one-layer SEI (no EBL) saturates at ~18% once the applied voltage exceeds 6 V, while the overflow increases with the applied voltage from 0% to 50% when the voltage increases from 3 to 14 V for the LED with EBL if no SEI is incorporated. Therefore, most of the investigated

LED structures in this thesis have incorporated SEI structures without putting EBL unless indicated specifically.

## 3.2 Impact of active layer design, electron cooler, and EBL

### 3.2.1 Motivation

We have undertaken a series of investigations to unveil the root cause of the dominant efficiency degradation mechanism. Experiments conducted on LEDs with and without AlGaN electron blocking layer (EBL) grown on both *c*-plane and *m*-plane GaN substrates indicated that severe electron overflow resulted in a substantial EL efficiency loss by 70% or more if no EBL was incorporated. This clue shows that the leakage to be most likely due to the ballistic electrons that cross the active region and recombine with the holes outside where the recombination is predominantly nonradiative. In this section, LEDs with various active regions have been designed. Some of them incorporated single thicker active layer and some of them have reduced barrier thickness and height favoring hole transport. The structure with SEI only was compared to the one with EBL only leading to the conclusion that SEI is more beneficial to EQE improvement.

### 3.2.2 LED structures

We examined LED structures with different active-region designs and aimed at reducing the electron overflow (better efficiency retention at high injection current density) as well as improving the quantum efficiencies. In this realm, MQW LED structures with EBL (without SEI), and without EBL but with SEI, and further with different InGaN barrier heights (namely $In_{0.06}Ga_{0.94}N$ and $In_{0.01}Ga_{0.99}N$) and thicknesses (namely 3 nm and 12 nm) are compared and analyzed. Moreover, the DH active regions, where hole diffusion is not obstructed by the interwell potential barriers, are also investigated for comparison. Additionally, the quantum efficiency of the LEDs with sole SEI is compared with that of sole EBL having the same active regions, *i.e.* uncoupled MQW.

The LED is listed in Table 3-2. Five of the investigated LEDs incorporated SEI between the underling $In_{0.01}Ga_{0.99}N$ layer and the active region. The SEI consists of two 5-nm InGaN layers (two-layer SEI) with step-increased In composition of 4% and 8%, in the given order, again inserted before the active region. The steps having potential energy drop equal or more than one LO phonon energy (88 meV) contribute to electron thermalization through electron–LO-phonon interaction.

**Table 3-2** Structural details of LEDs investigated.

| LED Structure | Well Indium composition | Well thickness (nm) | Barrier Indium composition | Barrier thickness (nm) |
|---|---|---|---|---|
| Uncoupled-MQW | 14% | 2 | 1% | 12 |
| Uncoupled-MQW-LB | 14% | 2 | 6% | 12 |
| Uncoupled-MQW-EBL | 14% | 2 | 1% | 12 |
| DH | 14% | 9 | N/A | N/A |
| Coupled-MQW-LB | 14% | 2 | 6% | 3 |
| Coupled-MQW | 14% | 2 | 1% | 3 |

### 3.2.3 Uncoupled MQWs

**Figure 3.4** (a) shows the results for the LED structures with uncoupled-MQW, uncoupled-MQW-LB, and uncoupled-MQW-EBL. Detailed LED structures can be found in Table 3-2. The measured IQE values reached 90% at a carrier density of $3\times10^{18}$ cm$^{-3}$ for the uncoupled-MQW LED with SEI and 93% at a carrier density of $3\times10^{18}$ cm$^{-3}$ for the MQW-LB-LED with SEI, and continued to increase for higher carrier densities

[**Figure 3.4** (a)]. Although it is not quite pronounced, the lowered InGaN barrier height, *i.e.* $In_{0.06}Ga_{0.94}N$, slightly enhanced the IQE at both low and high carrier densities. We can also observe that the uncoupled-MQW-EBL-LED, which does not have an SEI, shows about 10% lower IQE values consistently as compared to the uncoupled-MQW-LED having only SEI. This demonstrates that the IQE value is improved by inserting SEI instead of using EBL. This might be due to the degraded layer crystalline quality by the strain-induced defects in the LED with AlGaN EBL. **Figure 3.4** (b) displays the extracted IQE values *vs.* photocurrent converted from the carrier density using the rate equation (naturally being resonant optical excitation calls for no carrier leakage) as described in Ref. 33. As indicated in **Figure 3.4** (b), the IQE values of LEDs with uncoupled MQW active regions (either with $In_{0.01}Ga_{0.99}N$ or $In_{0.06}Ga_{0.94}N$ barrier) reach 80% at photocurrent densities below 30 A/cm$^2$. **Figure 3.4** (c) shows the relative EQE values for the MQW-LED structures. Among them, the uncoupled-MQW-LB-LED exhibited the highest EQE value and reached a maximum at a current density of around 40 A/cm$^2$, while the EQE of the uncoupled-MQW-LED with $In_{0.01}Ga_{0.99}N$ barrier reached the maximum at a same current level (~40 A/cm$^2$) but suffers more efficiency degradation in relation to the one with reduced barrier with increasing injection current. As shown in **Figure 3.4** (c), the relative EQE for the uncoupled-MQW-LB-LED is approximately 15% higher than that for the uncoupled-MQW-LED under current density ~600 A/cm$^2$. It is well known that the hole transport in GaN is compromised due to the large hole effective mass causing low hole mobility (~5 cm$^2$/Vs). The reduced InGaN barrier height ($In_{0.06}Ga_{0.99}N$) in the MQW active regions could favor the hole transport and thus reduce the electron overflow induced efficiency degradation at high injection levels as the probability of recombination in the active region would increase with more holes present. Therefore, improved quantum efficiency would be expected with reduced InGaN barriers in MQW-LEDs.

Our investigations also sought to undertake a comparative analysis of uncoupled MQW-LED having only SEI with the uncoupled LED having only EBL in terms of both IQE and EQE. As shown in **Figure 3.4** (b), the uncoupled MQW-LED with SEI shows 18% higher IQE than the uncoupled MQW-LED with EBL but without SEI (uncoupled-MQW-EBL) under the same carrier density ~$2\times10^{18}$ $cm^{-3}$. This improved IQE of LEDs with SEI can be attributed to improved crystalline quality due to the absence of any strain induced defects and to more efficient hole injection into the active region, which would have been limited by low hole mobility in AlGaN. Similarly, the uncoupled-MQW-LED shows 12% higher peak EQE than the uncoupled-MQW-EBL-LED at lower injection levels though they tend to converge at higher injection levels, as shown in **Figure 3.4** (c). One can argue then that the efficiency is improved when LEDs use SEI instead of AlGaN EBL.

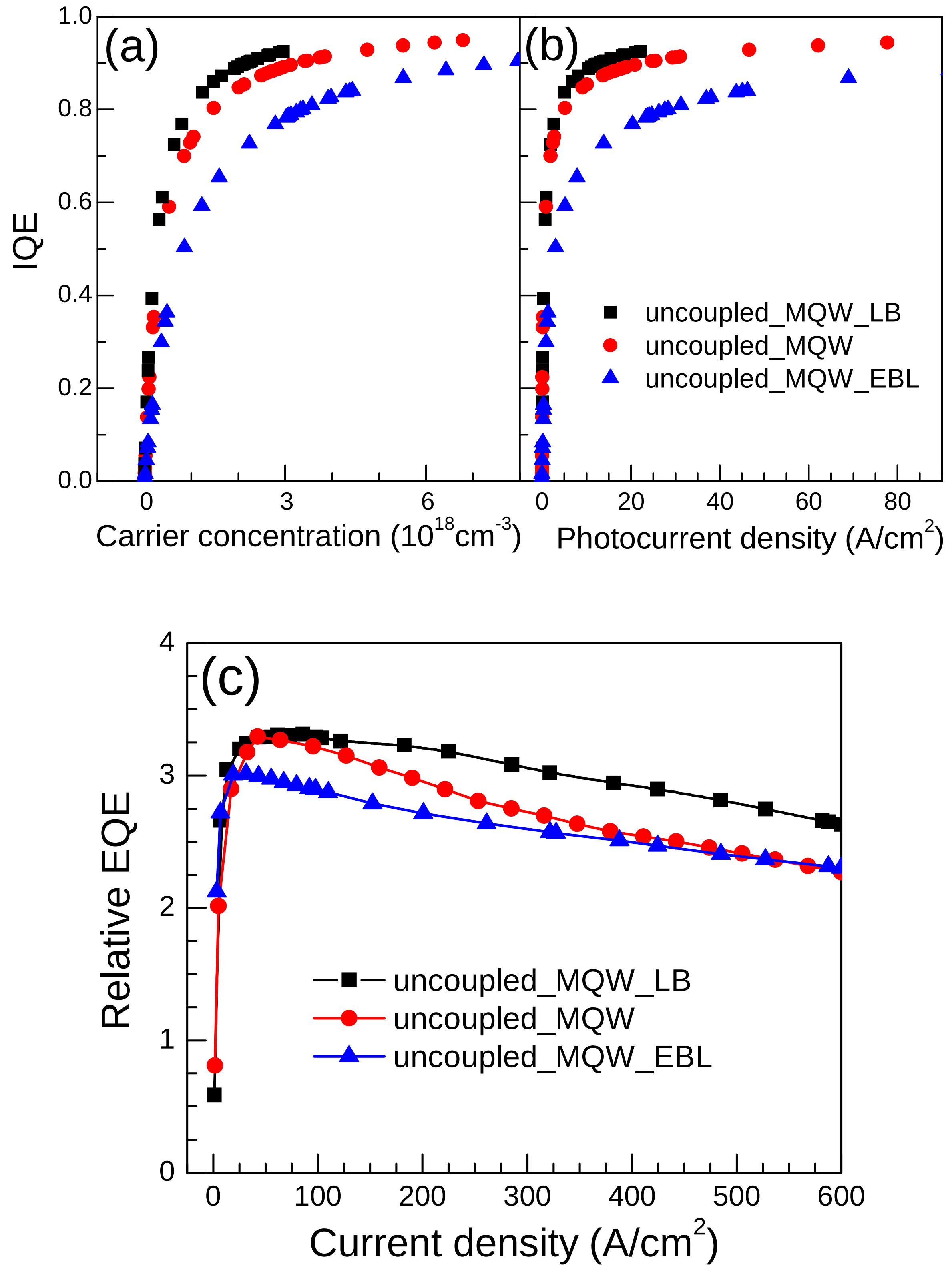

**Figure 3.4:** (a) IQE values determined from excitation-dependent PL for LEDs with

uncoupled MQWs; For the calculation of carrier densities, the *B* value was assumed to be $10^{-11}$ $cm^3s^{-1}$; (b) IQE values *vs.* electron density converted from carrier density using rate equation; (c) Relative external quantum efficiencies of uncoupled LEDs as a function of pulsed injection current density.

### 3.2.4 Coupled MQW-LEDs and DH-LED

Compared to the uncoupled MQW LEDs, the coupled MQW and DH LEDs exhibit lower IQE values and slower rate of increase in the IQE with generated electron (hole) concentration as shown in **Figure 3.5** (a). The maximum IQE for the 9-nm DH-LED is only 60% at a carrier density of $4.5\times10^{18}$ $cm^{-3}$. The relative EQE data obtained in this LED structure are consistent with the relatively low IQE (discussed below). The 9-nm DH-LED shows lower EQE values than those of coupled-MQW-LB-LEDs at current densities below 60 A/$cm^2$. The coupled-MQW-LB-LED and coupled-MQW-LED reach the maximum IQE value of 84% and 79%, respectively, at the carrier density of about $6\times10^{18}$ $cm^{-3}$. This appears to bode well for the low InGaN barrier height sample in terms of IQE, most likely due to strain and quality considerations and absorption in the low $In_{0.06}Ga_{0.94}N$ barrier. The LED structures with coupled MQW active regions (either $In_{0.01}Ga_{0.99}N$ or $In_{0.06}Ga_{0.94}N$ barrier) exhibit a much slower rise in the IQE values [80% is reached at the maximum equivalent photocurrent density of 90 A/$cm^2$] when compared with uncoupled MQWs [80% IQE is reached ~30 A/$cm^2$, **Figure 3.4** (b)] .

As shown in **Figure 3.5** (c), the 9-nm DH-LED exhibits the highest EQE value at high injection levels, *i.e.* beyond a current density of 60 A/$cm^2$ and reaches a maximum at a current density of approximately 150 A/$cm^2$. The maximum relative EQE for the 9-nm DH-LED is approximately 25% higher than that for the MQW-LED with coupled quantum wells and low InGaN barriers. However, at low injection levels, *i.e.*, below 60 A/cm$^2$, the 9-nm DH-LED has relatively slower EQE rate of increase with current density compared to that of MQW-LEDs. This observation is consistent with the IQE values determined by excitation dependent resonant PL measurements. In 9-nm DH-LED structures, a triangular potential well exists at the interface due to the piezoelectric and spontaneous polarization fields as shown in **Figure 3.5** (b). The energy band profiles were calculated at a forward bias of 4V (above threshold) using the Silvaco Atlas simulation software. Note that due to the large thickness, the linear electric field model applicable in thin layers would give rise to a non-linear behavior which is depicted in **Figure 3.5** (b). Therefore, at low injection levels, electron and hole wavefunctions are widely separated due to the thicker active region, which results in reduced radiative recombination rate and relatively low relative EQE. Furthermore at low injection levels, the available states of this triangular potential well are not completely filled. Upon increasing the injection level the triangular well will be fully occupied, due to relatively low density of states. With further increase of injection, the quasi-continuum states followed by the three dimensional states in the DH active region will begin to fill and contribute to emission leading to higher recombination rate and thus higher relative EQE.

In support of the above argument, **Figure 3.6** (a) shows the peak energy shift as a function of injection current density for the MQW and DH LED samples. For the 9-nm DH LED a nearly rapid and large blueshift (25 meV) is observed within the initial 45 A/cm$^2$ compared to the 5 meV shift for coupled and uncoupled MQWs within the same injection range. This initial rapid change can be attributed to the band filling of the triangular well as mentioned above. As the injection level is further increased, both the

MQW and the DH LED samples exhibit a monotonic blueshift due to screening of the built in polarization field. However, it should also be noted that the InGaN active layer quality has been known to degrade with increasing thickness. Therefore, one should expect the nonradiative recombination rate to increase, lowering the quantum efficiency particularly at low injection levels. The relative importance of the two aforementioned processes, one affecting the radiative recombination coefficient and the other affecting the non radiative recombination rate is under further investigation.

We note the hole diffusion is not obstructed by the InGaN barriers in DH active regions, and hence electrons and holes that are present can recombine more easily barring the complication caused by the induced field. We suggest that due to the relatively enhanced hole transport through the low InGaN barrier in MQW active regions. As in the uncoupled MQWs this trend holds for coupled MQWs as well. The coupled MQW LB-LED shows 27% higher EQE than the nominally coupled MQW-LED with $In_{0.01}Ga_{0.99}N$ barriers as shown in **Figure 3.4** (c). Comparing the coupled-MQW-LB-LED [see **Figure 3.4** (c)] to the uncoupled-MQW-LB-LED [see **Figure 3.4** (c)], the peak EQE for the former is 25% higher than that for the latter, which confirms our previous report stating that the coupled MQWs with 3 nm barriers would help provide a more uniform hole population among the 6-period quantum wells than the uncoupled MQWs. This is consistent with the calculated band diagrams at an applied forward bias of +6 V. We further suggest that in the uncoupled (12 nm barrier) MQW-LED, the hole concentration dominates in the QW near the *p*-side, while for the coupled (3 nm barrier) MQW-LED holes can be more uniformly distributed across all the QWs. Therefore, all the 6 wells are more likely to participate nearly fully in the recombination process in coupled MQW-LEDs, which thereby reduces the excess electron density and thus electron leakage.

As for the efficiency degradation ratio (taken as the EQE value at 600 A/cm$^2$ relative to the maximum EQE), the LEDs with coupled MQW active layers show smaller degradation ratios compared with the uncoupled MQW counterparts. A coupled-MQW-LB-LED investigated shows negligible efficiency degradation while the uncoupled-MQW-LB-LED counterpart shows 25% degradation. This can be attributed to the enhanced hole distribution through thinner barriers. This is further supported by experiments in which the barrier height, controlled through In mole fraction, in the quantum well region is varied. For instance, the coupled-MQW-LB-LED with lower barriers in the quantum well region shows negligible efficiency degradation while the coupled-MQW-LED with higher barriers shows 10% degradation. We should also mention that EQE values reach their maximum at current densities ranging from 20-70 A/cm$^2$ in the MQW-LEDs, depending on the LED active layer structure. This observation as well is consistent with the IQE data shown in **Figure 3.4** (b) and **Figure 3.5** (b).

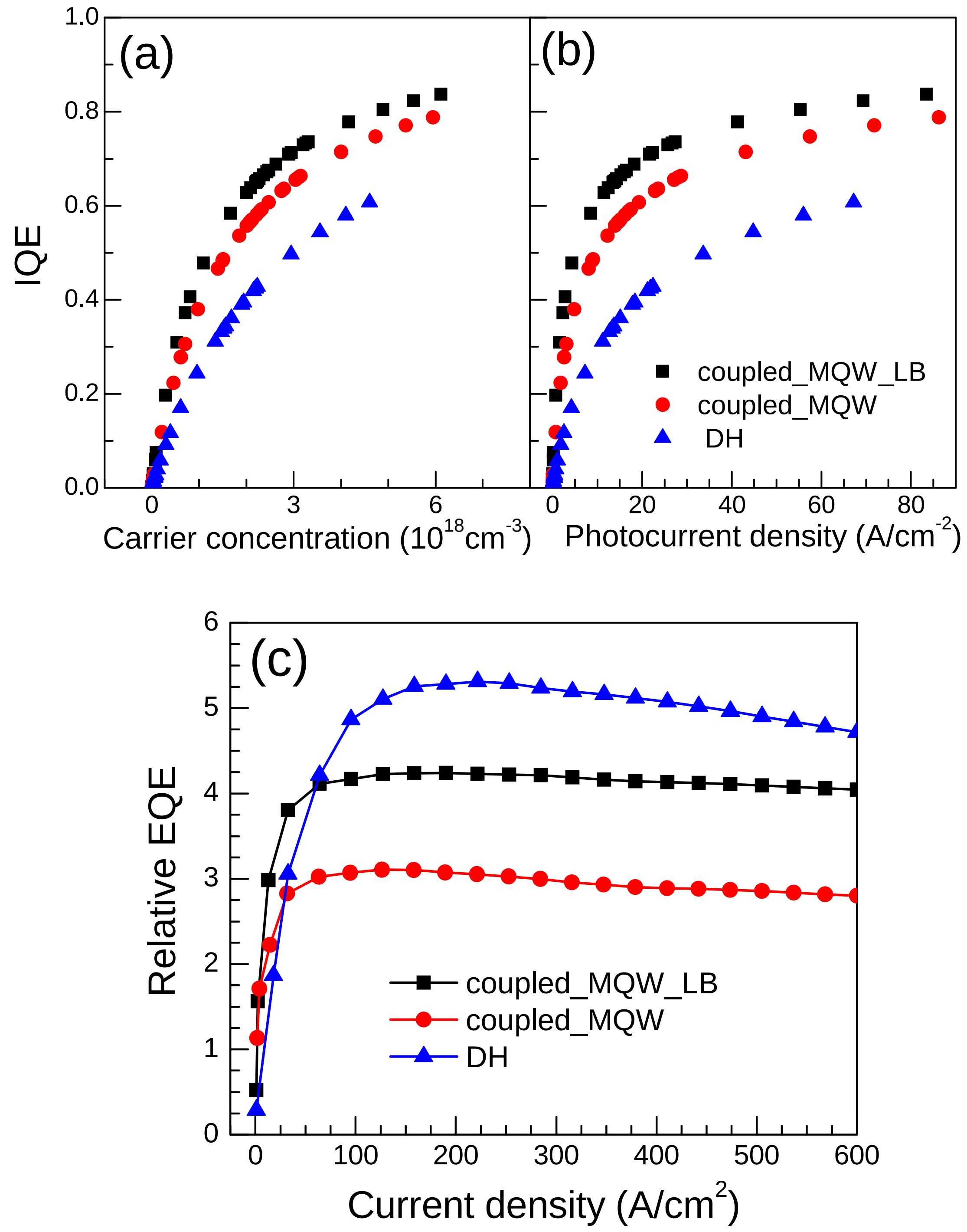

**Figure 3.5:** (a) IQE values determined from excitation-dependent PL for LEDs with coupled MQWs and DH; For the calculation of carrier densities, the *B* value was assumed to be $10^{-11}$ cm$^3$s$^{-1}$; (b) IQE values *vs.* photo current density converted from carrier density using rate equation (Equation 1); (c) Relative external quantum efficiencies of coupled

MQW and DH LEDs as a function of pulsed injection current density (0.1 % duty cycle and 1 kHz frequency). The relative values of EQE can be compared with those in Figure 1 (c);

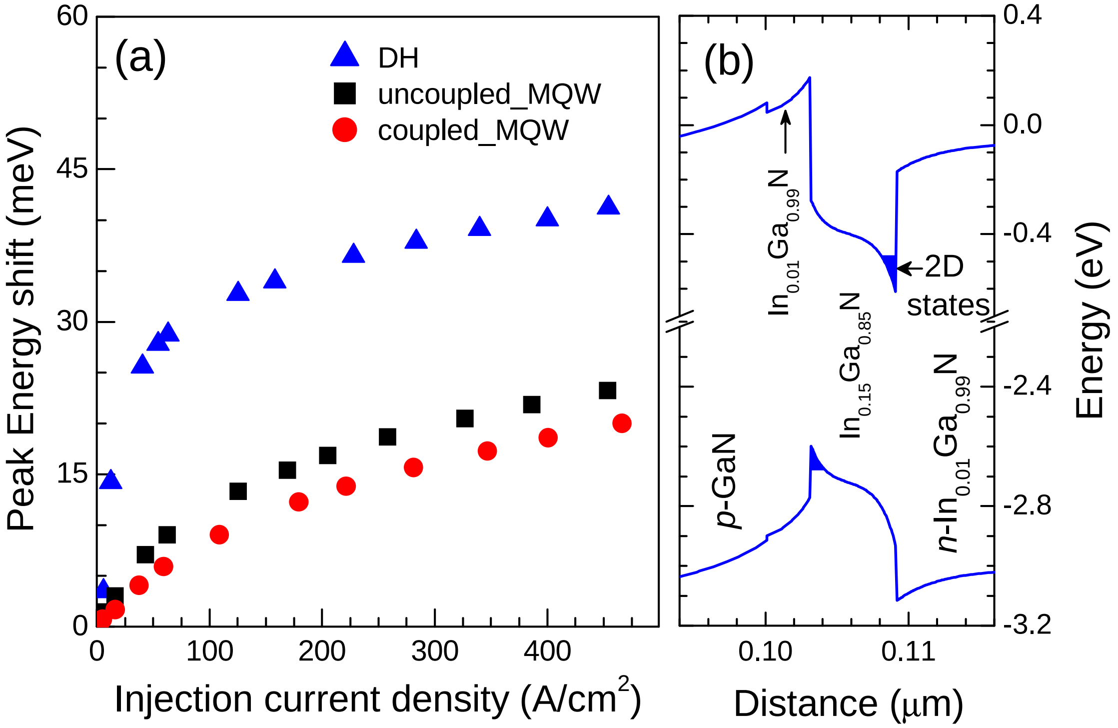

**Figure 3.6**: (a) Peak energy shift as a function of injection current density for DH, uncoupled MQW and coupled MQW LEDs. (b) Energy band edge profiles calculated at 4V forward bias (corresponding to 35 A/cm$^2$) for the DH LED (SEI is not included in simulations for a clearer picture).

### 3.2.5 Conclusion

With electron overflow in mind, which is a detrimental factor in LEDs, we investigated the dependence of both IQE and EQE on the induced electron density and injection current density for InGaN based LEDs with various active layer designs: both DH and MQWs, InGaN barrier thickness (3 nm and 12 nm), barrier In composition (1% and 6%), sole SEI (without EBL) and sole EBL (without SEI). The IQE values deduced from the excitation dependent resonant PL measurements for the uncoupled- MQW-LEDs reached above 93% at a carrier density of $3x10^{18}$ $cm^{-3}$, which is higher than those for the coupled-MQW LEDs (~70%) and the DH-LED (~51%) at the same carrier density. However, the EL measurements at various injection levels revealed that 9-nm DH-LED has the highest EQE values beyond 60 $A/cm^2$ though the figure is lower below this injection level. This is attributed to the interfacial triangular quantum well with low density of states that results in spatial separation of the electrons and holes reducing the radiative efficiency. Furthermore, the EQE of 9 nm DH-LED can be retained up to the maximum injection current density 600 $A/cm^2$, the highest used in experiments, with small degradation ~10%. Moreover, the EQE was retained in the coupled-MQW-LB-LEDs with low barriers in the quantum well active region at levels up to 600 $A/cm^2$. The reduced InGaN barrier height in the coupled MQW design not only enhanced the EL intensity but also greatly reduced the efficiency degradation ratio, defined by the peak efficiency relative to the efficiency at 600$A/cm^2$.

The EBL layer can be successfully replaced with SEI in all the LED active layer designs even in the uncoupled-MQW-LEDs with SEI as evidenced by ~12% increase in the peak EQE values at low injection levels compared to that with EBL of the same active region. Overall, by replacing the conventional EBL with SEI and lowering the InGaN barrier height (6%), the latter improving the hole transport through the active region, both the IQE and EQE of LEDs were enhanced. Although the 9 nm DH-LED shows lower IQE at low injection levels, the EQE values are 25% higher than that in the coupled MQW-LED with reduced InGaN barrier at high injection current levels

(>60A/cm$^2$) suggesting that the DH LED structure is superior to the MQW active region LEDs for high power LEDs.

## 3.3 *m*-plane orientation InGaN LEDs

### 3.3.1 Motivation

The use of non-polar m-plane orientation is expected to alleviate efficiency droop issues persistent in c-plane counterparts, owing to the reduced hole effective mass (supplying higher hole concentrations), and predicted large optical matrix elements.[34,35,36] The aforementioned features increase the radiative recombination rate as well as mitigating hole distribution throughout the active region. Moreover, as shown in **Figure 3.7**, in c-axis polar wurtzite GaN epilayers, the internal spontaneous and piezoelectronic polarization effects can cause strong electric field in the nitrides interface, *i.e.*, wells and barriers, wells and EBL. This electric field is a necessity for two-dimensional electron gas formation in field effect transistor devices; but it can also cause spatial separation of electron and hole wavefunction in quantum wells of InGaN LEDs, thereby increasing the radiative lifetime[37] and hence reducing the quantum efficiency[38], and can also cause the red shift of LED emission.

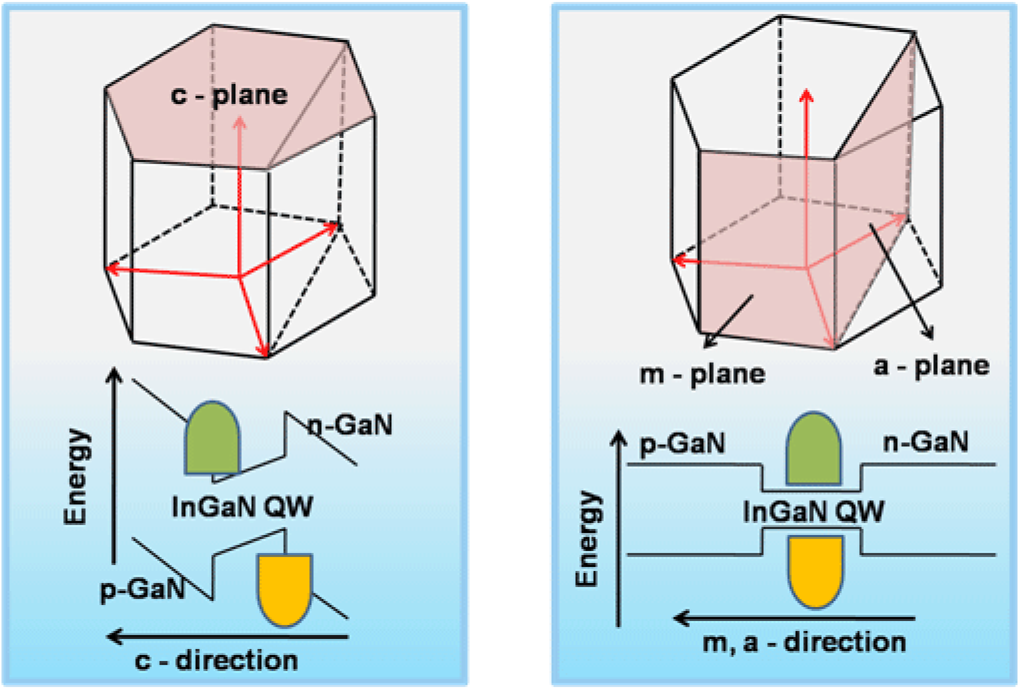

**Figure 3.7** Schematic demonstration of polarization field effect on the band structures in polar c-plane GaN and nonpolar m- and a-plane GaN. The very large electrostatic fields in the polar orientation result in a quantum confined Stark effect (QCSE) and poor electron-hole overlap. The nonpolar orientation is free of electrostatic fields, thus true flat-band conditions are established.

### 3.3.2 Figure print of *m*-plane LEDs

The *m*-plane LEDs were confirmed to exhibit polarized EL due to the in-plane polarization anisotropy in m-plane, which is further enhanced by large valence band splitting induced by the anisotropic biaxial strain within the quantum wells.[39, 40] **Figure 3.8** shows the EL intensity of an *m*-plane LED as a function of the polarization analyzer angle, where 0° corresponds to polarization perpendicular to the c-axis. As can be seen the electric field component of the EL is mainly polarized in the GaN *m*-plane and perpendicular to the GaN *c*-axis. The polarization degree is $\rho = (I_{\perp c} - I_{\|c}) / (I_{\perp c} + I_{\|c}) =$ 0.48, where $I_{\perp c}$ and $I_{\|c}$ correspond to intensities for polarization perpendicular and parallel to the *c*-axis, respectively. This value is comparable to that reported in Ref. 41 (~0.43) for the same emission wavelength (~400 nm) and the same wafer configuration (on-wafer measurement without dicing, no sidewall polishing to reduce light scattering) employed here.

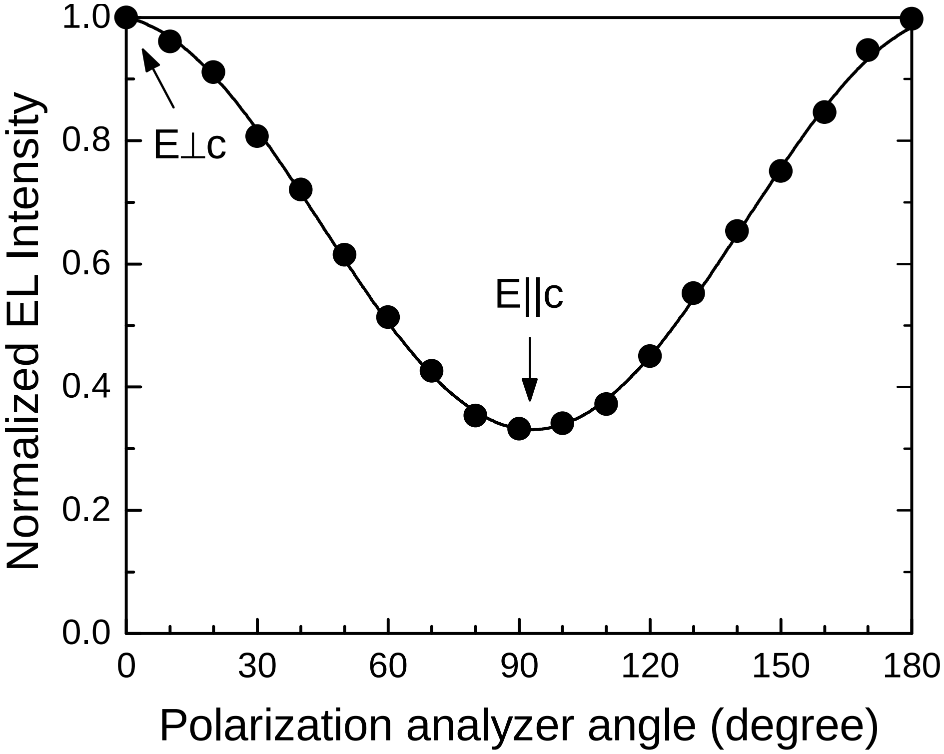

**Figure 3.8**: EL intensity as a function of the polarizer angle of the *m*-plane LED sample grown bulk *m*-plane GaN. The polarizer angles of 0° correspond to the E⊥c and the polarizer angles of 90° correspond to the E||c. The solid line is a guide to the eye.

The degree of polarization has been reported to increase with increasing emission wavelength,[41] which is attributed to increased valence-band splitting caused by larger compressive strain in QWs with increasing In composition.[42]

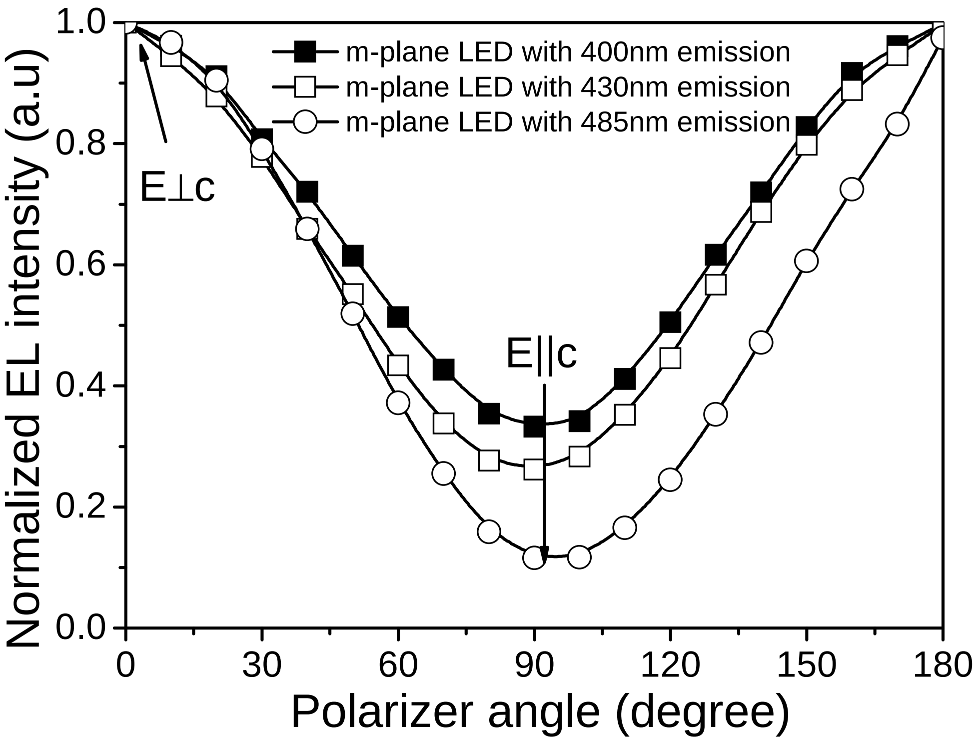

**Figure 3.9**. PL intensity as a function of the polarizer angle of the three *m*-plane LEDs grown on bulk *m*-plane GaN. The polarizer angles of 0° correspond to the E⊥c, while the polarizer angles of 90° correspond to the E||c.

As shown in **Figure 3.9**, the polarization ratio corresponds to intensities of the components polarized perpendicular and parallel to the *c*-axis, respectively, is calculated to be ~0.49, ~ 0.60, and ~0.8 for the 400 nm, 435 nm and 485nm emission wavelength *m*-plane LEDs, respectively.

### 3.3.3 Experimental procedures

Both m-plane and c-plane LED structures were grown on freestanding GaN in a vertical low-pressure metalorganic chemical vapor deposition (MOCVD) system. They are composed of 6 period 2 nm $In_{0.14}Ga_{0.86}N$ quantum wells with 12 nm $In_{0.01}Ga_{0.99}N$ barriers, and a 60 nm Si-doped ($2\times10^{18}$ $cm^{-3}$) $In_{0.01}Ga_{0.99}N$ underlayer just beneath the active region for improved quality. A ~10 nm *p*-$Al_{0.15}Ga_{0.85}N$ electron blocking layer was deposited on top of the active quantum well region. The Mg-doped *p*-GaN layer that followed is about 100 nm thick having $7\times10^{17}$ $cm^{-3}$ hole concentration for the c-plane variety, as determined by Hall measurements on a calibration sample, which is expected to be higher for the m-plane orientation due to lighter hole effective mass for the same Mg chemical content. Meanwhile, another three LEDs comprised of 6 period 2 nm InGaN quantum wells sandwiched between 3 nm $In_{0.01}Ga_{0.99}N$ barriers (thinner barriers favoring hole transport) with various emission wavelengths from 400  to 485 nm were also fabricated in order to investigate the wavelength dependent efficiency droop. Due to the fact that the m-plane LED sample is extremely small, we did not perform Hall measurements. Further details and the schematic of the LED structures can be found in Ref.19. After mesa (250 μm diameter) etching, Ti/Al/Ni/Au (30/100/40/50 nm) metallization annealed at 800 ºC for 60 seconds was used for *n*-type ohmic contacts and 5 nm/5 nm Ni/Au contacts were used for the semi-transparent *p*-contacts. Finally, 30/50 nm Ni/Au contact pads were deposited on the top of part of the mesa. The 500 μm-thick *m*-plane freestanding GaN templates,  produced at Kyma Technologies, Inc.,  have a threading dislocation density of $<5x10^{6}$ $cm^{-2}$ and are off-cut by 0.2° towards the GaN *a*-axis and 0.3° towards the GaN *c*-axis. The *c*-plane freestanding GaN is around 250 $\mu$m thick.

### 3.3.4 Results and discussions

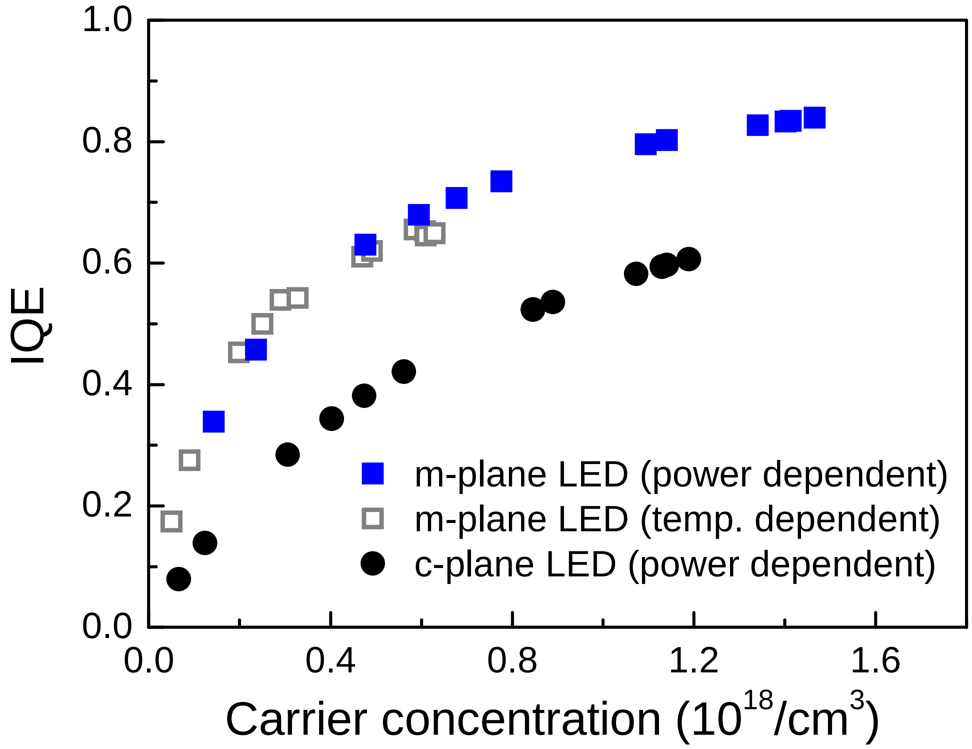

**Figure 3.10**: IQE values determined from power-dependent PL and also temperature-dependent PL measurements for the *m*-plane and *c*-plane LEDs. For the calculation of carrier concentrations, the B value was assumed to be $1\times10^{-11}$ cm$^3$s$^{-1}$.

Both *m*-plane and *c*-plane LED structures are composed of 6 period 2 nm $In_{0.14}Ga_{0.86}N$ quantum wells with 12 nm $In_{0.01}Ga_{0.99}N$ barriers, which will exacerbate the efficiency droop for better comparison. **Figure 3.10** shows the room temperature IQE values of an m-plane LED sample vs. the induced carrier concentration measured from resonant PL measurements using both excitation power-dependence and temperature-dependence.[43] At relatively high carrier concentrations, the IQE values of the *m*-plane LEDs are ~30 % higher than those of their *c*-plane counterparts (80 % and 60 %, respectively, at a carrier concentration of $1.2\times10^{18}$ cm$^{-3}$), which is similar to the aforementioned ones. For confirmation, we also determined the IQE values of the *m*-plane LEDs from temperature-dependent PL at various excitation densities, where IQE at low temperature (e.g. 15 K in our case) was assumed to be 100%.[43] The IQE values extracted as such were nearly identical to those obtained from the excitation density dependence: e.g. 66 % vs. 68 % at a carrier concentration of $1.2\times10^{17}$ $cm^{-3}$. The carrier densities used for the temperature dependent PL were obtained from the intensity-dependent PL measurements at room temperature.

The relative EQE values of the two representative LEDs of different crystal orientation are shown in **Figure 3.11**. The *m*-plane LED shows negligible droop, *i.e.* almost full retention of its efficiency for a current density up to 2500 $Acm^{-2}$ as compared to ~25 % for that on *c*-plane freestanding GaN having the same structure. This observation is consistent with the premise of relatively higher hole concentration and smaller hole effective mass expected in *m*-plane that would favor the transport of holes throughout the active region and reduce the electron spill over (or overflow) and thereby mitigate the efficiency droop. Furthermore, as also evident from **Figure 3.11**, at relatively lower injection levels the EL intensity for the *m*-plane LED increases more rapidly than that for the *c*-plane LED, reaching its peak value at ~140 $Acm^{-2}$ compared to ~400 $Acm^{-2}$ for the c-plane LED, which is indicative of a relatively small Shockley-Reed-Hall nonradiative recombination coefficient for the *m*-plane variety. Among several devices tested for both orientations, *m*-plane LED EQE values are consistently higher by ~ 35 % and even higher at higher injection levels due to better efficiency retention than those of *c*-plane LEDs, which is consistent with the results obtained from the intensity dependent PL measurements. The variation from device to device for each orientation was less than 10 %.

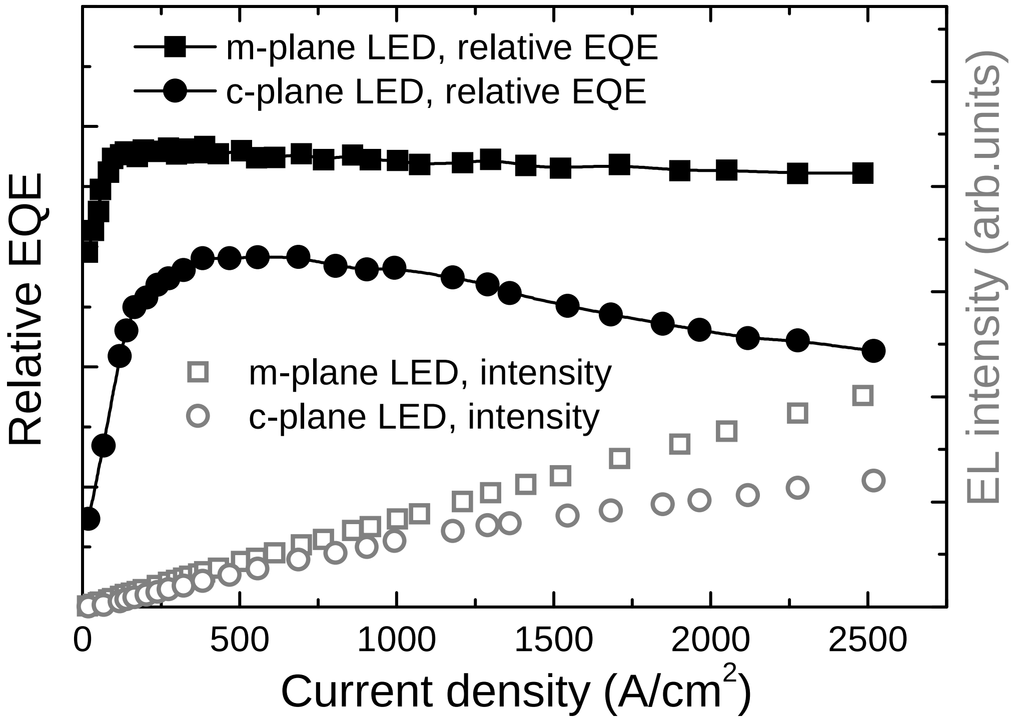

**Figure 3.11**: Relative external quantum efficiency and integrated EL intensity of the m-plane LED on freestanding GaN and the reference LED on c-plane bulk GaN as a function of pulsed injection current density (0.1 % duty cycle and 1 kHz frequency). Both samples have the same device structure.

It is worth to mention that when the emission wavelength of the *m*-plane LEDs is increased from ~ 400 nm to 435 nm the EQE was reduce due to the material degradation with In content whereas the efficiency droop was still negligible. On the other hand, the LED with 485 nm emission shows much more severe efficiency droop compared with the two LEDs with shorter emission wavelength, which might be due to the inferior InGaN (Indium-rich at longer emission wavelength) material quality, as exhibited in **Figure 3.12**.

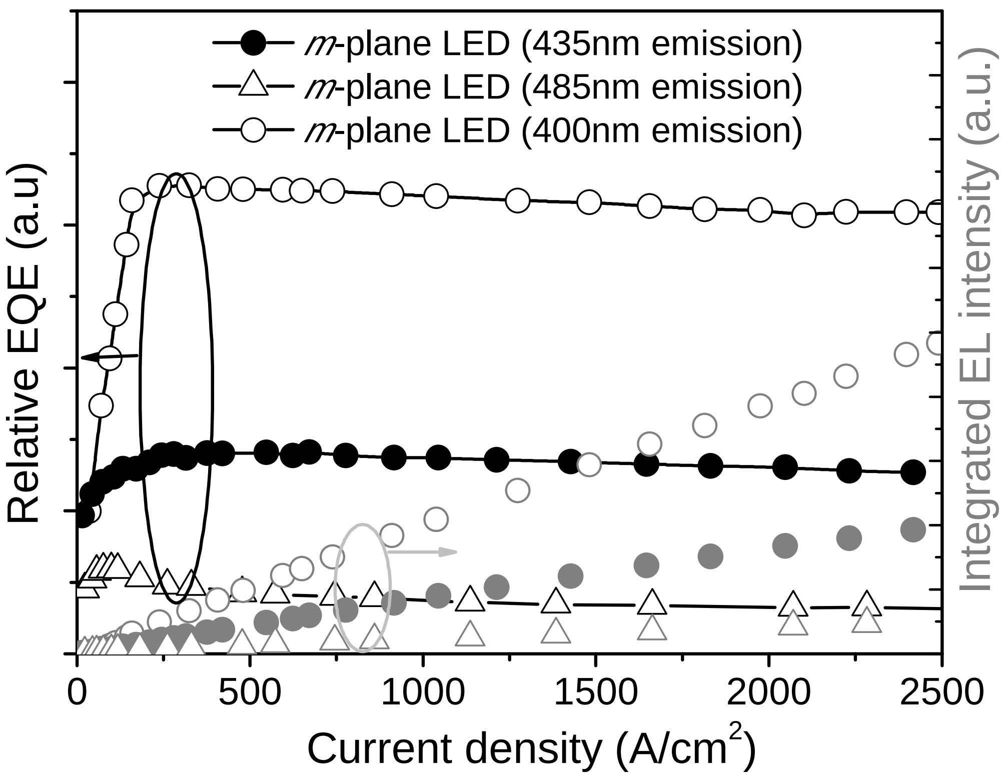

**Figure 3.12** Relative EQE comparison of the *m*-plane LED with different wavelength (400nm, 435nm and 485 nm)

### 3.3.5 Conclusion

IQE values deduced from intensity dependent PL measurements for the *m*-plane LEDs are approximately 30 % higher than those for the *c*-plane LEDs of the same structure. Electroluminescence measurements at various injection levels also revealed more than 35 % higher EQE for the *m*-plane LEDs than *c*-plane LEDs, a factor which increased with injection. More importantly, the high EQE was retained in *m*-plane LEDs at high injection levels up to 2500 Acm$^{-2}$ (only 5 % droop). The LEDs on *c*-plane freestanding GaN exhibited ~25 % droop within the same current injection range. The observations are consistent with the predicted increased optical matrix elements and improved hole concentration/transport in *m*-plane orientation, and absence of polarization.

Determination of the exact mechanism requires detailed further investigations. With increasing emission wavelength for LEDs with 3 nm barriers the material quality degrades owing to the lower growth temperature. However the efficiency droop is not aggravated for 435 nm emission though severe efficiency droop was observed in 485 nm LED.

# Chapter 4 Quantum efficiency enhancement in InGaN-based LEDs

## 4.1 Double heterostructure (DH) active layers

### 4.1.1 Motivation

To retain the quantum efficiency at high current levels a straightforward approach would be to increase the number of QWs in the active region. However, due to the poor hole transport, light is emitted mainly from the QWs closest to the *p*-GaN in typical *c*-plane InGaN/GaN LEDs.[44, 45, 46] An alternative approach is to utilize double heterostructure (DH) active regions ensuring uniform carrier spreading across the active region.[47] Among the ramifications of DH are the loss of InGaN quality and the increased band bending due to the polarization field. In spite of this, we have demonstrated 9 nm InGaN based single DH LEDs exhibiting peak EQE approximately 25% higher than that of a MQW-LED [6 period $In_{0.15}Ga_{0.85}N$ (2nm)/$In_{0.06}Ga_{0.94}N$(3nm)] with low efficiency degradation (~10%) up to current densities of 600 A/cm$^2$. As expected, at low injection levels, *i.e.*, below 60 A/cm$^2$, the 9 nm DH-LEDs exhibit relatively slower EQE rate of increase with injection current compared to that of the MQW-LED. This observation is consistent with the IQE measurements we performed, and is caused by the larger spatial separation of electrons and holes owing to the stronger effect of the polarization field in thicker active regions. Essentially this is equivalent to a radiative recombination coefficient which increases with injection current before other ailments set in.

Very few studies have been carried out on the quantum efficiency of InGaN based DH structures.[47] We demonstrated that with increasing DH active layer thickness from 3 nm to 6 nm the relative EQE increased considerably despite reduction in IQE and the rate of increase of efficiencies with increasing injection. The relative EQE was enhanced substantially in dual 3 nm DH and dual 6 nm DH LEDs, separated by a 3 nm-thick $In_{0.06}Ga_{0.94}N$ barrier. Incorporating more DH active regions of the same thickness, separated by thin and low InGaN barriers, results in enhanced emission intensity without any discernible degradation of the active region quality unlike that observed in thicker single DH layers due to strain relaxation with increasing InGaN thickness. We find that employment of low and thin InGaN barriers is essential for ameliorating carrier (particularly hole) transport across the active region. Numerical simulations elucidated carrier injection effects on the overlap of the electron and hole spatial distributions.

### 4.1.2 Experimental procedures

The active regions of *c*-plane InGaN LED structures contained either one or more (dual, quad, hex) $In_{0.15}Ga_{0.85}N$ DH active regions separated by 3 nm $In_{0.06}Ga_{0.94}N$ barriers. **Figure 4.1** shows the conduction band diagram for dual DH structures where flat bands are shown for simplicity. All the structures incorporate a SEI layer for efficient thermalization of hot carriers prior to injection into the active region.

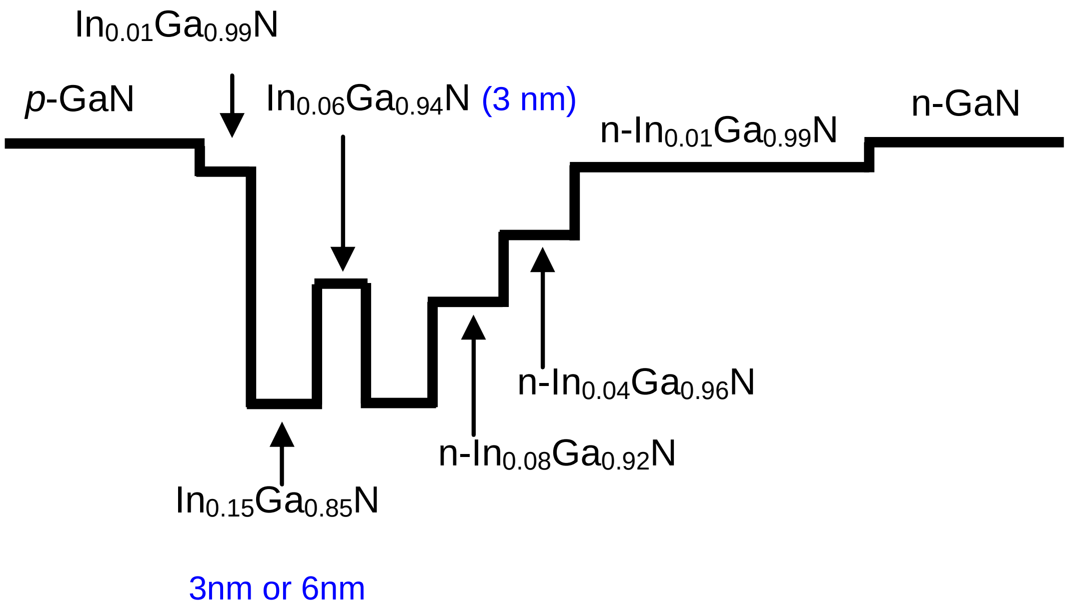

**Figure 4.1**: Conduction band diagram for dual DH LED structures.

### 4.1.3 B coefficient calculations

IQE and EQE values for all LED structures were measured at different injection levels and the effects of the active region design and the resulting polarization fields and band structures were investigated. For determination of the IQE from optical measurements injection dependent radiative recombination coefficients obtained from numerical simulations of the band structures and electron and hole distributions were used.

In the realm of Fermi's Golden Rule, the spontaneous transition rate from a group of initial states *i* in the conduction band to a group of final states *f* in the valence band separated by a transition energy $\hbar\omega$ can be expressed as

$$T_{i\to f} = \frac{2\pi}{\hbar}\left|H_{fi}\right|^{2}\rho_{r}\left(\hbar\omega\right)F\left(\hbar\omega\right)$$ **Equation 4-1**

where $\rho_r(\hbar\omega)$ is the reduced density of states, $\hbar\omega$ is the transition energy,

$F = f_c(1 - f_v)$ is the Fermi factor given in terms of the Fermi functions for the conduction ($f_c$) and valence bands ($f_v$), and $H_{fi}$ is the transition matrix element given by,

$$H_{fi} = \langle \Psi_f | H | \Psi_i \rangle = \int \Psi_f^*(\mathbf{r}) H(\mathbf{r}) \Psi_i(\mathbf{r}) d^3\mathbf{r}$$ **Equation 4-2**

For a system with confinement along the *z*-direction (growth direction), the wavefunctions can be expressed using the envelope functions as $\Psi(\mathbf{r}) = \psi(z)\phi(\mathbf{r}_{xy})$. If the physical interaction operator is independent of the variable *z*, the matrix element can be simplified to[48]

$$H_{fi} = \left(\frac{eA_0}{2m_0}\right) M \int \psi_f^*(z)\psi_i(z)\,dz$$ **Equation 4-3**

where $A_0$ is magnitude of the sinusoidal local vector potential, *e* is the electron charge, $m_0$ is the free electron mass, and *M* is the in-plane momentum matrix element. The spontaneous transition rate in **Equation 4-3** can then be written as

$$T_{i\to f} = \frac{2\pi}{\hbar}\left(\frac{eA_0}{2m_0}\right)^2 |M|^2 \left|\int \psi_f^*(z)\psi_i(z)\,dz\right|^2 \rho_r(\hbar\omega) F(\hbar\omega)$$ **Equation 4-4**

**Equation 4-4** indicates that a necessary condition for efficient recombination is the spatial overlap between the electron and hole wavefunctions ($\psi_e$ and $\psi_h$) and the radiative recombination rate is proportional to the squared overlap integral when electrons and holes are confined in the *z*-direction.

For quantum-confined structures it has been suggested that low-dimensional equivalents of the bimolecular radiative recombination *B* coefficient should be introduced to eliminate the artificial dependence of the radiative recombination current on size, such as the active region width in two-dimensional (2D) systems.[48] For InGaN quantum wells with confinement along the *z*-direction, defining the spontaneous transition rate as

$T_{spont} = B_{2D} n_{2D} p_{2D}$ , where $n_{2D}$ and $p_{2D}$ are the 2D electron and hole densities, respectively, the 2D *B* coefficient can be expressed in terms of the momentum matrix element in **Equation 4-4**:[48]

$$B_{2D} = \frac{4\pi n\hbar^2}{\varepsilon_0 c^3 k_B T} \frac{(\hbar\omega)}{m_e^* m_h^*} \left(\frac{e}{2m_0}\right)^2 \times |M|^2 \left|\int_0^\infty \psi_h^*(z)\psi_e(z)\,dz\right|^2 \rho_r(\hbar\omega), \qquad \textbf{Equation 4-5}$$

where *n* is the refractive index, $\varepsilon_0$ is the permittivity of free space, *c* is the speed of light, $\hbar\omega$ is photon energy, $k_B T$ is the thermal energy, and $m_e^*$ and $m_h^*$ are the electron and hole effective masses (obtained using linear interpolation from the binary values for a given In content), respectively. The momentum matrix element *M* can be obtained from the in-plane interband transition matrix element (for polarization within the plane), $P_{cv} = 2|M|$ ,[49] which has been determined from the absorption measurements for binaries InN and GaN.[50] Using a value of $P_{cv} = 9.6\times10^{-20}$ g cm/s obtained from linear interpolation for the required composition, the $B_{2D}$ coefficient was calculated to be $1.8\times10^{-4}$ cm$^2$s$^{-1}$ for an $In_{0.15}Ga_{0.85}N$ active region assuming full overlap of electron and hole wavefunctions. In order to make the transition from the 2D to the 3D case to be able to employ the conventional 3D rate equation, the 2D *B* coefficient should be multiplied by the active region thickness, $L_z$ . To test this approach and the validity of the 2D approximation, the 3D limit for the *B* coefficient for $In_{0.15}Ga_{0.85}N$ was also calculated from[51]

$$B_{3D} = \frac{e^2 n}{m_0^2 c^3 \hbar^2} \left(\frac{2\pi\hbar^2}{k_B T}\right)^{3/2} \times M^2 \times \frac{1}{(\bar{m}_x \bar{m}_y \bar{m}_z)^{1/2}} \hbar\omega, \qquad \textbf{Equation 4-6}$$

where $\bar{m}_{x,y,z} = m_{e(x,y,z)} + m_{h(x,y,z)}$ . The 3D *B* coefficient calculated using **Equation 4-6** is $5\times10^{-11}$ cm$^3$s$^{-1}$ for $In_{0.15}Ga_{0.85}N$. This value is smaller than that obtained using $B_{2D}L_z$

even for the thinnest active region investigated in this study with $L_z$ = 3 nm. Therefore, we assume that all the LED structures employed here exhibit 3D behavior but with an electric field along the growth direction reducing the spatial overlap of charge carriers in the active region. Consequently, the injection dependent overlap integral of the electron and hole wavefunctions should be incorporated into the calculation of the 3D *B* coefficients using the upper limit for full overlap, $5\times10^{-11}$ $\mathrm{cm^3/s}$:

$$B=\left(5\times10^{-11}\right)\ \left[\mathrm{cm^3s^{-1}}\right]\times\left|\int_0^\infty \psi_h^*(z)\psi_e(z)\,dz\right|^2 \qquad \textbf{Equation 4-7}$$

In this study, the effects of the active region design and the resulting polarization-induced field[52] on the overlap integral and the associated spontaneous recombination rates were investigated at different injection levels. **Figure 4.2** (a) presents the simulated bimolecular recombination coefficients, *B*, which are obtained from the transition matrix element and thus the simulated squared overlap integrals of the electron and hole wavefunctions within the DH active regions. It should be mentioned that the calculated *B* coefficients may vary slightly based on the material parameters used for a given structure; however, this would not affect the overall conclusions of this paper. The calculated *B* coefficients are also plotted in **Figure 4.2** (b) as a function of supplied electrical power per unit cross-sectional area, which is the product of injection current density and applied voltage used in the simulations. It is apparent from **Figure 4.2** (a) that the *B* coefficient, instead of being constant as assumed in Ref. 23, depends on the injection current density for a given design,[53] increasing with injection due to screening of the internal fields by free carriers. Naturally, the *B* coefficient tends to saturate at high injection levels as the nearly flat band condition is approached.[52] It is also evident that thinner active layers have relatively larger spatial overlap of the electron and hole wavefunctions. The single 3 nm DH LED shows 30% higher squared overlap integral value compared to the single 6 nm DH LED at a current density of ~300 A/cm$^2$. The lower *B* coefficients in wider active regions are attributed to the increased spatial separation of electrons and holes by the larger contribution of the polarization fields. Moreover, while the dual and the single DH structures exhibit comparable overlap integrals at low injection levels (below 100 A/cm$^2$), the dual DH structures surpass their single DH counterparts as the injection current increases. For example, the dual 3 nm DH LEDs show 15% higher EQEs compared to the single 3 nm DH LEDs at a current density of 500 A/cm$^2$. Furthermore, the rate of increase for the *B* coefficient *vs.* the current density at low injection levels is reduced with increasing active layer thickness, which is consistent with the experimental IQE and EQE data shown in **Figure 4.2** (c) and **Figure 4.3**, respectively.

### 4.1.4 Results and discussions

The room temperature IQE values were measured by resonant optical excitation intensity-dependent photoluminescence (PL) but with invoking injection dependent *B* coefficients to produce more accurate IQE values *vs.* the photoinduced carrier concentration. The generation rates in optical excitation were matched to those calculated from the electrical injection power density used in the simulations to account for the carrier density (injection) dependence of the *B* coefficients. The excitation wavelength from a frequency doubled Ti:Sapphire laser was set to 385 nm for photogeneration of carriers inside the active region only. **Figure 4.2**(c) shows the resulting IQE values *vs* .the carrier concentration for all the DH structures. The IQE for single 3 nm DH LED reaches above 95% at a carrier concentration of 10$^{18}$ cm$^{-3}$, which corresponds to a photocurrent density of 1 A/cm$^2$ as indicated in **Figure 4.2**(d). The photocurrent densities in **Figure 4.2**(d) are obtained from carrier densities using the rate equation as described earlier. As can be seen, when we insert a second DH active region separated by a 3 nm-thick $In_{0.06}Ga_{0.94}N$ barrier, which still allows efficient hole transport, the IQE rate of increase with photocurrent density is slower, and a 90 % IQE is reached at a photocurrent density of ~5 A/cm$^2$ compared to 0.3 A/cm$^2$ in the single 3 nm DH. However, the IQE values are very similar for both structures at high injection levels. Increasing the DH thickness to 6 nm and 9 nm reduces IQE and its rate of increase substantially. As shown in **Figure 4.2**(c), IQEs for both 6 nm and 9 nm DH LEDs increase relatively slowly with carrier concentration and reach 70% at around a carrier density of $4\times10^{18}$ cm$^{-3}$. The dual 6 nm DH essentially has quite a similar IQE dependence on carrier concentration as the single 6 nm DH, as shown in **Figure 4.2**(c). Whereas the dependence on photocurrent density shows an apparent discrepancy due to increased overall active region thickness (12 nm) and larger *B* coefficients used in the conversion calculation from density of photocarriers to photocurrent density. With increasing DH thickness, the IQE values degrade and the IQE rate of increase with the carrier concentration becomes slower, the most severely for DH thickness of 11 nm. These effects in wider active regions can be partially attributed to the stronger polarization field effects and decreased electron and hole wavefunction overlap and partially to the degraded layer quality with increasing InGaN thickness, which will increase nonradiative recombination.

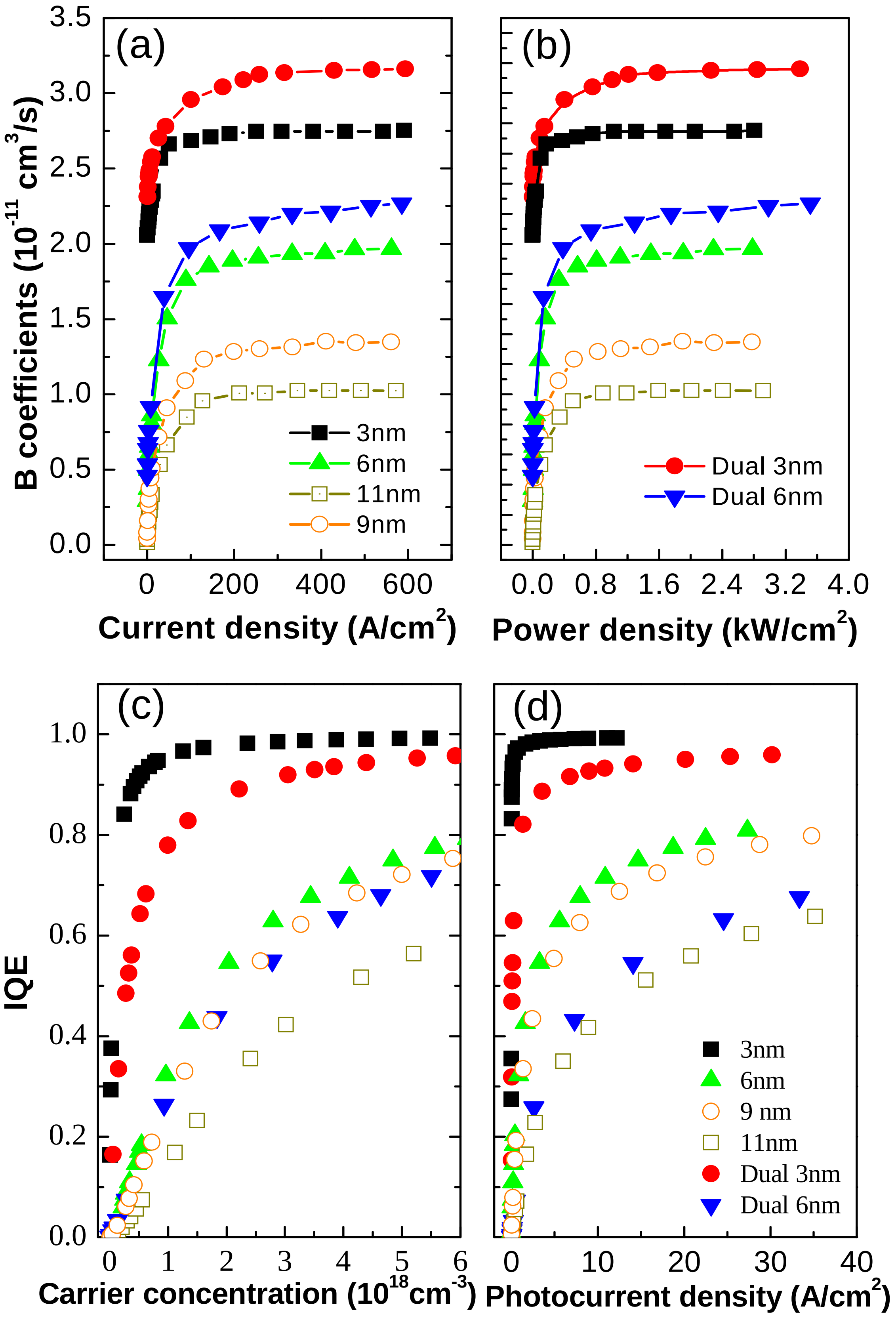
(a)
(b)
(c)
(d)
B coefficients ($10^{-11}$ cm$^3$/s)
3.5
3.0
2.5
2.0
1.5
1.0
0.5
0.0
0
200
400
600
Current density (A/cm$^2$)
3nm
6nm
11nm
9nm
0.0
0.8
1.6
2.4
3.2
4.0
Power density (kW/cm$^2$)
Dual 3nm
Dual 6nm
IQE
1.0
0.8
0.6
0.4
0.2
0.0
0
1
2
3
4
5
6
Carrier concentration ($10^{18}$cm$^{-3}$)
0
10
20
30
40
Photocurrent density (A/cm$^2$)
3nm
6nm
9 nm
11nm
Dual 3nm
Dual 6nm

**Figure 4.2:**Calculated *B* coefficients using squared overlap integrals of electron and hole wavefunctions (proportional to radiative recombination rate) within the active region as a function of (a) current density calculated using SILVACO ATLAS simulations and (b) injection electrical power density (the product of applied voltages and current densities). (c) IQE values determined from excitation-dependent PL for LEDs with various DH thickness by using injection dependent *B* coefficients from (a). (d) IQE values *vs.* photocurrent density converted from carrier concentration using Equation 8.

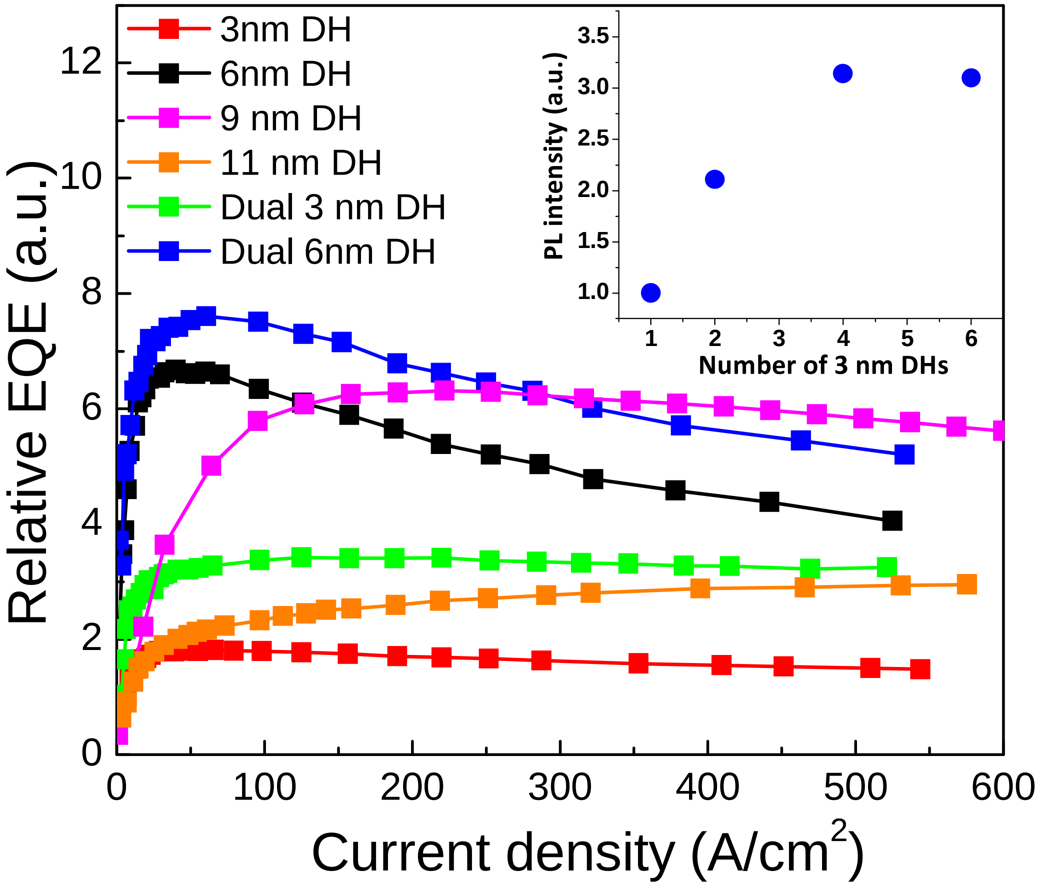

**Figure 4.3**: Relative external quantum efficiencies of DH LEDs as a function of pulsed injection current density (0.1 % duty cycle and 1 kHz frequency). The inset shows the normalized resonant PL intensity versus the number of 3 nm DH active regions.

The relative EQE values for the LED structures with various DH thicknesses are shown in **Figure 4.3**. As presented in **Figure 4.3** (c) and (d), the 3 nm DH exhibits the highest IQE, reaching 97.5% at a low carrier level ~$10^{18}$ $cm^{-3}$ (corresponding to 1 A/$cm^2$). Its EQE also increases at a fast rate with current injection and reaches its maximum at ~ 30 A/$cm^2$ owing to the greater spatial overlap of electron and hole wavefunctions. However, the overall EQE is only 23% of that of the single 6 nm DH LED, likely due to lower density of states within the 3-nm InGaN active layer (nearly two-dimensional states) as compared to 6-nm InGaN layer (nearly three-dimensional states) as well as more severe electron overflow in thinner active region. Noticeably, when another 3 nm $In_{0.20}Ga_{0.80}N$ layer separated by a 3nm $In_{0.06}Ga_{0.94}N$barrier is added to the active region, the EQE value is doubled due to increased active layer volume, which is consistent with resonant PL measurements showing a two fold increase in emission intensity for the same excitation power (see the inset of **Figure 4.3**).

The single 6 nm DH LED structure shows the maximum relative EQE values at current density ~41 A/$cm^2$, slightly higher than that for the 3 nm DH LEDs, indicative of a slower rate of increase with injection for the 6 nm DH LED. However, it suffers from large efficiency droop (reduced by 38% at 550 A/$cm^2$ with respect to the maxima) with increasing current density. The dual 6 nm DH LED shows ~12% higher peak EQE values and less efficiency droop percentile (reduced by ~30%) under the same current density. Increasing the individual layer thickness further to 9 and 11 nm results in deteriorated layer quality and the 11 nm single DH LED exhibits much lower EQE values. We should also note that the dual 6 nm DH shows 20% higher peak EQE than that obtained from the single 9 nm DH and much faster increasing rate of EQE with current injection. It is also observed that the 9 nm DH LED exhibits lower EQE values at lower injection levels (less than 125 A/cm$^2$) due to a much slower rise of EQE with injection although its EQE saturates at higher values with increasing injection level. At high current densities, *e.g.* 550 A/cm$^2$, the 9 nm single DH shows 15% and 32% higher EQE than those for dual 6 nm and single 6 nm DH LEDs, respectively, due to greater efficiency reduction in single and dual 6 nm DHs. Specifics of the degradation mechanisms and methods to mitigate them are still under investigation.

Promisingly, the EQEs for the single 3 nm and dual 3 nm DH LEDs show negligible degradation with increasing injection current density up to 600 A/cm$^2$. According to the IQE and relative EQE data for single 3 nm and dual 3 nm DH LEDs, there seems to be a trade-off to achieve both high IQE and EQE in *c*-plane InGaN DH LEDs. However, the negligible droop and rapid initial increase of quantum efficiencies with injection current in single 3 nm and dual 3 nm DH LEDs are critical to InGaN LED improvement. In an effort to enhance the relative EQE of such DH structures further we have grown LED structures with more (4 and 6) 3 nm-thick active regions separated by the thin $In_{0.06}Ga_{0.94}N$ barriers. Resonant PL measurements revealed that the PL intensity of quad 3 nm DH LED is nearly four times higher than that for single 3 nm DH; however, the PL intensity of the hex 3 nm DH LED did not scale to 6 times that from the single 3 nm DH but is very close to that from the quad 3 nm DH LED, which is shown in the inset of **Figure 4.3**.This behavior can be attributed to the relaxation of the active regions upon increasing the number of 3-nm DH layers beyond four. More detailed data will be discussed and provided in the following section.

### 4.1.5 Conclusion

In conclusion, bearing efficiency loss/retention arguments at high current levels in mind, we investigated the quantum efficiencies of DH LED structures with different active region designs. DH LEDs with 3 nm-thick active regions reached very high IQE (97 %) at $10^{18}$ $cm^{-3}$ carrier density and exhibited negligible efficiency droop with increasing injection. Increasing DH thickness from 3 nm to 6 nm resulted in a decrease in IQE; however, the peak EQE increased although the rate of increase in EQE with injection slowed down slightly. Further increase of the DH active region thickness to 9 nm improved EQE only at very high injection levels while 11 nm thick DH showed significantly lower EQE due to relaxation and the degradation of the InGaN material. To increase EQE while maintaining high IQE, multiple 3 nm-thick DH active regions separated by 3 nm-thick $In_{0.06}Ga_{0.94}N$ barriers were employed. The dual 3 nm and 6 nm DH structures were found to be superior to the single DH structures considering both IQE and EQE results comprehensively. In dual 3 nm DH LEDs, the IQE reached above 95% and the EQE doubled compared to the single 3 nm DH LED. Both single and dual 3 nm DH LEDs exhibited negligible droop up to current densities above 500 $A/cm^2$. Furthermore, LEDs incorporating quad 3 nm DH active regions were observed to improve the emission further with slight reduction when six DH active regions were employed (hex 3 nm DH). Similarly, by incorporating two 6 nm DH active regions separated by a 3 nm $In_{0.06}Ga_{0.94}N$ barrier into a single LED, the highest peak EQE values were achieved: 12% and 19% higher than those provided by 6 nm DH and 9 nm DH, respectively. Moreover, both the single and the dual 6 nm DH LEDs showed similar IQE values implying that the layer quality does not degrade with the inclusion of a second 6 nm DH active region, unlike the significant degradation observed when a single 11 nm-thick DH was used.

## 4.2 Multi-thin DH (MDH) active regions

### 4.2.1 Motivation

As InGaN based light-emitting diode (LED) technology continues to develop and mature, high brightness LEDs retaining high quantum efficiencies at high injection levels (>100 A/cm$^2$) have become even more desirable to replace the prevailing incandescent lamps and fluorescent tubes in general lighting. However, the quantum efficiency of typical InGaN multi quantum well (MQW) LEDs peaks at current densities even as low as ~ 10 A/cm$^2$, and drops with increasing injection by a factor of as much as 2 in some reported cases. Although debates still persist on the origins of “efficiency droop”, carrier overflow has been reported to be the substantial component.[54,55] In order to avoid carrier overflow and increase the light output, LEDs must employ thick double heterostructure (DH) or MQW active regions.

In InGaN MQWs normally adopting thick (>10 nm) GaN barriers light is emitted mainly from the topmost QWs adjacent to *p*-GaN due to the poor hole transport.[56,57] DH active regions on the other hand can ensure more uniform hole spreading across the active region due to the absence of barriers and consequently have paved the way for negligible drop in quantum efficiencies beyond current densities of ~150 A/cm$^2$.[58] Moreover, DH LEDs possess bulk-like 3D density of states (DOS), and therefore, can accommodate more carriers than thin QWs having constant 2D DOS. However, among the ramifications of DHs are the degradation of InGaN structural quality with increasing thickness and separation of electron and hole wavefunctions due to the polarization field in the c-plane variety.[59,60] Therefore, keeping the DH layer thin (3 nm) but stacking multiple of them separated by thin and low barriers (for ameliorating hole transport) in the active regions could be a promising approach to maintain high material quality and overcome the efficiency loss at high driving currents. In this work, we demonstrate that by using 3nm-thick multi-DH active layers separated by 3 nm-thick low-energy $In_{0.06}Ga_{0.94}N$ barriers the electroluminescence (EL) is enhanced dramatically, in proportion with the number of DH layers up to 4 without discernible efficiency loss at high injection levels. Moreover, under resonant optical excitation, emission intensities at 10 K increase linearly with excitation power, indicating nearly unity quantum efficiency, and scale with the effective active region thickness for a given excitation density. This study markedly differs from the prior work[60] in that with increasing number of active region DH layers carrier overflow is unequivocally shown to reduce significantly and material degradation beyond 6 DH layers is found to be the efficiency limiting factor for a given electron injector design. We also show that using multi-DH active regions is a more effective way to achieve high LED efficiency compared with solely increasing single DH thickness or using a MQW active region.

### 4.2.2 Experimental procedures

The *c*-plane multi-DH InGaN LED structures, emitting at ~425 nm, were grown on ~5 µm-thick *n*-type GaN templates on sapphire substrates in a vertical low-pressure metalorganic chemical vapor deposition (MOCVD) system. The GaN templates employed an *in situ* $SiN_x$ nanonetwork to reduce the dislocation density down to mid-$10^8$ $cm^{-3}$.[61] The active regions contained one to eight 3 nm-thick $In_{0.15}Ga_{0.85}N$ DH active layers separated by 3 nm $In_{0.06}Ga_{0.94}N$ barriers. All the structures incorporate a staircase electron injector (SEI) for efficient thermalization of hot electrons prior to injection into the active region and a 60-nm Si-doped ($2\times10^{18}$ $cm^{-3}$) $In_{0.01}Ga_{0.99}N$ underlying layer for improving the quality of overgrown layers. The SEI consists of two 5 nm InGaN layers with step-increased In compositions of 4% and 8%, inserted in the given order below the active region. The LED structures were completed with 100 nm-thick Mg-doped *p*-GaN layers having $6\times10^{17}$ $cm^{-3}$ hole density, as determined by Hall measurements on a separate calibration sample. The simulated band structures for a typical hexa 3 nm DH were shown in **Figure 4.4**. Device fabrication procedures using standard photolithography are described elsewhere.[60] The EL efficiencies were compared with those of LED structures with either 9 nm thick $In_{0.15}Ga_{0.85}N$ DH or six period MQW [$In_{0.15}Ga_{0.85}N$(2 nm)/$In_{0.06}Ga_{0.94}N$ (3 nm)] active regions.

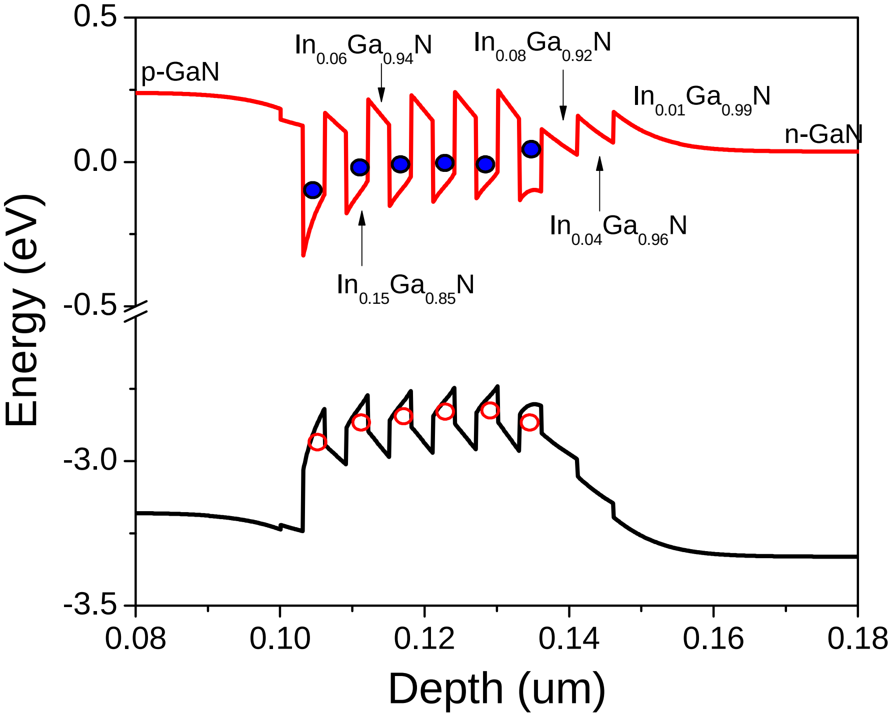

**Figure 4.4** Simulated band structures with 6 period $In_{0.15}Ga_{0.85}N$ (3 nm)/$In_{0.06}Ga_{0.94}N$ (3

nm), solid blue-filled circles represents electrons in the conduction band while empty red circles represents holes in the valence band.

### 4.2.3 STEM images

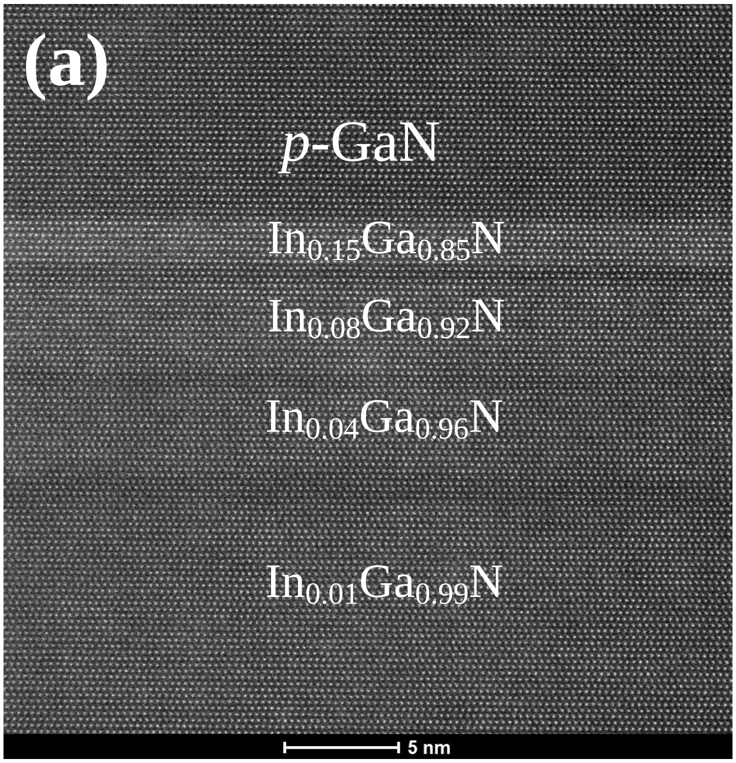

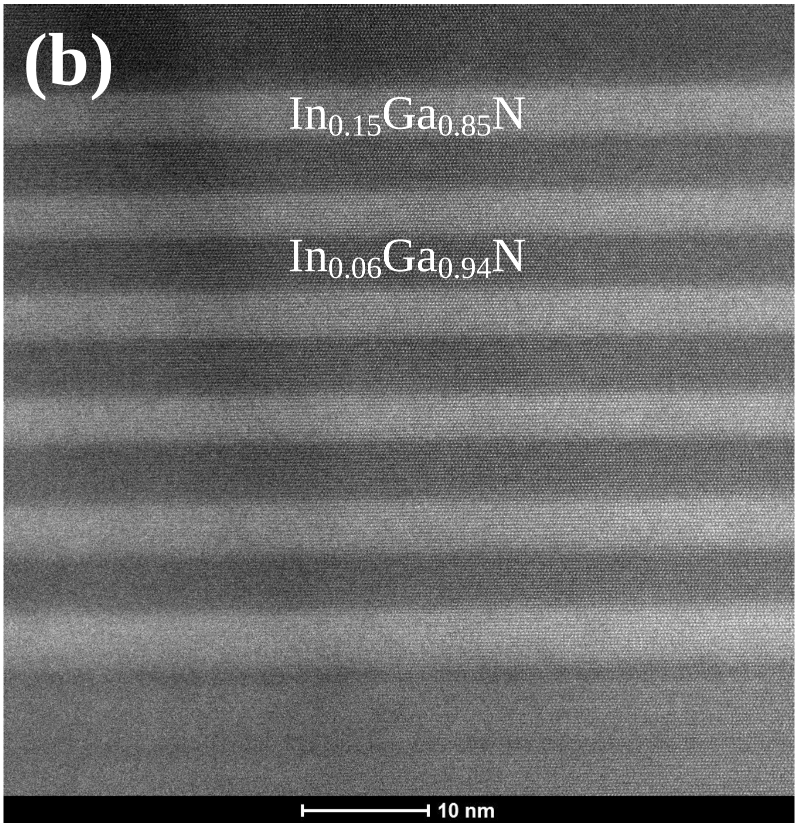

**Figure 4.5** Scanning transmission electron microscope (STEM) images of (a) single 3 nm DH LED structure; (b) active region of 6 period 3 nm DH structures

Aberration corrected-STEM images shown in **Figure 4.5** were obtained from University of Wisconsin.[62] Atomic resolution STEM utilizes a focused electron probe smaller than the diameter of an atom with a current large enough to produce meaningful signal at high angles in the diffraction plane. The STEM images were produced by scanning the probe across a thin sample, causing scattering of electrons to all angles. Electrons that are collected by a high angle annular detector produce a signal that depends strongly on the atomic number (Z) of the atoms under the beam and give this technique its names, high angle annular dark field (HAADF), and Z-contrast imaging. In the simplest model, the intensity is proportional to Z albeit in real case it is modified by dynamic diffraction and strain. If electrons are collected at smaller angles, diffraction contrast enters the image and sample strain is emphasized. Annular bright field (ABF) STEM is a recently discovered imaging technique, where only electrons in the outer annular region of the bright field zone are collected. ABF STEM allows the detection of light elements like in bright field STEM, but preserves the interpretability over thickness and defocus like Z-contrast STEM imaging. They used high angle Z-contrast, smaller angle diffraction contrast, and ABF STEM in the experiments. The spherical aberration corrector allows for partial correction of unavoidable lens aberrations, which on their STEM can produce $\leq$ 0.8 Å resolution Z-contrast images. Some studies claimed lateral In composition fluctuations in the InGaN active layers that may act like quantum dots and localized carriers especially in thicker active layers such as MQWs, which therefore could enhance the quantum efficiency of InGaN layer. However, as shown in **Figure 4.5** , our samples (single 3 nm DHs and Hexa 3nm DHs) show abrupt barrier and well interface and laterally uniform In distribution and no In-rich clusters were observed.

### 4.2.4 Results and discussions

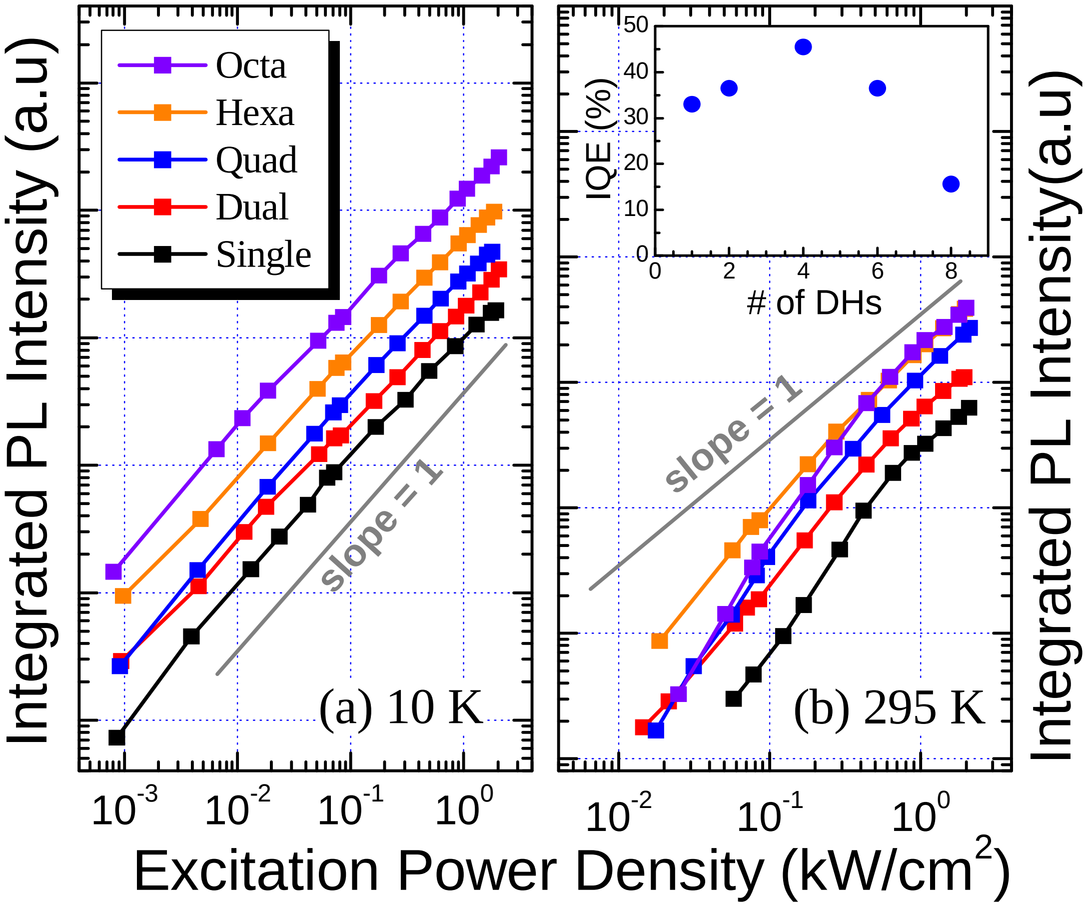

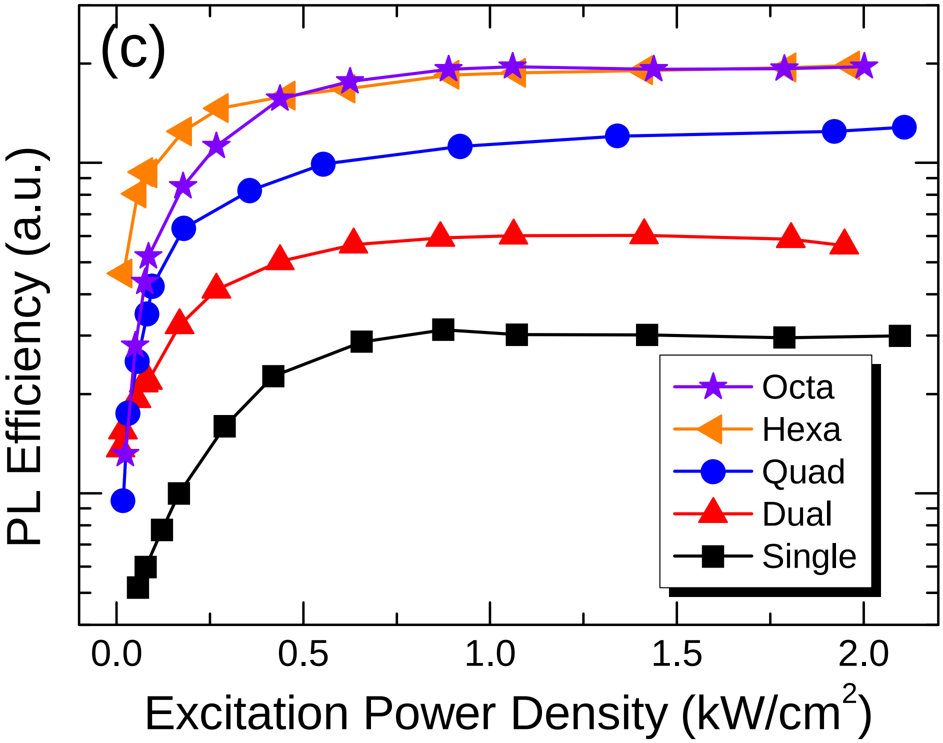

**Figure 4.6** Integrated PL intensity as a function of excitation power density at (a) 10 K and (b) 295 K; gray solid lines indicate slope of 1 and the inset of (b) displays the PL-IQE *vs.* the number of 3 nm DHs in the active region; (c) PL efficiencies of multi-3 nm DHs *vs.* excitation power density at room temperature.

As discussed in Chapter 3, the IQE values were obtained by power dependent PL measurement methods using a data fitting technique incorporated with rate equation. However, data fitting procedures might introduce various errors, which sometimes results in inconsistence of IQE values. Therefore, considerable cares must be taken to avoid such issues. On the other hand, a common and more straightforward procedure to evaluate the IQE involves excitation-dependent photoluminescence (PL) measurements and comparison of the PL intensities at low and room temperatures by assuming 100% IQE at low temperature though it might not be the case.[63,64] Excitation power dependent resonant

PL measurements were performed at both 10 K and 295 K using 385 nm excitation from a frequency doubled Ti:Sapphire laser ensuring photo-generation of carriers only in the LED active regions. The highest excitation density used corresponds to an average carrier concentration of ~$10^{18}$ $cm^{-3}$ in the single DH LED structure. As the collected PL intensity is proportional to excitation intensity, $L_{PL} \propto I_{exc}^{m}$, the linear dependence ($m \approx 1$) for all structures at 10 K [see **Figure 4.6** (a)] indicate that the radiative recombination dominates, *i.e.* $\tau_{Rad} << \tau_{nonRad}$, where $\tau_{Rad}$ and $\tau_{nonRad}$ are the radiative and nonradiative lifetimes, respectively. It is therefore reasonable to assume that the quantum efficiencies are nearly one at 10 K for all DH LEDs, omitting the negligibly slight deviations. The room temperature data [**Figure 4.6** (b)], however, shows superlinear dependence ($m \approx 1.4$ - 1.95) for low excitations, which is attributed to the notable impact of nonradiative recombination ($m = 2$ in case of constant $\tau_{nonRad}$). As the excitation density is increased, the slope gradually approaches to $m = 1$ ($I_{PL} \propto I_{exc}$). The gradually decreasing slope in the intermediate excitation regime indicates strong competition between nonradiative and radiative processes and can be attributed to decreasing radiative lifetime, beneficial, for moderate injections. Another process to be kept in mind is that with further increase of excitation, saturation of localized states and delocalization of carriers (particularly holes, as the electron density in the wells is in mid-$10^{17}$ $cm^{-3}$) may allow access to additional nonradiative centers and result in enhanced recombination rate with respect to low excitation.[65, 66] Moreover, Coulomb screening of the quantum confined Stark effect (QCSE) with increasing excitation leads to an increased interband recombination rate $1/\tau_{Rad}(N) \propto BN$, where $B$ is the bimolecular recombination coefficient and $N$ is injected carrier density. The IQE values deduced from ratio of PL intensities at 300 K and 10 K at the highest excitation density employed are shown in the inset of **Figure 4.6** (b). The quad 3 nm DH LED exhibits an IQE, so determined, of ~46% whereas increasing the number of 3 nm DH active regions to 6 and 8 lowers the IQE to 36% and 16% respectively, indicative of active region degradation with increasing overall thickness due to plausibly strain relaxation and increased interface roughness. This degradation is evident also from the room temperature PL efficiencies, defined as the collected integrated PL intensity normalized to the incident laser power, shown in **Figure 4.6** (c). Notably, the PL efficiencies nearly scale with the number of DH layers up to 6 due to increased absorption and emitting volume, showing ~ 2, 4 and 6.5 fold increase for dual, quad and hexa DHs compared to single DH at an excitation density of 1.5 kW/cm$^2$, but no further improvement for the octa DH LED which is most likely a manifestation of material degradation.

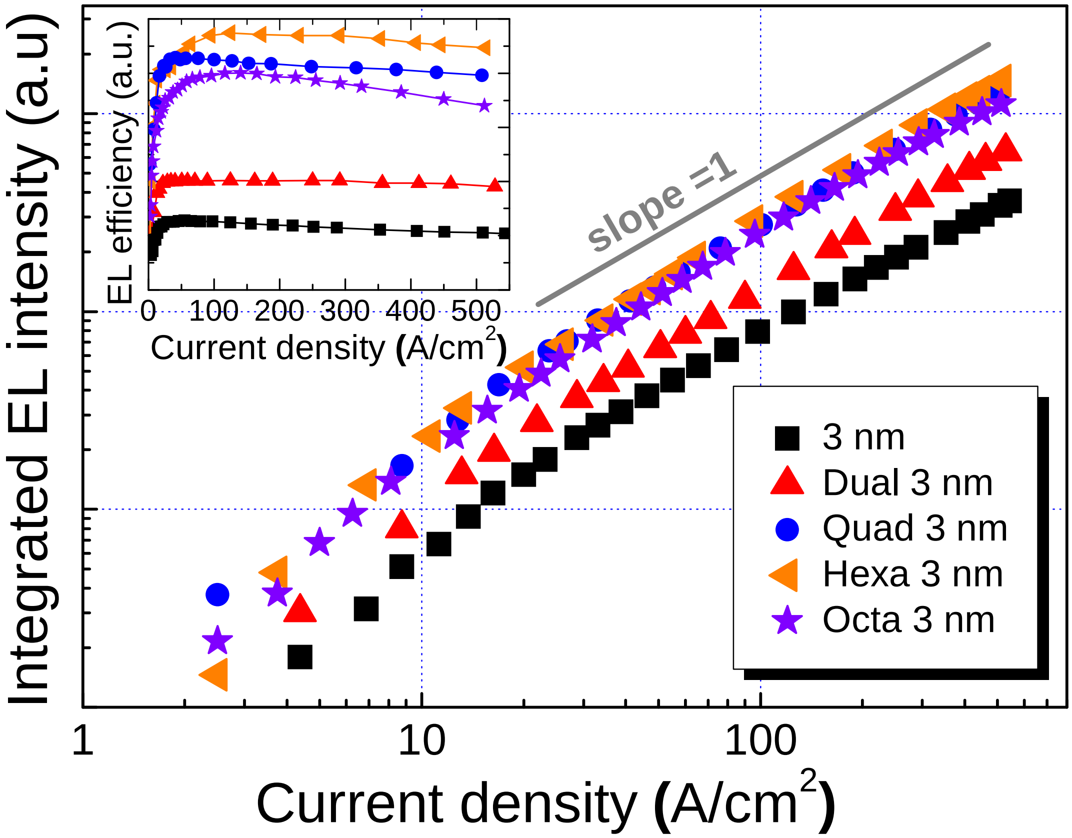

**Figure 4.7** The integrated EL intensity dependence on current density (the grey-sold line indicates slope of 1); the inset shows EL efficiencies of multi-3 nm DHs *vs.* injected carrier density.

To study the impact of carrier overflow and other carrier transport features, we measured EL efficiencies on-wafer (unpackaged) with light output collected primarily normal to the sample surface by an optical fiber. The integrated EL intensities *vs.* injection current are shown in **Figure 4.7**. The integrated EL intensity, $L_{EL}$ , can be described by a power dependence on the injection current density as $L_{EL} \propto J^m$ , where the power index *m*, as in the case of optical excitation, reflects an effective rate of recombination processes within a given range of current densities.[67] The superlinear growth of EL intensity (*m* ~ 1.4 for single, ~ 1.3 for dual and quad, and ~ 1.6 for hexa and octa DH LEDs) at low current densities is again attributed to nonradiative recombination. Smaller *m* values suggest lower density of nonradiative recombination centers in single, dual and quad DH LEDs compared to hexa and octa DH LEDs. The EL intensity changes nearly linearly at high current levels; therefore, EL efficiency tends to be constant [**Figure 4.7** inset].

As presented in the inset of **Figure 4.7**, the EL efficiency for the MDH structures with up to 4 DH layers increases rapidly with current injection and reaches its maximum at ~ 35-40 A/cm$^2$. Compared to the single 3 nm DH LED, the peak EL efficiencies for dual and quad DH LEDs are higher by 1.6 and 3.5 times, respectively. Unlike in the case of optical injection, this significant improvement on EL efficiency cannot simply be explained by increased emitting volume as for a given current density overall carrier concentration is the same. Therefore, the data unequivocally indicates that increasing the number of 3 nm DH layers (from 1 to 6) decreases the overflow of injected carriers considerably (*i.e.* more of the injected carriers are captured by the active region), while further increase in number of DH layers (8) aggravates by introducing more nonradiative recombination centers due to degradation of the active region quality.

It is important to note that although the 5nm+5nm SEI (electron cooler) design used here has been shown to be an effective replacement for the $Al_{0.15}Ga_{0.85}N$ electron blocking layer for reducing electron overflow in structures with multiple QWs and wider DHs (6 and 9 nm),[68] it must be optimized for a given active layer to fully prevent electron overflow. Based on the hot electron model reported in Ref. 68, the percentage (*p*) of electrons captured by and recombine in the active region is increased to 76% in quad DH

LED compared to 48% and 60% for single and dual 3 nm DH LEDs, respectively, at a current density of ~500 A/cm$^2$.

The above somewhat crude estimates are simply based on single active regions with effective thicknesses equal to the number of DH active layers multiplied by 3 nm, *i.e*. 3, 6 and 12 nm for single, dual, and quad 3 nm DH, respectively. Our preliminary results on LED structures with optimized SEI layers confirm that the carrier overflow can indeed be eliminated while maintaining the active region quality. For optimum SEI layer design, which depends on the overall active region design, the resulting maximum EL efficiencies for single and quad 3 nm DH LEDs are similar. Further optimization of the SEI for various active regions designs is underway.

As observed in **Figure 4.7**, the EL efficiency of hexa 3 nm DH LED is only slightly larger than that of the quad 3 nm DH, which suggests that the injected carriers are mostly consumed in the first four DH layers close to *p*-GaN due to limited hole transport for the achieved hole concentration and/or the active region quality may have slightly degraded with increased overall thickness. Further increase in the number of DH layers to 8 lowered the EL efficiency by ~20% compared to the hexa 3 nm DH at a current density of 350 A/cm$^2$, which is a clear indication of the active layer quality degradation confirmed by PL measurements conducted at 10 K and 295 K (see **Figure 4.6**).

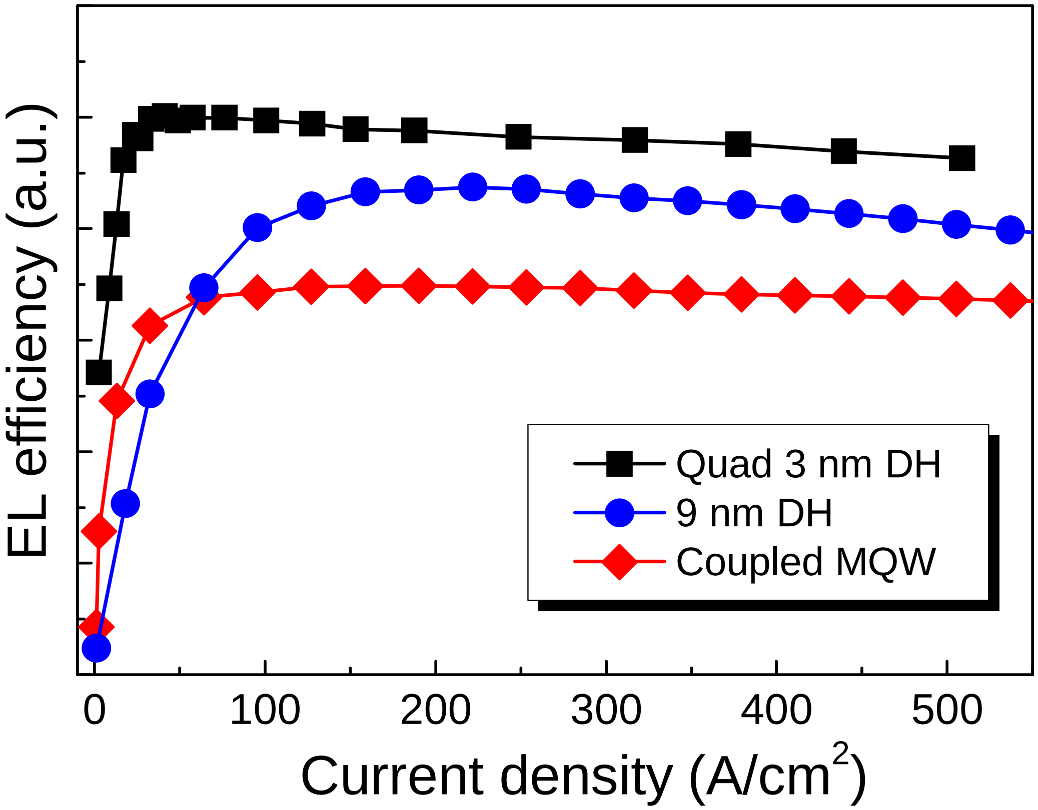

**Figure 4.8** EL efficiencies comparison for quad 3 nm DH, 9 nm DH, and coupled MQW (six period $In_{0.15}Ga_{0.85}N$ (2 nm)/$In_{0.06}Ga_{0.94}N$ (3 nm)) LEDs.

It is worth noting that the EL efficiency for all the DH LEDs except the octa 3 nm DH show negligible drop with increasing injection current density up to 500 A/cm$^2$. PL and EL data in aggregate suggest that an active region with four DH layers (quad DH LED) provides an optimum design. In addition, as shown in **Figure 4.8**, the quad 3 nm DH LED structure outperforms a typical MQW LED having the same total active layer thickness (6×2 nm well) and a DH LED with single 9 nm-thick active region, which was reported to have 1.25 and 3.8 times higher relative EL efficiency than 6 nm and 11 nm-thick single DH LEDs, respectively, at a current density of ~ 300 A/cm$^2$.[60] Therefore, it is clear that multi-3 nm DH layer design is a superior approach for increasing the active region volume for enhanced light output and improvement of LED external quantum efficiency.

### 4.2.5 Conclusion

Multi-3nm DH structures have been demonstrated to enhance the quantum efficiency of InGaN based LEDs at high injection levels. We showed that incorporating more DH layers (having 3D-like DOS) separated by thin and low InGaN barriers represents an effective avenue to improve light output compared with solely increasing single DH thickness or the number of 2 nm-thick QWs in MQW LEDs, which due to the two-dimensional DOS have limited optical output. Excitation dependent PL results indicate that PL efficiency is nearly proportional to the number of DH layers up to 6 at room temperature, suggesting the same quantum efficiency for each DH active layer. Similarly, EL efficiency is also shown to increase with the number of DH active layers up to 4, due to reduced electron leakage, and the hexa DH LED shows ~20 % higher EL efficiency than that of quad DH LED at high injection. We attribute the proportional increment in EL with increasing DH active region layers to increased carrier capture. Therefore, among the efforts to enhance the quantum efficiency at elevated injection levels, multi-DH layer designs with appropriate electron injectors can constitute a viable alternative approach to achieve high efficiency and high power LEDs.

## 4.3 Optimization of SEI structures

### 4.3.1 Motivation

As discussed in last section, the EL efficiency of quad 3 nm DHs shows about 3.5 times higher than that of single 3 nm DH. We attributed this to the more severe electron overflow in single 3 nm DH. By incorporating more 3 nm DHs, the active layer thickness is increased and thus electrons can be captured more readily in quad 3 nm DHs. First order calculation also indicated that only 48% of electrons can be efficiently injected in to the single 3 nm active region and recombine radiatively. As such, it is desirable to reduce the electron overflow by optimizing SEI structures. In the first place, we increased the two step SEI thickness without modifying the In composition inside SEIs. Secondly, we employed multi-step InGaN stair cases in order to cool down electrons sufficiently by keeping the total thickness equal to 40 nm. **Table 4-1** shows the details of studied LED structures.

**Table 4-1** LED structures under investigations

| | First SEI (nm) | Second SEI (nm) | Active region (nm) |
|---|---|---|---|
| LED-A | 5 | 5 | 3 |
| LED-B | 20 | 20 | 3 |
| LED-C | 5 | 5 | 4×3 |
| LED-D | 10 | 5 | 4×3 |
| LED-E | 20 | 20 | 4×3 |
| LED-F | 30 | 30 | 4×3 |
| LED-G | 7 step SEIs with total thickness 40 nm | | 4×3 |

### 4.3.2 Results and discussions

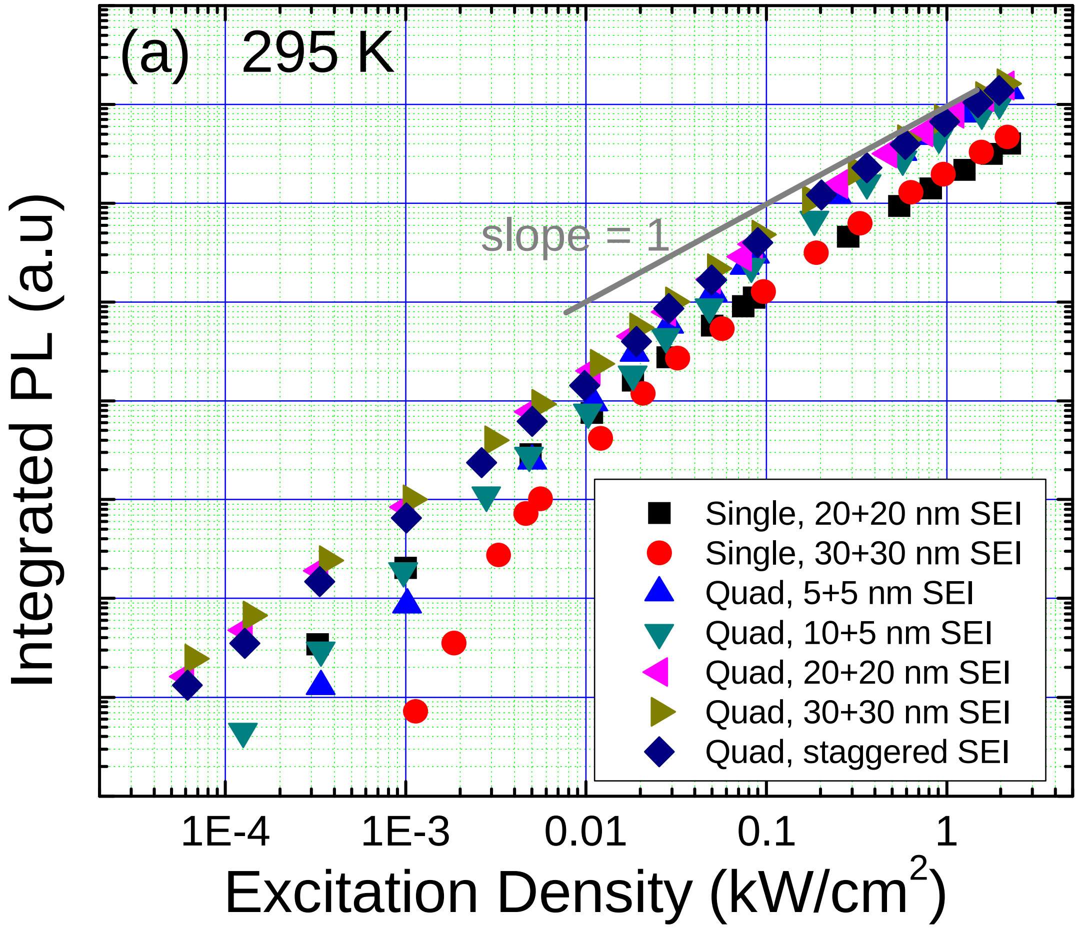
(a) 295 K
slope = 1
Single, 20+20 nm SEI
Single, 30+30 nm SEI
Quad, 5+5 nm SEI
Quad, 10+5 nm SEI
Quad, 20+20 nm SEI
Quad, 30+30 nm SEI
Quad, staggered SEI
Integrated PL (a.u)
1E-4
1E-3
0.01
0.1
1
Excitation Density (kW/cm$^2$)

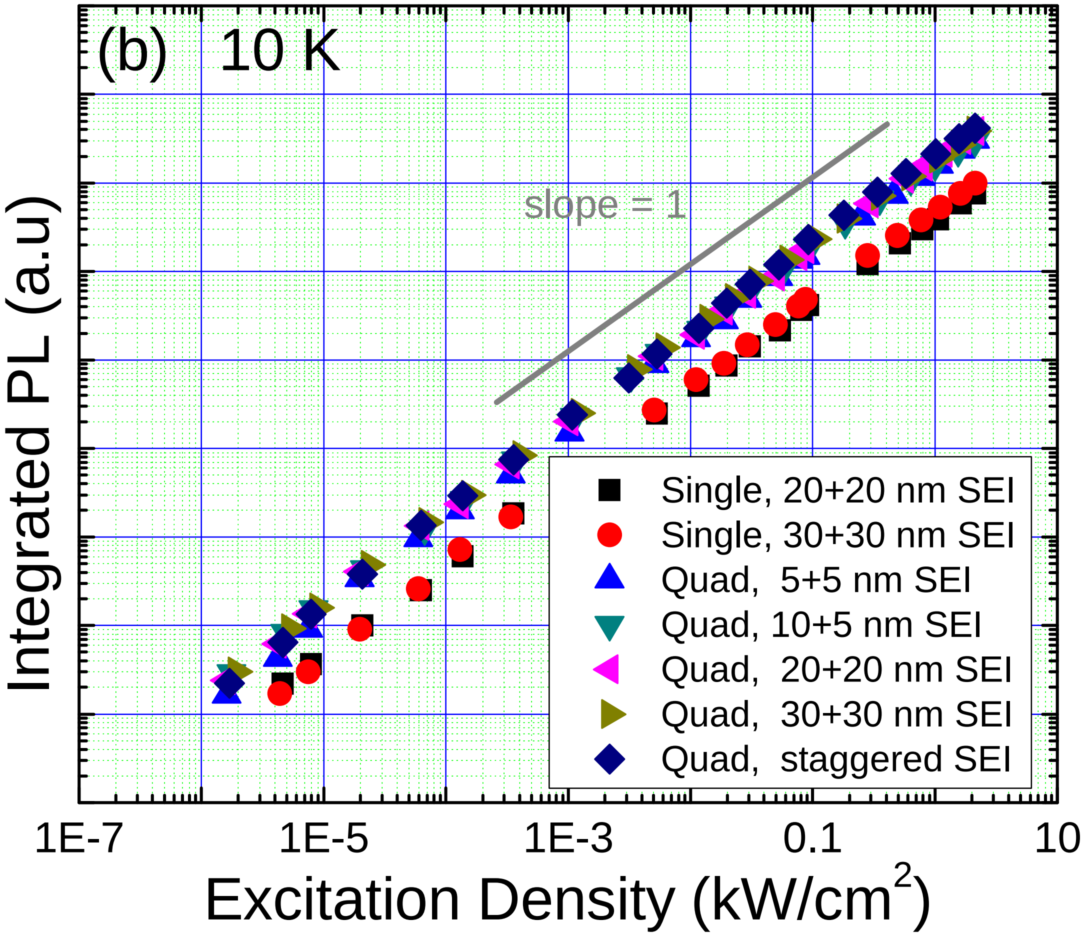
(b) 10 K
slope = 1
Integrated PL (a.u)
Excitation Density (kW/cm$^2$)
1E-7
1E-5
1E-3
0.1
10
■ Single, 20+20 nm SEI
● Single, 30+30 nm SEI
▲ Quad, 5+5 nm SEI
▼ Quad, 10+5 nm SEI
◀ Quad, 20+20 nm SEI
▶ Quad, 30+30 nm SEI
◆ Quad, staggered SEI

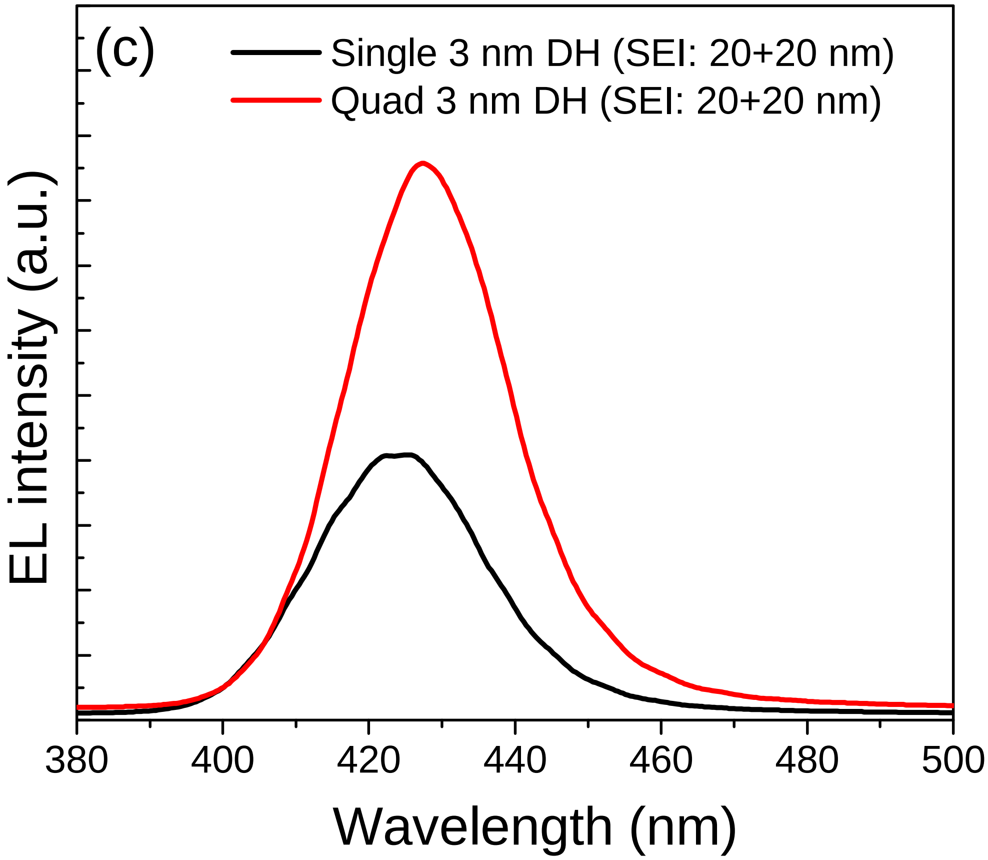

**Figure 4.9** Integrated PL intensity as a function of excitation power density at (a) 295 K and (b) 10 K; gray solid lines indicate slope of 1; (c) EL spectrum for single 3 nm and quad 3 nm DH with SEI: 20 nm+20nm under current injection 500 A/cm$^2$.

As shown in **Figure 4.9** (a) and (b), the collected PL intensity is proportional to excitation intensity, $L_{PL} \propto I_{exc}^{m}$. The linear dependence ($m \approx 1$) for all structures at 10 K indicates the radiative recombination dominates. Similar to the previous discussions, the PL intensity is scaled with the number of DH layers as quad DHs present 4 times higher PL intensity than single DH, which indicates the IQE uniformity in each DH. As expected, at room temperature, the slope of PL intensity vs. excitation is gradually changing from ~1.2-1.4 to 1, which is consistent with aforementioned data on MDH structures. We should also mention that with increasing the SEI thickness from 5 + 5 nm to 20 + 20 nm the PL intensity was improved by 15-18% for both single 3 nm DH and quad 3 nm DH structures. And consistent improvement ratio at both 10 K and 295 K can be observed. Moreover, the quad 3 nm DH with 20 nm + 20 nm SEIs shows almost the same PL intensity with quad 3 nm DH with staggered SEI having a total thickness 40 nm. **Figure 4.9** (c) shows the EL spectrum of both single 3 and quad 3 nm DH under current injection of 500 A/cm$^2$. The wavelength shows slight red shift ~ 3 nm from single 3 nm to quad 3 nm DH, which might be due to the increased indium incorporation at the interfaces in the quad 3 nm DH.

Based on the hot electron overflow mode introduced in Chapter 3, electron overflow percentile was calculated with increased SEI thickness, as shown in **Figure 4.10**. For simplicity, we assume that the electrons move in the normal direction to the hetero-interfaces. Under the flat-band condition (*i.e.* the net potential drop across the active region V = 0), the 5 + 5 nm-thick SEI would result in a minimum overflow percentile of 23.5%, while increasing the SEI thickness to 20 + 20 nm and 30 + 30 nm would reduce the electron overflow to less than 1%. Under the bias corresponding to V = 0.1 V drop across the active region, the overflow for the 5+5 nm-thick SEI increases to 42.6%, while 20 + 20 nm and 30 + 30 nm exhibits overflow only 1.5% and 0.12%, respectively. These results suggest that a thicker SEI will efficiently reduce the electron overflow for a single 3 nm DH. Besides, it is noted that more steps in the SEI would result in smaller step height and thus less gained kinetic energy for the electrons from the potential and thus reduced electron overflow, when the energy steps are equal to or larger than the LO phonon energy. However, growth related issues in terms of the effect of SEI on the material quality and strain inside the active region should also be taken into consideration when optimizing the SEI layer stack.

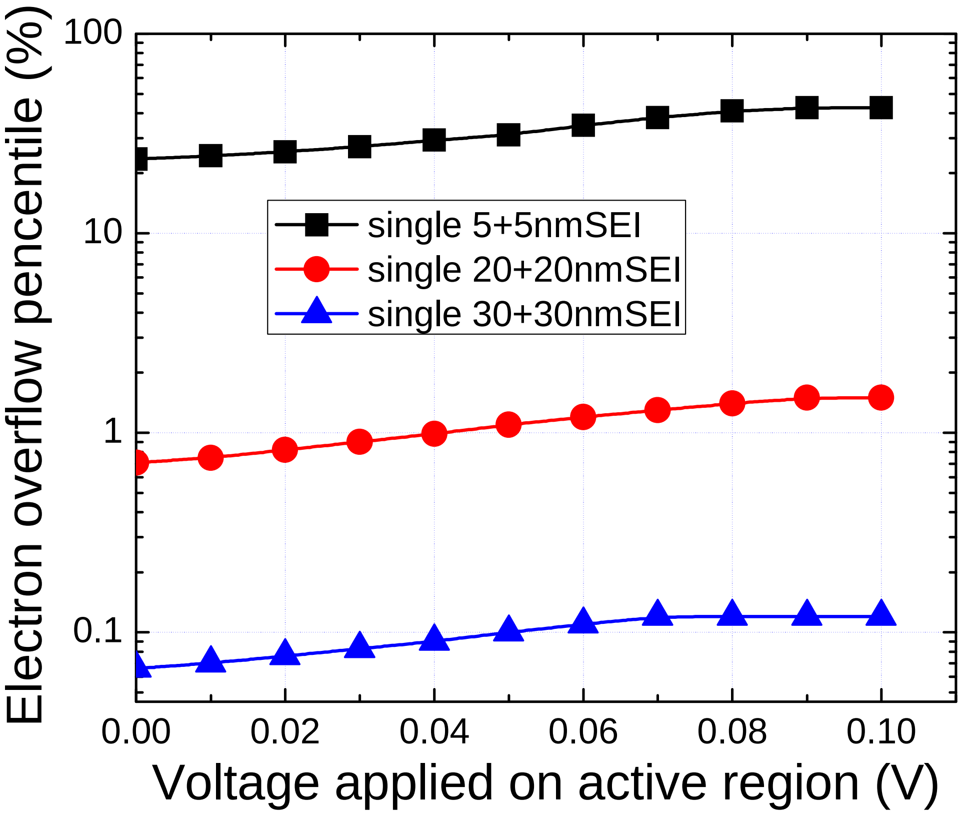

**Figure 4.10** Electrons spillover percentile dependence on the SEI thickness and applied voltage on the single 3 nm active region.

Experimentally, as presented in **Figure 4.11**, by increasing the SEI thickness to 20 nm + 20 nm, the single 3 nm shows about 15% lower peak EL efficiency compared to quad DHs, which is much better than those shown in **Figure 4.7**. This can be attributed to the much less electron overflow with increasing the SEI thickness. However, at high injection levels, the EL efficiency degrades very fast for single DH, *i.e.*, at 500 A/cm$^2$, the EL efficiency was reduced down to half of quad DHs due to the increased electron overflow for thinner active regions but this discrepancy is still much smaller than that obtained for 5 nm + 5 nm SEI case, which is about 3.5 times. The staggered SEI LED exhibits intermediate EL efficiency and less efficiency droop compared to the one with 20 + 20 nm SEI. Further optimizations regarding to this particular structure need to be performed to enhance the EL efficiency. Although from power dependent PL measurements, the optical quality of both single 3 nm DH and quad 3 nm DH with 30 nm + 30 nm thick SEIs seem to bode well, those with 30 nm +30 nm SEI exhibit consistently lower EL efficiency.

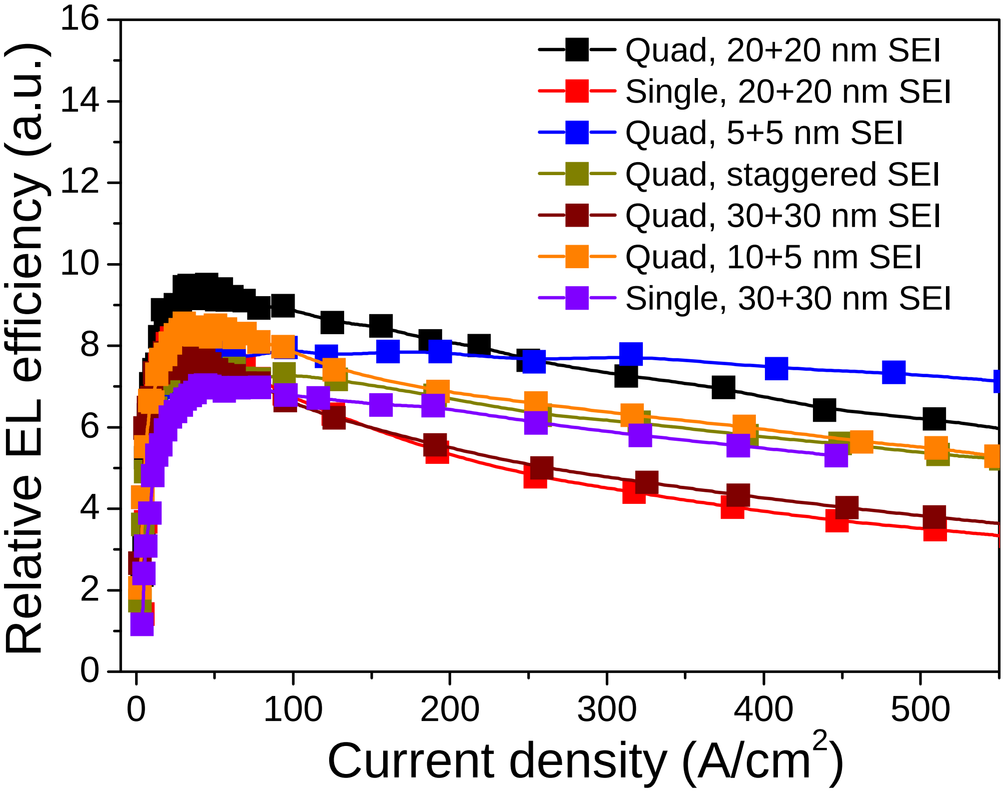

**Figure 4.11** EL efficiencies for various LEDs structures with different active region designs and SEI structures

### 4.3.3 Conclusion

By optimizing the SEI structures, mainly increasing the thickness, the EL efficiency has been improved considerably for single 3 nm DH with 20 + 20 nm SEIs owing to the reduced electron overflow. However, further increasing the SEI thickness degraded the material quality which offers lower EL efficiency and PL intensity as well. Although the staggered SEI LED shows intermediate EL efficiency, the efficiency droop for this particular structure is reduced. Further optimization for this structure including slight reducing the total thickness needs to be done.

## 4.4 Ga doped ZnO as transparent *p*-contacts

### 4.4.1 Motivation

To achieve high extraction efficiency and also reliability in LEDs, *p*-type GaN ohmic contacts with low- resistance and high optical transparency are crucial. Conventionally, thin semi-transparent bilayer Ni-Au (typically 5 nm-5 nm)[69,70] and indium tin oxide (ITO) films have been extensively investigated and utilized as ohmic contact layers to *p*-type GaN. However, the maximum transmittance of Ni-Au bilayers providing acceptable *p*-type ohmic contacts is only around 65-70% in the visible wavelength range and Au-based contacts can lead to poor device reliability due to the poor thermal stability of Au[71]. Although ITO-based contact layers, including metal-ITO bi- and multi- layers (e.g. Ni-ITO[71], In-ITO [72], Sn-Ag-ITO[73]) provide good p-type ohmic contacts and are highly transparent (~90-95%) in the visible spectrum, the potential scarcity of In is worrisome for the rapidly growing flat panel display and illumination industries. As an alternative, ZnO-based transparent conducting oxides (TCOs) appear to be among the most attractive material systems due to their structural and thermal compatibility with GaN as well as their lower cost. As such, ZnO doped with Al (AZO[74,75]) or Ga (GZO[76]) has received considerable attention for its unique properties such as low resistivity and high transparency which is extremely attractive for InGaN based LED applications. It has been reported that 1μm-thick GZO films prepared by pulsed laser deposition (PLD) have a sufficiently low resistivity of $2.92\times10^{-4}$ Ω-cm and a transmittance of 94% in the visible range[77]. PLD deposited AZO with thickness of 580 nm exhibited a resistivity of $1.8\times10^{-4}$ Ω-cm while possessing an optical transmittance up to 91%[75]. Recently, we have demonstrated that the transparency of epitaxial GZO by MBE on sapphire can reach ~95% while maintaining an electrical resistivity below $\sim3 \times 10^{-4}$ Ω-cm for 430 nm-thick films.

Non-uniform 3-dimensional current distribution especially in the *p*-type contact layers of the LEDs could result in serious problems such as local heat generation, early saturation of light emission intensity, and filamentation as well as shortened device lifetime[78,79,80]. Therefore, it is essential to attain contacts to *p*-type GaN for excellent current spreading with negligible current crowding to achieve reliable operation.

We demonstrate that 250 μm in diameter and unpackaged InGaN LEDs with GZO *p*-contact layers can be operated stably without any indication of degradation under a 100 mA DC current stress (on-wafer test configuration without any heatsink - corresponding to 318 A-cm$^{-2}$) for duration of 30 minutes used in the current experiment. Moreover, the use of GZO reduced the efficiency droop due to improved current spreading on *p*-type GaN as well as exhibiting much better contact stability under high current density operation (up to 4700 A-cm$^{-2}$ under pulsed operating conditions).

### 4.4.2 Experimental procedures

The studied LED active region structures were composed of 6 periods of 2-nm-thick $In_{0.14}Ga_{0.86}N$ quantum wells with 12 nm $In_{0.01}Ga_{0.99}N$ barriers. A 10-nm-thick undoped

ZnO buffer layer followed by a 430-nm-thick GZO film was grown by MBE on the *p*-type GaN at a substrate temperature of 300 °C under metal-rich conditions (metal (Ga+Zn) to oxygen ratio >1). These conditions are consistent with the best growth conditions for GZO on *a*-sapphire substrates by MBE, producing highly conductive films with transparency as high as ~95% in the visible range. The *in situ* monitoring of the reflection high energy election diffraction (RHEED) pattern evolution revealed that the GZO initially grew in a 2-dimensional (2D) growth mode on top of the *p*-GaN, and then the RHEED pattern gradually changed towards 3-dimensional (3D) one. From high-resolution X-ray diffraction (HRXRD) characterization for both symmetric and asymmetrical two-theta-omega scans, the *c* and *a* lattice constants of these GZO films were determined to be 5.208 and 3.256 Å, respectively. The calculated lattice constants are very close to those of bulk ZnO, indicating a very small lattice distortion when Ga atoms in high concentrations are incorporated into ZnO. Room temperature Hall measurements show that the as grown GZO on *p*-GaN has a low resistivity of $2\times10^{-4}$ Ω-cm which is the basis for current spreading in LED applications.

After patterning, the GZO layers were partially etched in diluted aqueous HCl solution (0.5%), and then the InGaN LED structures were dry-etched to expose the *n*-GaN layer with a mesa size of 250 μm in diameter. Ti/Al/Ni/Au (30/100/40/50 nm) metallization annealed at 800 ºC for 60 seconds was used for *n*-type ohmic contacts. Finally, 40/50 nm-thick Ti/Au contact pads with 75 μm in diameter were deposited on the top of the mesa (on top of GZO). 5/5 nm- thick Ni/Au contacts were also employed instead of the GZO current spreading layer on LEDs from the same wafer for comparison.

### 4.4.3 Results and discussions

Prior to electrical characterization of the InGaN LEDs, we evaluated the current-voltage characteristics between the GZO and *p*-GaN layers. As clearly seen in the inset of **Figure 4.12** (a), the as-grown GZO shows ohmic behavior on *p*-GaN layers without metal contact pads deposited on the top of GZO.

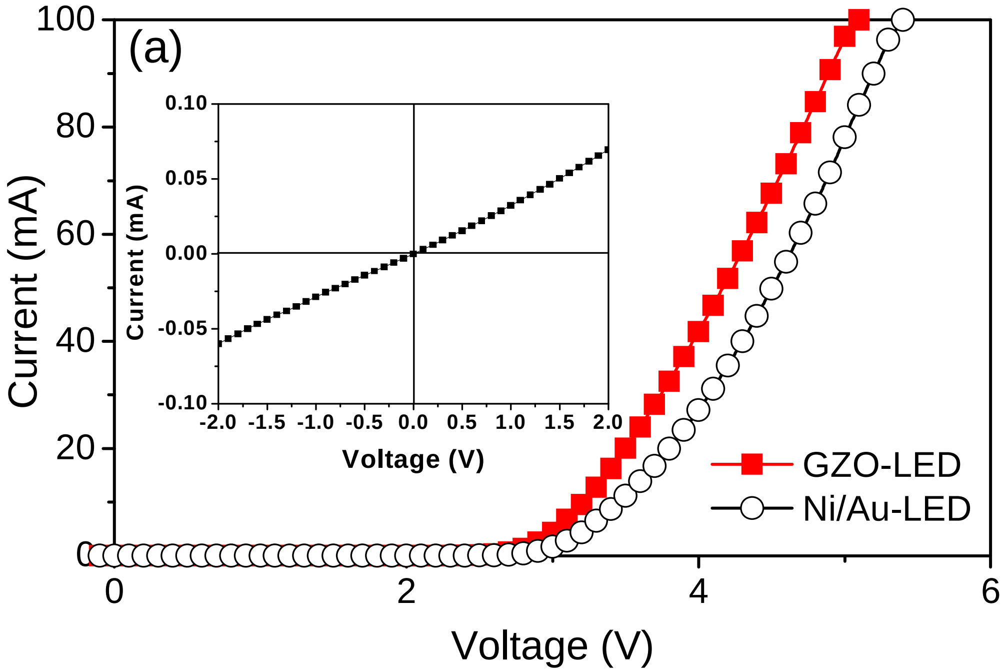

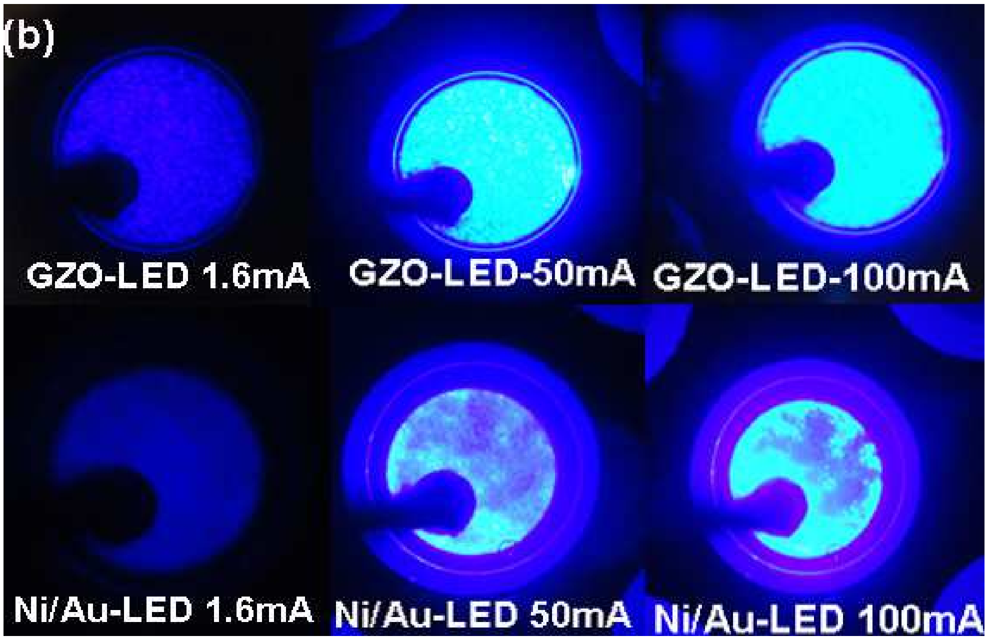

**Figure 4.12**(a) Current-voltage (I-V) characteristics of the LEDs with GZO- and Ni/Au electrodes. The inset shows current-voltage characteristics of the GZO contacts on *p*-GaN measured in transmission lines patterns having 40 μm contact spacing; (b) photographs of operating LEDs taken at different current levels under DC biased mode.

**Figure 4.12** (a) compares the typical I-V characteristics of the LEDs with GZO and Ni/Au current spreading layers. The LEDs with GZO contacts (GZO-LEDs) have virtually the same vertical series resistance (typically ~18-22 Ohm) as that of the Ni/Au-LEDs (typically ~17-23 Ohm). We should mention that it is the lateral resistance which plays a role in current spreading and filamentation. It can also be seen that the forward voltage measured at 20 mA is 3.5 V and 3.7 V for GZO-LEDs and Ni/Au-LEDs, respectively. The forward voltage at 20 mA for GZO-LEDs is compara comparable to or lower than the reported values for LEDs with ITO based current spreading layer which is in the range of 3.42-4.28 V [72,81,82]. The photographs in **Figure 4.12** (b) illustrate the difference between a Ni/Au-LED and a GZO-LED in terms of current crowding. We see that the filamentation phenomena due to the severe current crowding which occurs in Ni/Au-LEDs under higher DC current levels, i.e. 50 mA (159 A/cm$^2$) and 100 mA (318 A/cm$^2$) while it is not observed in the GZO-LEDs up to the maximum current applied (100 mA), which can be attributed to better current spreading in the case of GZO *p*-contacts.

In addition to the output power, the device reliability at high current levels is extremely important for LEDs especially for high power LEDs. The different current spreading behaviour for the Ni/Au-LEDs and GZO-LEDs would affect the LED reliability due to the induced differences in local junction heating. Hence, for device aging purposes we applied DC currents of 50 mA (159 A/cm$^2$), 75 mA (238 A/cm$^2$), and 100 mA (318 A/cm$^2$) for up to 30 min using on-wafer testing configuration without employing any heatsink, and observed the evolution of I-V characteristics and the light output intensity (collected by UV enhanced silicon photodetector that is placed just above the LEDs) for both types of LEDs before and after aging.

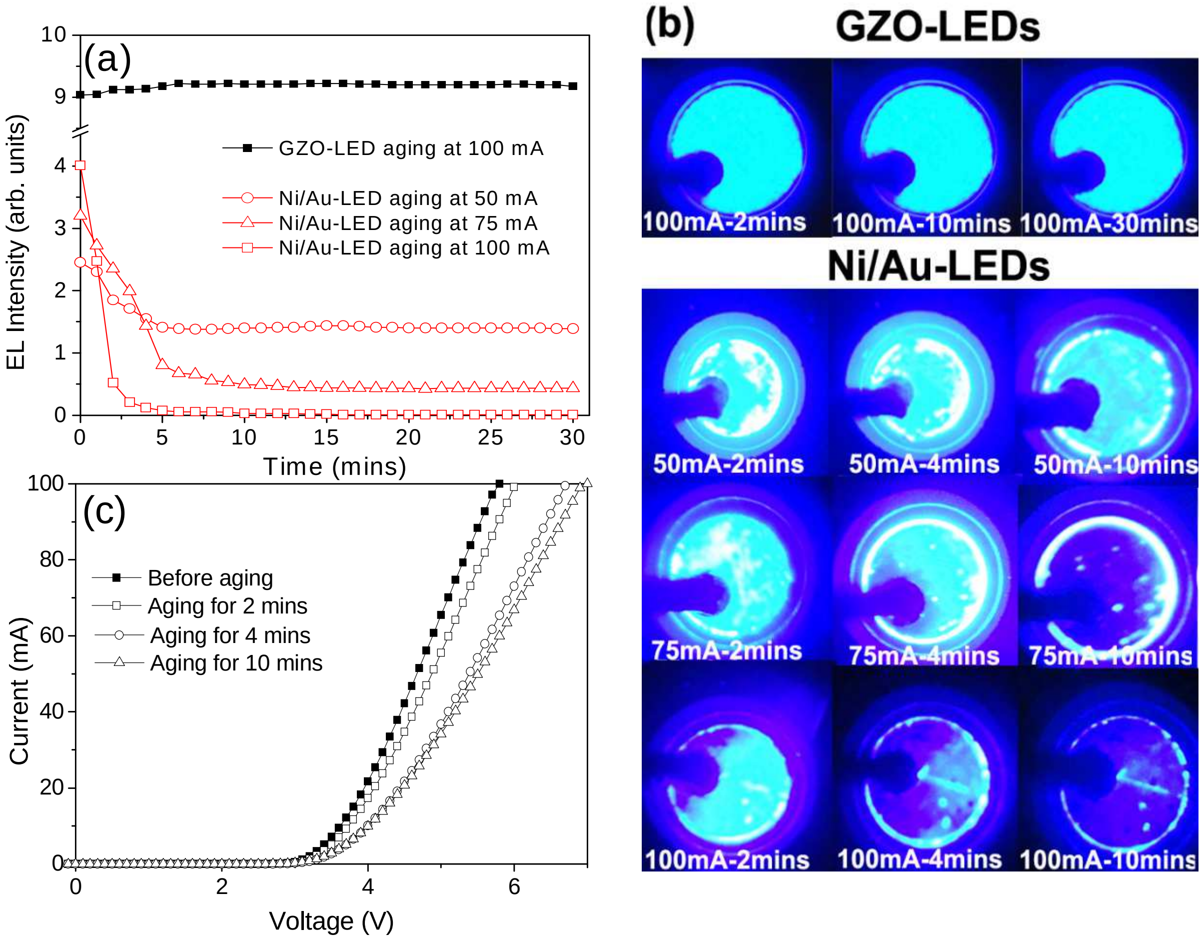

**Figure 4.13** (a) Measured output EL intensity represented by photocurrent versus time for Ni/Au-LEDs (at 50, 75 and 100 mA) and GZO-LEDs (at 100 mA); (b) photographs of GZO-LEDs emitting for 2, 10, and 30 min at DC current of 100 mA (top three images in the first row) and photographs of Ni/Au-LED operating for 2, 4, and 10 min emitting at DC currents of 50, 75, and 100 mA. The white emission is due to the saturation of CCD camera; (c) I-V curves for Ni/Au-LEDs measured before and after operating at 75 mA for 2, 4, and 10 min.

Although the overall device efficiency for Ni/Au-LEDs was minimally affected at 50 mA, significant degradation of the device and light output was observed at 75 and 100 mA, most likely as a result of current crowding. Typically, according to our observations, the Ni/Au-LEDs degrade very fast during the first 5 mins of operation. We measured the current-voltage (I-V) characteristics before and after 75 mA aging for Ni/Au-LEDs shown in Figure 4.13 (c). We can clearly see that the forward voltage at 20 mA increases from ~3.75V (before aging) to ~3.9V (after 2 mins aging), 4.4V (after 4 and 10 mins aging), respectively. Such increased contact resistance is consistent with current crowding in Ni/Au-LEDs with increased current. To underscore the abovementioned degradation, the photographs of light intensity distribution in **Figure 4.13** (b) clearly show device degradation in Ni/Au-LEDs after only 2 mins of operation under 75 mA and 100 mA. The current crowding becomes more severe with the aging progresses. Furthermore it appears much more prominently at the edge of the semitransparent Ni/Au current spreading layer.

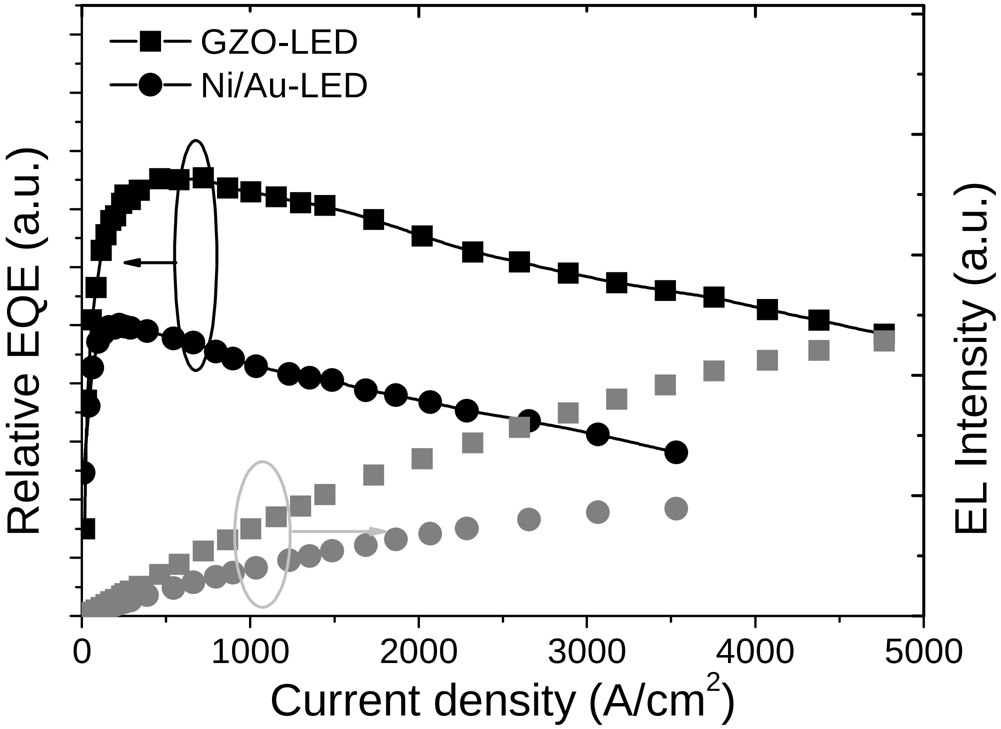

**Figure 4.14** Pulse EL measurements for LEDs with GZO and Ni/Au current spreading layers.

High-current pulsed EL characteristics were also measured in the on-wafer testing configuration to evaluate the quantum efficiency as a function of the injection current. **Figure 4.14** shows the relative external quantum efficiency under pulsed condition (1 μs rectangular pulses at 1 kHz repetition rate) for current densities up to 4700 A/cm$^2$ for GZO-LEDs and 3500 A/cm$^2$ for Ni/Au-LEDs (the Ni/Au devices failed beyond this current density due to heating and subsequent destruction of contacts). The GZO-LEDs show 50% higher EL intensity due to the higher optical transparency of the GZO current spreading layer. Furthermore, although it does not seems to be significant, GZO-LEDs exhibit reduced efficiency droop (~28%) compared to that of Ni/Au-LEDs (~43%) up to current densities as high as 3500 A/cm$^2$. Recalling **Figure 4.13**, this reduced efficiency droop can be related to the alleviated current crowding effect and hence less carrier leakage in GZO-LEDs.

### 4.4.4 Conclusion

We have demonstrated that GZO-LEDs provide 50 % more light output compared with Ni/Au-LEDs. They also have relatively good stability under 100 mA DC-bias up to 30 min due to the lack of current crowding, whereas for Ni/Au-LEDs, fast degradation during the first 5 min operation under DC-biased 75 mA and 100 mA was observed. This much more severe current crowding in Ni/Au-LEDs could cause device degradation during operation.

# Chapter 5 Conclusions and future research

## 5.1 Conclusions

InGaN based LEDs have been widely used in displays of TV, computers, and cell phones. And more applications have been focused on the general lighting market due to their high efficiency and long lifetime. However, high power LEDs suffer efficiency droop at high injection levels. The fitting results as discussed in Chapter 2.2 along with theoretical and experimental results by other researchers have ruled out the possibility of Auger recombination in wide band gap GaN based LEDs. We have proposed that the poor hole transport in GaN is a contributing factor for such efficiency droop. For m-plane GaN, the hole concentration and hole mobility is higher than c-plane counterpart due to the smaller effective mass in m-plane case. Besides, the same LED structures grown on c-plane and m-plane bulk GaN show quite different efficiency behaviors with injection current. The LED structure with thicker and higher barriers (12 nm $In_{0.01}Ga_{0.99}N$) intentionally designed for more pronounced efficiency droop presents negligible efficiency droop for the one grown on m-plane substrate while nearly 25% efficiency droop was observed for that grown on c-plane substrate. Further LED structure designs with lower and thinner barriers favor the efficiency retention. Moreover, the single wide 9 nm DH without any barriers blocking hole transport was introduced and exhibited higher relative EQE and efficiency retention albeit the EQE rising rate with current density was slowed down compared to MQW structures, which can be partially ascribed to increase non-radiative SCH coefficients and partially due to the increased separation of electron and hole wavefunction.

LEDs with EBL shows much higher (3-5 times) relative EQE compared with those without EBL, which hints to the effect of electron overflow on the efficiency droop. Based on the experimental data and theoretical calculations, we also suggested the hot electron overflow model to interpret the efficiency droop. We introduced the two-step SEI just before the active region to thermalize/cool down the injected hot electrons due to the large band discontinuity. A uncoupled MQW LED with sole SEI shows ~10% higher peak relative EQE compared to that with sole EBL indicating that EBL can be replaced by SEI without sacrificing efficiency reduction due to the reduced hole injection efficiency in the EBL case.

Armed with SEI in our LED structures, we have played with various active region designs to maximize the output power/efficiency. By using MDH structures, the relative EL efficiency was enhanced greatly by increasing number of DH and quad 3 nm DH shows even higher EL efficiency compared to single 9 nm DH and MQW structures. With more DHs in the active region, the LED can handle more injection power and thus favors high power applications. Our optimization of SEI structures increasing SEI thickness from 5 nm to 20 nm per step further improved relative EL efficiency for single 3 nm DH and move the peak efficiency of 3 nm DH to the comparable level with quad 3 nm DH albeit single 3 nm DH shows ~2 time lower EL efficiency than quad 3 nm DH at high injection levels. This onwards approves that hot electron overflow is the most dominant reason for the efficiency droop in the GaN based LEDs since thicker SEI can reduce the electron overflow as obtained by first order calculation.

## 5.2 Future research

### 5.2.1 Enhance hole concentrations

From aforementioned discussions supported by massive experimental results and theoretical calculations, we can conclude that in order to mitigate efficiency droop issues occurring in the InGaN based LEDs, electron and hole concentrations should be balanced or hole concentrations must be further increased. However, standard GaN growth conditions by MOCVD lead to hole concentration typically on the order of 1-4×$10^{17}$ $cm^{-3}$ since the Mg activation energy in GaN is high and the formation of the Mg-H complexes inhibit the ionization of Mg acceptors. Using higher growth pressures and lower temperatures can enable higher hole concetrations[83,84]. But higher growth pressures and lower growth temperatures lead to material degradation[83]. In addition, this approach is limited by self-compensation attributed to nitrogen vacancy complexes in *p*-GaN. Due to the motion of Fermi level, nitrogen vacancies are expected to have a major impact on *p*-GaN. However, with higher $NH_3$ partial pressures during growth and careful post annealing, the nitrogen vacancy density can be minimized.[85] For *p*-GaN growth with Ga polarity, the Mg incorporation can induce the stacking faults from GaNGaN to GaNMgNGa, inverting the GaN polarity from Ga-face to N-face. As the growth proceeds, additional Mg atoms migrate towards these stacking faults leading them to develop along several inclined planes, and eventually form pyramidal-shape defects (called pyramidal inversion domains (PIDs)). δ- doping of Mg into GaN was found to be virtually free of such PIDs extended defects due to the hindering of the vertical diffusion of Mg inhibited by GaN interlayers, which in turn improved the surface morphology[84]. It was also reported that Mg δ- doping improves not only the *p*-type GaN conduction, but also significantly suppresses the dislocation densities, which is beneficial to the leakage current and lifetime of LEDs.[86] It has also been demonstrated that incorporating Mg-doped AlGaN/GaN superlattice structure into devices could enhance the hole conduction in the lateral direction. However, the enhancement of hole conduction in the vertical direction by employing a superlattice structure is limited because a superlattice structure simultaneously introduces potential barriers for hole conduction in the vertical direction. Using the Mg δ- doping technique, hole concentration as high as $10^{18}$ $cm^{-3}$ has been achieved by MOCVD growth method[87]. We expect that, by tuning the growth parameters (including growth temperature, Mg flow rate, interruption time and un-doped GaN spacer layer thickness) during growth of Mg δ- doped GaN, the solubility limit of Mg into GaN can be affected in a controlled way, allowing to enhance the incorporation of Mg ions, to hinder the self-compensation mechanisms and therefore improve the concentration of active carriers in the layers.

Preliminary results have been obtained by tuning the undoped GaN spacer thickness in the Mg δ- doping profile as schematically depicted in **Figure 5.1**.

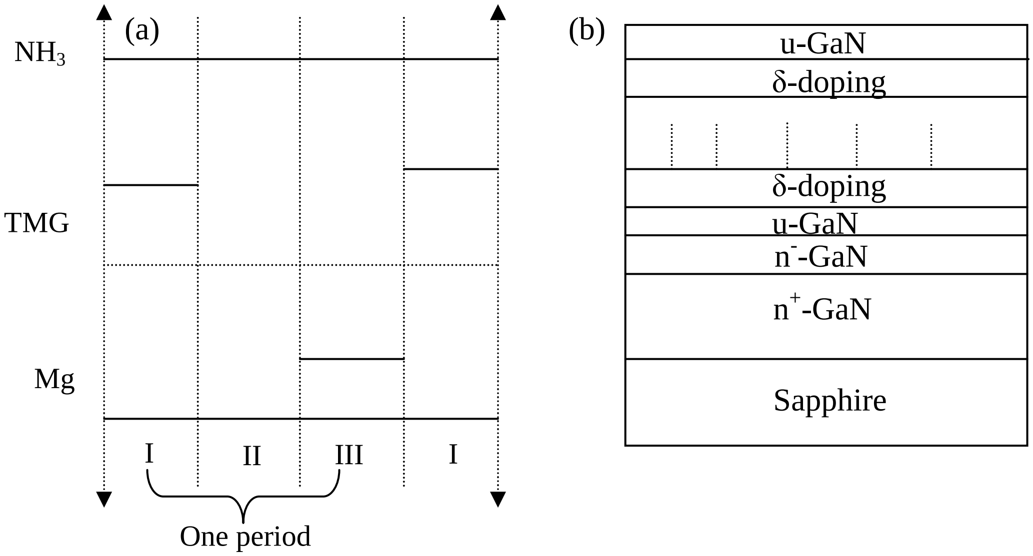

**Figure 5.1**: (a) δ- doping profile implementation: Stage I: undoped GaN growth (u-GaN); II: Nitridation; III: Mg incorporation (constant Mg molar flow for all the samples); (b) Side view of the δ-doped p-GaN structure.

For *p*-type doping studies, a p-n$^-$-n$^+$ layer structure was grown, as shown in **Figure 5.1** (b). The growth conditions for top Mg δ- doping GaN have been varied by changing the undoped GaN spacer thickness from 5 nm, 7.5 nm, to 10 nm. The bottom n type layers were Si-doped with carrier concentration around $3\times10^{18}$ cm$^{-3}$. This was capped with lightly Si doped GaN ($5\times10^{17}$ cm$^{-3}$) layer of 200 nm thickness, and finally 500 nm Mg δ-doping GaN. This structure is useful for making electrical measurements on Mg doped layer because the resulting p-n junction has a high reverse breakdown voltage; as a consequence a high bias can be applied between two *p*-contacts and only hole current will flow between them, enabling accurate measurements. In addition, by forming p-n junction devices, we can test the I-V characteristics for the p-n junctions simultaneously.

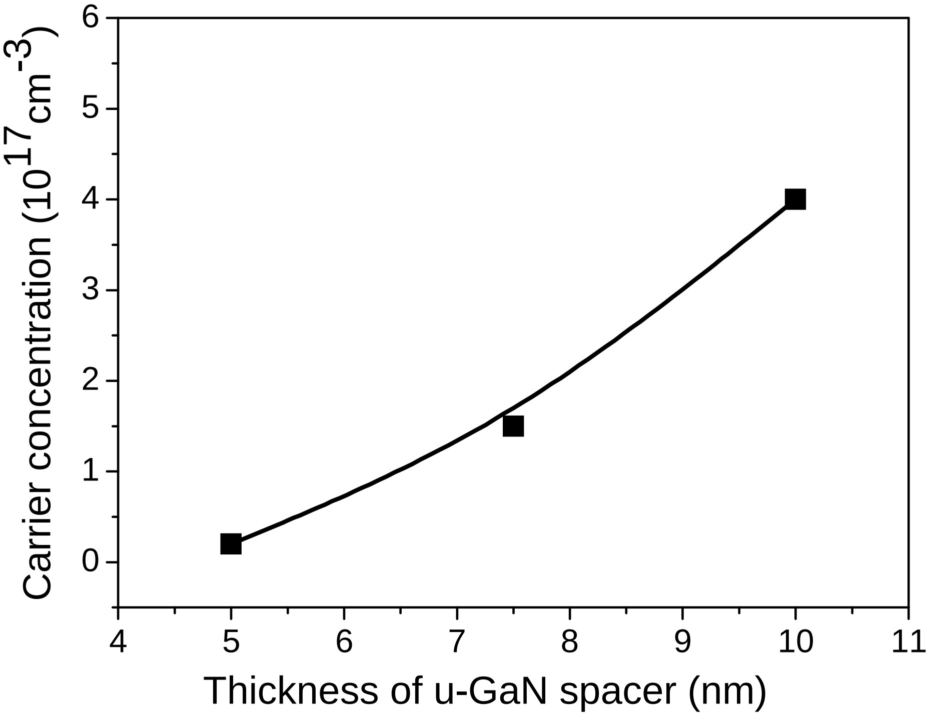

**Figure 5.2**: Measured hole concentration as a function of u-GaN spacer thickness

As presented in **Figure 5.2**, with increasing u-GaN spacer thickness, the hole concentrations continue improving. The highest hole concentration obtained so far is $4\times10^{17}$ cm$^{-3}$ with u-GaN thickness of 10 nm. Although the obtained hole concentration is still less than our standard continuous Mg doping *p*-type GaN with hole concentration $7\times10^{17}$ cm$^{-3}$, the Mg δ-doping GaN optimization is still on the way. Further optimizations are required in order to achieve higher hole concentration including (1) further increasing u-GaN spacer thickness; (2) optimizing Mg source flow; (3) optimizing u-GaN spacer growth V/III ratio.

### 5.2.2 Wide active region quality enhancement

As discussed in Chapter 4, in order to achieve high performance LEDs at high injection levels, the active layer thickness need to be increased to handle more current injection.

However, as we all know increasing the thickness of InGaN layers will deteriorate their material quality owing to the accumulated strain and eventually relaxation could occur in a form of large density of dislocations, which prevents efficient radiative recombination. To compensate the material degradation with increasing the active layer, the dislocation density in the bottom GaN buffer layer needs to be minimized so that it won’t propagate into the active layer. One of the efficient methods to improve GaN quality is to employ *in-situ* SiNx approach, which is developed in our group. A typical AFM image of the GaN template grown with this approach is shown in **Figure 5.3**. The counted threading dislocation density is about $8\times10^{7}$ $cm^{-2}$. We should note that this value is the minima since more buried dislocations can be revealed by wet etching of the GaN surface. However, with this *in-situ* SiNx method the dislocation can still be reduced down to mid $10^{8}$ $cm^{-2}$, which is an order of magnitude lower than coniventional GaN template grown on sapphire. Other methods that can be incorporated to further reduce the dislocation density and also be compatible with current *in-situ* SiNx approach include sapphire substrate patterning.

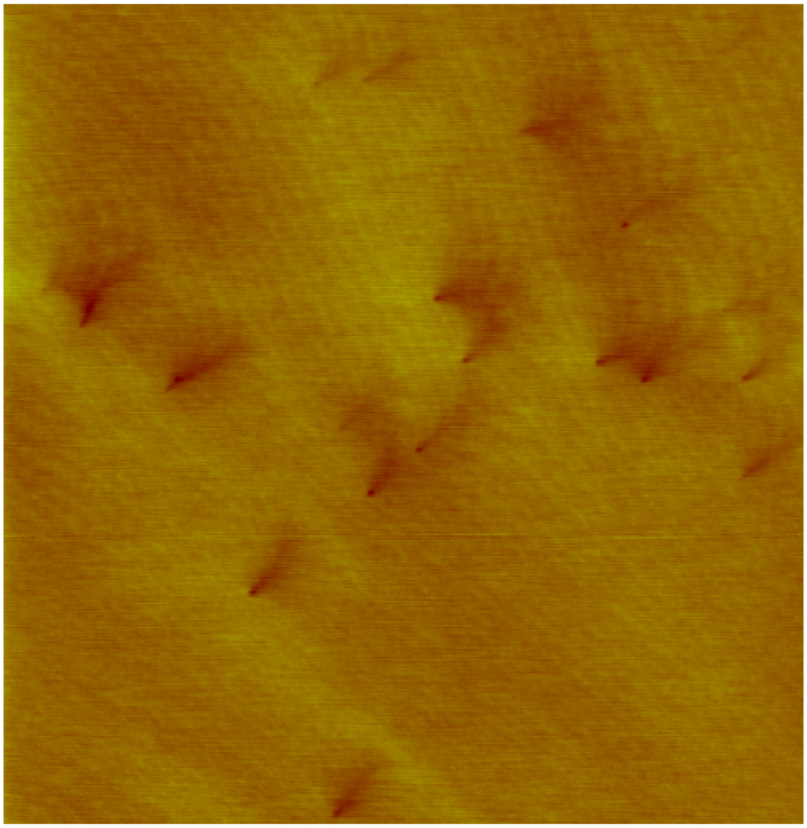

**Figure 5.3** AFM image (5 µm×5 µm) of GaN template with *in-situ* SiNx

The sapphire substrate patterning on the micrometer and nanoscale range has been shown to improve light output power attributed to not only the enhanced IQE due to the reduced dislocation density but also the light extraction efficiency (LEE)[88,89,90]. By using the patterned substrates, the LEE can be improved through the light scattering from the nitride epilayer and patterned sapphire interface compared with the *in-situ* SiNx ELO method. Various methods have been developed to form different sapphire substrate patterns. Gao *et al*,[91] successfully grew InGaN LED structures on pyramidal patterned sapphire substrates in microscale (MPSS) and nanoscale (NPSS) and improved the light output power of about 29% and 48% with MPSS and NPSS, respectively at an injection current 20 mA, compared with planar sapphire substrates. Chiu *et al*.[90], utilized $SiO_2$ nanorod-array patterned sapphire substrates (NAPSS) serving as a template for the nanoscale ELO of GaN to produce high efficiency LED structures. The two approaches are summarized as following:

i. Gao's approach:

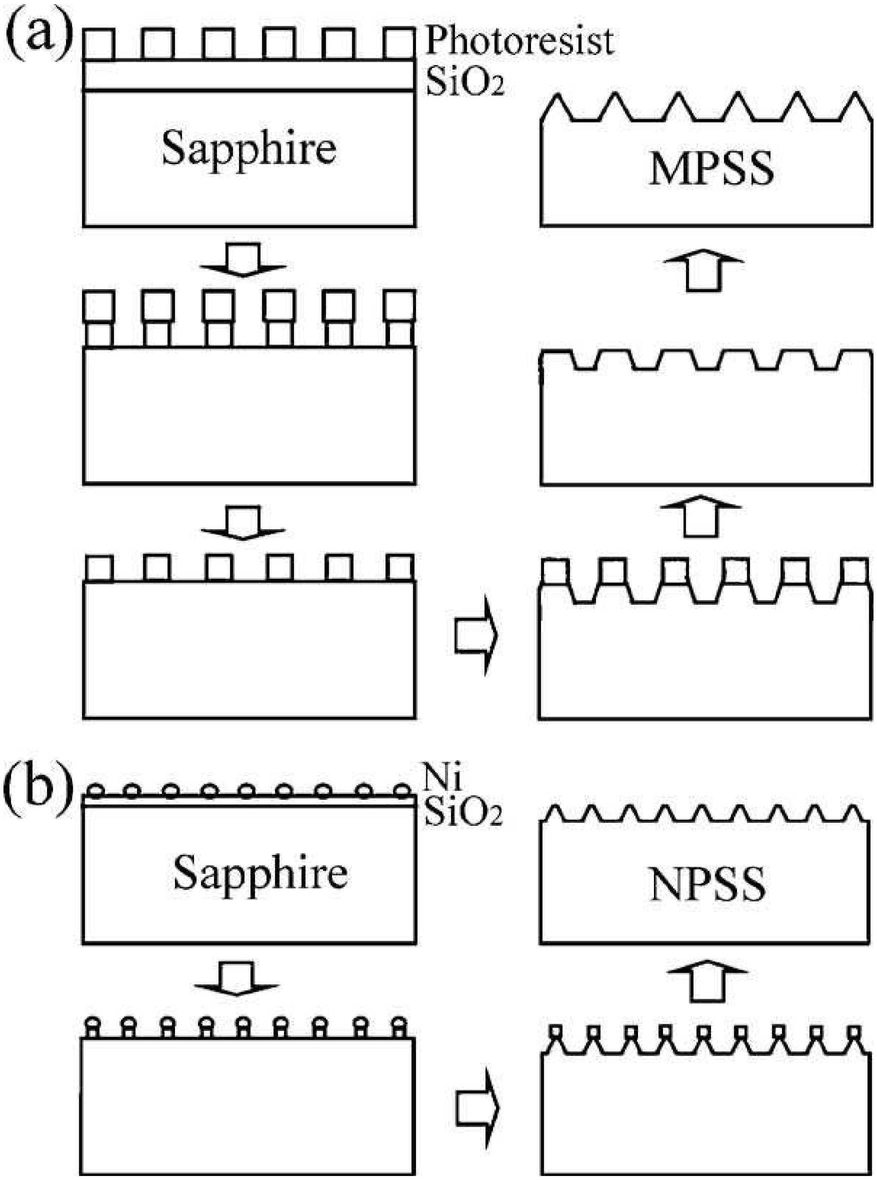

**Figure 5.4**: Schematic description of fabrication procedures for (a) MPSS; (b) NPSS

Firstly, 100-500 nm thick $SiO_2$ film was deposited on sapphire substrates by plasma-enhanced chemical vapor deposition (PECVD). For fabrication of MPSS, the circular photoresist array with a 3 µm in diameter and 3 µm spacing was formed by standard photolithography. And then, the $SiO_2$ film was etched for 10-50 s in a buffered oxide etching solution using the photoresist as a mask. After $SiO_2$ patterning, the photoresist was removed and $SiO_2$ array was formed as the mask for following sapphire substrate etching, which was treated in a mixture of $H_2SO_4$ and $H_3PO_4$ ($H_2SO_4$: $H_3PO_4$=3:1) for 3 min. Finally, $SiO_2$ mask was removed in HF solution. Wet etching of substrate was continued for 2 min to form triangular pyramidal patterns, as schematically depicted in **Figure 5.4** (a) with SEM image shown in **Figure 5.5** (a).

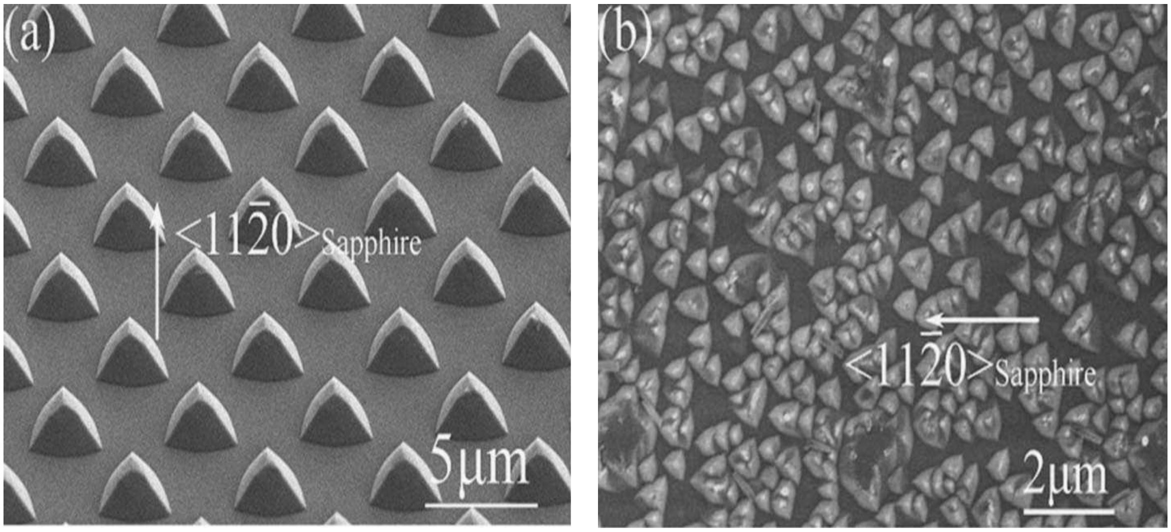

**Figure 5.5** SEM images of pyramidal patterned sapphire substrates prepared by wet etching (a) MPSS; (b) NPSS.

For the fabrication of the NPSS, a nickel layer was deposited on the $SiO_2$ film by E-beam evaporation. The nickel was self-assembled by annealing and formed to nanosized islands. The $SiO_2$ film was etched in a dry etcher using nickel nanoislands as mask. The residual $SiO_2$ was nanosized and served as the mask for the sapphire substrate etching. The sapphire substrate with nanosized $SiO_2$ masks were wet etched for 3 min in a mixture of $H_2SO_4$ and $H_3PO_4$ ($H_2SO_4$: $H_3PO_4$=3:1). The fabrication procedure was schematically depicted in **Figure 5.4** (b) with SEM image shown in **Figure 5.5** (b).

ii. Chiu's approach:

The preparation of the $SiO_2$ NPSS template started with the deposition of a 200 nm thick $SiO_2$ layer on sapphire by PECVD, followed by the evaporation of a 10 nm nickel layer, and the subsequent rapid thermal annealing with a flowing nitrogen gas at 850 $^oC$ for 1 min. The resulting self-assembled Ni clusters then served as the etch masks to form a $SiO_2$ nanorod array using reactive ion etch system for 3 min. Finally the sample was dipped into a heated nitric acid solution ($HNO_3$) at 100 $^oC$ for 5 min to remove the residual Ni masks. The obtained $SiO_2$ nanorods were approximately 100-150 nm in diameter with a density of $3\times10^9$ $cm^{-2}$. The spacing between nanorods was about 100-200 nm. As deposition process started, localized and hexagonal islandlike GaN nuclei were first formed from the sapphire surface to initiate GaN overgrowth.

Based on the aforementioned approaches for fabricating PSS and associated results, I propose to develop our own PSS technique and combine *in-situ* SiNx ELO technique to grown low dislocation density GaN templates for high performance InGaN LED applications, especially for thicker InGaN active layer, *i.e.*, single thick DH ( > 12 nm) or multi-DH layers (up to 10).

# References

[1] Y. Narukawa, M. Ichikawa, D. Sanga, M. Sano, and T. Mukai, J. Phys. D: Appl. Phy. 43, 354002 (2010).

[2] 2011 LEDs magazine, http://ledsmagazine.com/news/8/3/12

[3] M. Kneissl, et al, Semicond. Sci. Technol. 26, 014036 (2011).

[4] S. Yamamoto, Y. Zhao, C.C. Pan, R.B. Chung, K. Fujito, J. Sonoda, S.P. Denbaars, and S. Nakamura, Appl.Phys.Exp., 3, 122102 (2010).

[5] H. Zhong, A.Tyagi, N.N. Fellows, F. Wu, R.B. Chung, M. Saito, K. Fujito, J.S. Speck, S.P. DenBaars, and S. Nakamura, Appl.Phys. Lett., 90, 233504 (2007).

[6] H.Morkoç, "Handbook of Nitride Semiconductors and Devices", Volume 3, Chapter 1, Wiley-VCH, 2008.

[7] Y.J. Lee, C.H. Chiu, C.C. Ke, P.C. Lin, T.C. Lu, H.C. Kuo, and S.C. Wang, IEEE J. Quant. Electron. **15**, 1137 (2009).

[8] A. Michiue, *et al.*, Proc. SPIE. **56**, 7216 (2009).

[9] B. Monemar and B. E. Sernelius, Appl. Phys. Lett. **91,** 181103 (2007).

[10] I. V. Rozhansky and D. A. Zakheim, Semiconductors **40**, 839 (2006).

[11] I. V. Rozhansky and D. A. Zakheim, Phys. Status Solidi A **204**, 227(2007).

[12] I. A. Pope, P. M. Smowton, P. Blood, J. D. Thomson, M. J. Kappers, and C. J. Humphreys, Appl. Phys. Lett. **82**, 2755 (2003).

[13] Min-Ho Kim, Martin F. Schubert, Qi Dai, Jong Kyu Kim, and E. Fred Schubert, Joachim Piprek and Yongjo Park, Appl. Phys. Lett. **91**, 183507 (2007).

[14] M. F. Schubert, J. Xu, J. K. Kim, E. F. Schubert, M. H. Kim, S. Yoon, S. M. Lee, C. Sone, T. Sakong, and Y. Park, Appl. Phys. Lett. **93**, 041102 (2008).

---

[15] Y. C. Shen, G. O. Mueller, S. Watanabe, N. F. Gardner, A. Munkholm, and M. R. Krames, Appl. Phys. Lett. **91**,141101 (2007).

[16] A. A. Efremov, N. I. Bochkareva, R. I. Gorbunov, D. A. Larinovich, Yu. T. Rebane, D. V. Tarkhin, and Yu. G. Shreter, Semiconductors. **40**,605 (2006).

[17] A. R. Beattie and P. T. Landsberg, Proc. R. Soc. Lond. A. **249**,1256 (1958).

[18] J. Hader, J. V. Moloney, B. Pasenow, S. W. Koch, M. Sabathil, N. Linder, and S. Lutgen, Appl. Phys. Lett. **92**, 261103 (2008).

[19] J. Xie, X. Ni, Q. Fan, R. Shimada, Ü. Özgür, and H. Morkoç, Appl. Phys. Lett. **93**, 121107 (2008).

[20] X. Ni, X. Li, J. Xie, Q. Fan, R. Shimada, Ü. Özgür, H. Morkoç, Proc. of SPIE.**7216**,53 (2009).

[21] C. B. Su, J. Schlafer, J. Manning, and R. Olshansky, Electron. Lett. **18**,1108 (1982).

[22] P. G. Eliseev, M. Osin'ski, H. Li, and I. V. Akimova, Appl. Phys. Lett. **75**,3838 (1999).

[23] Q. Dai, M. F. Schubert, M. H. Kim, J. K. Kim, E. F. Schubert, D. D. Koleske, M. H. Crawford, S. R. Lee, A. J. Fisher, G. Thaler, and M. A. Banas, Appl. Phys. Lett. **94**, 111109 (2009).

[24] S. Jursenas S. Miasojedovas, G. Kurilcik, and A. Zukauskas, Appl. Phys. Lett. **83** (2003) 66.

[25] X. Li, H.Y. Liu, X. Ni, Ü. Özgür, and H. Morkoç, Superlattices Microstructure, **47** (2010) 118.

[26] Ümit Özgür, Hadis Morkoç, H. Liu, X. Li, and X. Ni, Proc. of IEEE, **98**, 1180 (2010).

[27] A. Niwa, T. Ohtoshi, and T. Kuroda, Appl. Phys. Lett. 70, 2159 (1997)

[28] K. T. Tsen, R. P. Joshi, D. K. Ferry, A. Botchkarev, B. Sverdlov, A. Salvador, and H.

---

Morkoç, Appl. Phys. Lett. **68**, 2990 (1996).

[29] I. V. Rozhansky and D.A. Zakheim, Phys. Stat. Sol. A **204**, 227 (2009).

[30] M.L. Nakarmi, K.H. Kim, M. Khizar, Z.Y. Fan, J. Y. Lin, and H. X. Jiang, App. Phys. Lett., 86, 092108 (2005).

[31] X. Ni, X. Li, J. Lee, S. Liu, V. Avrutin, Ü. Özgür, H. Morkoç, A. Matulionis, T. Paskova, G. Mulholland, and K. R. Evans, Appl. Phys. Lett. **97**, 031110 (2010).

[32] X. Ni, X. Li, J. Lee, S. Liu, V. Avrutin, Ü. Özgür, H. Morkoç, A. Matulionis, J. Appl. Phys. **108**, 031112 (2010).

[33] X. Li, F. Zhang, S. Okur, V. Avrutin, S.J. Liu, Ü. Özgür, H. Morkoç, S.M. Hong, S.H. Yen, T.S. Hsu, A. Matulionis, Phys. Status Solidi A. **208**, 2907 (2011)

[34] M. McLaurin, T. E. Mates, F. Wu, and J. S. Speck, J. Appl. Phys. **100**, 063707 (2006).

[35] M. McLaurin and J. S. Speck, Phys. Stat. Sol. (RRL) **3**, 110 (2007).

[36] A. Niwa, T. Ohtoshi, and T. Kuroda, Appl. Phys. Lett. **70**, 2159 (1997).

[37] R. Langer, J. Simon, V. Ortiz, N. T. Pelekanos, A. Barski, R. Andre, and M. Godlewski, Appl. Phys. Lett. **74**, 3827 (1999).

[38] T. Deguchi, K. Sekiguchi, A. Nakamura, T. Sota, R. Matsuo, S. Chichibu, and S. Nakamura, Jpn. J. Appl. Phys. Part 2-Letters **38**, L914 (1999).

[39] Y. J. Sun, O. Brandt, M. Ramsteiner, H. T. Grahn, and K. H. Ploog, Appl. Phys. Lett. **82**, 3850 (2003).

[40] H. Tsujimura, S. Nakagawa, K. Okamoto, and H. Ohta, Jpn. J. Appl. Phys, 46, L1010 (2007).

[41] H. Yamada, K. Iso, M. Saito, H. Masui, K. Fujito, S. P. DenBaars, and S. Nakamura, Appl. Phys. Express **1**, 041101 (2008).

---

[42] H. Masui, H. Yamada, K. Iso, S. Nakamura, and S. P. DenBaars, J. Phys. D: Appl. Phys. **41**, 225104 (2008).

[43] S. Watanabe, N. Yamada, M. Nagashima, Y. Ueki, C. Sasaki, Y. Yamada, T. Taguchi, K. Tadatomo, H. Okagawa, and H. Kudo, Appl. Phys. Lett. **83**, 4906 (2003).

[44] A. David, M.J. Grundmann, J.F. Kaeding, N.F. Gardner, T.G. Mihopoulos, and M.R. Krames, Appl. Phys. Lett. **92**, 053502 (2008).

[45] J.P. Liu, J.H. Ryou, R.D. Dupuis, J. Han, G.D. Shen and H.B. Wang, Appl. Phys. Lett. **93**, 021102 (2008).

[46] J.H. Zhu, S.M. Zhang, H. Wang, D.G. Zhao, J.J. Zhu, Z.S. Liu, D.S. Jiang, Y.X. Qiu, and H. Yang, J. Appl. Phys. **109**, 093117 (2011).

[47] N. F. Gardner, G.O. Müller, Y. C. Shen, G. Chen, S. Watanabe, W. Götz, and M. R. Krames, Appl. Phys. Lett. **91**, 243506 (2007).

[48] P. Blood, IEEE J. Quantum Elec. **36**, 354 (2000).

[49] V.I. Litvinov, J. Appl. Phys. **88**, 5814 (2000).

[50] R. J. Radtke, U. Waghmare, H. Ehrenreich, and C. H. Grein, Appl. Phys. Lett. **73**, 2087 (1998).

[51] A. Dmitriev and A. Oruzheinikov, J. Appl. Phys. **86**, 3421 (1999).

[52] F.D. Sala, A.D. Carlo, P. Lugli, F. Bernardini, V. Fiorentini, R. Scholz, and J.M. Jancu, Appl. Phys. Lett.**74**, 2002 (1999).

[53] L. Wang, C. Liu, J.N. Lu, L. Liu, N.Y. Liu, Y.J. Chen, Y.F. Zhang, E.D. Gu, and X.D. Hu, Optics Express **19**, 14182 (2011).

---

[54] B. Monemar and B.E. Sernelius, Appl. Phys. Lett. **91**, 181103 (2007).

[55] B.J. Ahn, T.S. Kim, Y. Dong, M.T. Hong, J.H. Song, Jae-Ho Song, H.K. Yuh, S.C. Choi, D.K. Bae, and Y. Moon, Appl. Phys. Lett. **100**, 031905 (2012).

[56] A. David, M.J. Grundmann, J.F. Kaeding, N.F. Gardner, T.G. Mihopoulos, and M.R. Krames, Appl. Phys. Lett. **92**, 053502 (2008).

[57] J.P. Liu, J.H. Ryou, R.D. Dupuis, J. Han, G.D. Shen, and H.B. Wang, Appl. Phys. Lett. **93**, 021102 (2008).

[58] N. F. Gardner, G.O. Müller, Y. C. Shen, G. Chen, S. Watanabe, W. Götz, and M. R. Krames, Appl. Phys. Lett. **91**, 243506 (2007).

[59] M. Maier, T. Passow, M. Kunzer, W. Pletschen, K. Köhler, and J. Wagner, Phys. Status Solidi C **7**, 2148 (2010).

[60] X .Li, S. Okur, F. Zhang, V. Avrutin, S.J. Liu, Ü. Özgür, H. Morkoç, S.M. Hong, S.H. Yen, T.S. Hsu, and A. Matulionis, J. Appl. Phys. **111**, 063112 (2012).

[61] J. Xie, Ü. Özgür, Y. Fu, X. Ni, H. Morkoç, C.K. Inoki, and T.S. Kuan, J.V. Foreman and H.O. Everitt, Appl. Phys. Lett. **90**, 041107 (2007).

[62] A.B. Yankovich, A.V. Kvit, X. Li, F. Zhang, V. Avrutin, H.Y. Liu, N. Izyumskaya, Ü. Özgür, H. Morkoç, and P.M. Volyes, J. App.Phys. 111, 023517 (2012).

[63] S. Watanabe, N. Yamada, M. Nagashima, Y. Ueki, C. Sasaki, Y. Yamada, T. Taguchi, K. Tadatomo, H. Okagawa, and H. Kudo, Appl. Phys. Lett. **83**, 4906 (2003).

[64] Y.J. Lee, C.H. Chiu, C.C. Ke, P.C. Lin, T.C. Lu, H.C. Kuo, and S.C. Wang, IEEE J. Quant. Electron. **15**, 1137 (2009).

---

[65] J.Hader, J.V. Maloney, and S.W. Koch, Appl. Phys. Lett. **96**, 221106 (2010).

[66] T. Malinauskas, A. Kadys, T. Grinys, S. Nargelas, R. Aleksiejunas, S. Miasojedovas, J. Mickevicius, R. Tomasiunas, K. Jarasiunas, M. Vengris, S. Okur, X. Li, F. Zhang, V. Avrutin, Ü. Özgür and H.Morkoç, Proc. SPIE **8262**, 82621S (2012).

[67] X.A. Cao, E.B. Stokes, P.M. Sandvik, S.F. LeBoeuf, J. Kretchmer, and D. Walker, IEEE Electron Device Lett. **23**, 535 (2002).

[68] X. Ni, X. Li, J. Lee, S. Liu, V. Avrutin, Ü. Özgür, H.Morkoç, and A. Matulionis, J. Appl. Phys. **108**, 033112 (2010).

[69] J.K. Ho, C.S. Jong, C.C. Chiu, C.N. Huang, C.Y. Chen, K.K. Shih, J. Appl. Phys. **86**, 4491 (1999)

[70] Y.C. Lin, S.J. Chang, Y.K. Su, T.Y. Tsai, C.S. Chang, S.C. Shei, S.J. Hsu, C.H. Liu, U.H. Liaw, S.C. Chen, and B.R. Huang, IEEE Photonics Tech. Lett. **14**, 1668 (2002).

[71] R.H. Horng, D.S. Wuu, Y.C. Lien, W.H. Lan, Appl. Phys. Lett. **79**, 2925 (2001).

[72] J.O Song, Kyung-Kook Kim, Hyunsoo Kim, Hyun-Gi Hong, Hyeonseok Na, and Tae-Yeon Seong, Electrochem. Solid-State Lett, **10**, H270 (2007).

[73] K.H. Choi, J.Y. Kim, Y.S. Lee and H.J. Kim, Materials Science in Semiconductor Processing, **10**, 211 (2007).

[74] C. J. Tun, J. K. Sheu, M. L. Lee, C. C. Hu, C. K. Hsieh, and G. C. Chi, J. Electrochem. Soc., **153**, G296 (2006).

[75] B.Z. Dong, G.J. Fang, J.F. Wang, W.J. Guan, X.Z. Zhao, J. Appl. Phys. **101**, 033713 (2007).

---

[76] J. Cho, J. Nah, M.S. Oh, J.H. Song, K.H. Yoon, H.J. Jung and W. K. Choi, Jpn. J. Appl. Phys., **40**, L1040 (2001).

[77] J.H. Kim, B.D. Ahn, C.H. Lee, K.A. Jeon, H.S. Kang and S.Y. Lee, J. Appl. Phys. **100**, 113515 (2006).

[78] S.R. Jeon, M.S. Cho, M.A. Yu and G.M. Yang, IEEE J. of Selected Topics in Quantum Electron, **8**, 4 (2002).

[79] J. Chu, C. Kao, H. Huang, W. Liang, C. Chu, T. Lu, H. Kuo, and S. Wang, Jpn. J. Appl. Phys. **44**, 11 (2005).

[80] X. Guo and E.F. Schubert, J. Appl. Phys. **90**, 8 (2001).

[81] Y. Yao, C. Jin, Z. Dong, Z. Sun, S.M. Huang, Displays, **28**, 129 (2007).

[82] C.S. Chang, S.J. Chang, Y.K. Su, Y.C. Lin, Y.P. Hsu, S.C. Shei, S.C. Chen, C.H. Liu, and U.H. Liaw, Semicond. Sci. Technol. **18**, L21 (2003).

[83] P. Kozodoy, S. Keller, S.P. DenBaars, and U.K. Mishra, J. Cryst. Growth, **195**, 265 (1998).

[84] T. Li, C. Simbrunner, M. Wegscheider, A. Navarro-Quezada, M. Quast, K. Schmidegg, and A. Bonanni, J. Cryst. Growth, **310**, 13 (2008).

[85] S. Hautakangas, K. Saarinen, L. Liszzkay, J.A. Freitas, Jr., and R.L. Henry, Phys. Rev. B **72**,165303 (2005).

[86] H. Kim, J. Li, S.X. Jin, J.Y. Lin, H.X. Jiang, Appl. Phys. Lett. **83**, 566 (2003).

[87] C. Bayram, J.L. Pau, R. McClintock, and M. Razeghi, **104**, 083512 (2008).

[88] D.S. Wuu, W.K. Wang, W.C. Shih, R.H. Horng, C.E. Lee, W.Y. Lin, and J.S. Fang, IEEE Photonics Technol. Lett. **17**, 288 (2005).

[89] H.W. Huang, C.H. Lin, J.K. Huang, K.Y. Lee, C.F. Lin, Mater. Sci. Eng., B **164**, 76

---

(2009).

[90] C.H. Chiu, H.H. Yen, C.L. Chao, Z.Y. Li, P. Yu, Appl. Phys. Lett. **93**, 081108 (2008).

[91] H. Gao, F. Yan, Y. Zhang, J. Li, Y. Zeng, and G. Wang, J. Appl. Phys. **103**, 014314 (2008).

# Vita

**Xing Li**
Date of Birth: Apr. 18, 1983
Citizenship: P.R. China
Email: xli.vcu@gmail.com

## EDUCATION

**Virginia Commonwealth University**, Richmond, Virginia

Electrical Engineering, Ph.D., August 2012

**Chinese Academy of Science,** Shanghai Institute of Optics and Fine Mechanics (SIOM), Shanghai, China

Material Science and Engineering, Mater of Science., July 2008

**University of Science and Technology of China**, Hefei, China

Material Science and Engineering, course study July 2006

**Wuhan University of Science and Technology**, Wuhan, China

Material Science and Engineering, B.S., July 2005

## TECHNICAL SKILLS

- Semiconductor device fabrication and processing: Photolithography/Wet Etching /Metallization /E-beam Deposition/Sputtering/Plasma Etching /Wire Bonding
- MOCVD epitaxial thin film growth
- PECVD deposition of $SiO_2$/SiNx
- Device testing: C-V, I-V, AC/DC/RF, network analyzer, LCR meter, EL, integrating sphere
- Characterizations: XRD, SEM, AFM, PL, Profilometry, Hall measurements
- Computers: Matlab, JMP, Silvaco TCAD, Origin, MSOffice

## PROFESSIONAL EXPERIENCE

**Microelectronics Materials and Device Laboratory--**Virginia Commonwealth University

- Research Assistant, 08/08 to Present
  - Fabricated and characterized GaN based RF devices: high electron mobility transistor (HEMT)

- Designed and grew HEMTs in a multiplayer project (with ***Air Force Research Lab***, ***Kyma Tech*** and ***PSU***)
- Simulated HEMT structures in Silvaco TCAD and incorporated into growth designs
- Performed small-signal parametric extractions
- Optimized plasma etching conditions and eliminated HEMT device leakage current
- Reduced specific ohmic contact resistance by one order of magnitude for HEMTs
- Optimized growth procedures and reduced sheet resistance of HEMTs by ~20% on sapphire
- Performed dominating work in a company funded project to improve high power LED performance
- Achieved high brightness LEDs (~20% brighter than the commercial one)
- Demonstrated LEDs of high quantum efficiency with negligible efficiency degradation
- Developed LED device fabrication procedures to reduce series resistance and maximize light extraction
- Simulated LED devices using Silvaco TCAD and incorporated into structure designs
- Fabricated GaN ELO structures on $SiO_2$/SiNx Distributed Bragg Reflectors (DBR) on sapphire
- Achieved crack- free semiconductor DBRs with reflectivity as high as 98% for vertical cavity laser (VCSEL)applications

**Key Laboratory for Materials of Chinese Academy of Science at SIOM** – Shanghai, China

- Research Assistant, 08/05-07/08

  Achieved room temperature magnetic semiconductor materials based on $In_2O_3$

**GE Globe Research Center** – Shanghai, China

- Project cooperator, 01/08-05/08

GaN phosphor substrate beta-$Ga_2O_3$ single crystal growth

## AWARDS

- 2011 Chinese Government Award for Outstanding Self-financed Students Abroad
- 2007 Graduate Student Award from *Shanghai-Applied Material Research and Development Fund* (AM Fund)

## KEY PUBLICATIONS

- **X. Li**, H. Morkoç, *et al.*, Improved InGaN LED quantum efficiency with multi-double-heterostructure, Appl. Phys. Lett., 101, 041115 (2012).
- **X. Li**, H. Morkoç, *et al.*, Impact of active layer design on InGaN radiative recombination coefficient and LED performance, J. Appl. Phys., 111, 063112 (2012). (Times cited: 1)
- **X. Li**, H. Morkoç, *et al.*, Efficiency retention at high current injection levels in m-plane InGaN light emitting, Appl. Phys. Lett., 95 (2009)121107. (Times Cited: 20 );
- **X. Li**, Hadis Morkoç, *et al.*, Effect of carrier spillover and Auger recombination on the efficiency droop in InGaN based blue LEDs, Superlattices and Microstructures., 47 (2010)118. (Times Cited: 6 );
- **X. Li**, H. Morkoç, *et al.*, S. M. Hong, S. H. Yen, and T.S. Hsu, On the Quantum Efficiency of InGaN Light Emitting Diodes: Effects of Active Layer Design, Electron Cooler, and Electron Blocking Layer, Phys. Status Solidi A., 208 (2011) 2907. (Times Cited: 4 );
- **X. Li**, H.Y. Liu, S. Liu, X. Ni, M. Wu, V. Avrutin, N. Izyumskaya, Ü. Özgür, and H. Morkoc, InGaN based Light emitting diodes with Ga doped ZnO as transparent conducting oxide, Phys. Status Solidi A., 207 (2010) 1993. (Times Cited: 10 );
- **X. Li**, X. Ni, H.Y. Liu, F. Zhang, S. Liu, J. Lee, Ü. Özgür, and H. Morkoç, T. Paskova, G. Mulholland, and K.R. Evans, On the reduction of efficiency loss in polar c-plane and non-polar m-plane InGaN light emitting diodes, Phys. Status Solidi C., 8 (2011) 1560. (Times Cited: 1 )
- Ü. Özgür, H.Y. Liu, **X. Li**, X. Ni, H. Morkoç, GaN based light emitting diodes: efficiency at high injection levels, Proceedings of IEEE, 98 (2010) 1180. (Times Cited: 20 );

- X. Ni, **X. Li**, J. Lee, S.Liu, Avrutin. V, Ü. Özgür, H. Morkoç, A. Matulionis, Hot electron effects on efficiency degradation in InGaN light emitting diodes and designs to mitigate them, J. Appl. Phys., 108 (2010)033102 (Times Cited: 13 );
- X. Ni, **X. Li**, J. Lee, S.Liu, Avrutin. V, Ü. Özgür, H. Morkoç, A. Matulionis, InGaN staircase electron injector for reduction of electron overflow in InGaN light emitting diodes, Appl. Phys. Lett, 97 (2010) 031110 (Times Cited: 12);
- J. Lee, **X. Li**, X. Ni, Ü. Özgür, H. Morkoç, T. Paskova, G. Mulholland, and K.R. Evans, On carrier spillover in c- and m-plane InGaN light emitting diodes, Appl. Phys. Lett, 95 (2009) 201113 (Times Cited: 14);
- **X. Li**, Xia CT, S, Pei, He XL, Synthesis and characterization of room-temperature ferromagnetism in Fe- and Ni-co-doped In2O3, J. PHYSICS AND CHEMISTRY OF SOLIDS, 68 (2007) 1836-1840. (Times Cited: 13 );
- **X. Li**, C.T. Xia, X.L. He, G.Q. Pei, J.G. Zhang, J. Xu, Study on nitridation processes of beta-Ga2O3 single crystal, CHINESE OPTICS LETTERS, 6 (2008) 282-285. (Times Cited: 6 );
- **X. Li**, Xia CT, He, XL, Gao, X, Liang, S, Pei, GQ, Dong, YJ, Enhancement of ferromagnetic properties in In1.99Co0.01O3 by additional Cu doping, SCRIPTA MATERIALIA, 58 (2008) 171-174. (Times Cited: 6 );
- A. B. Yankovich, A. V. Kvit, **X. Li**, F. Zhang, V. Avrutin, H. Y. Liu, N. Izyumskaya, Ü. Özgür, H. Morkoç, and P. M. Voyles, hexagonal based pyramid void defects in GaN and InGaN, J. Appl. Phys., 111 (2012) 023517.
- Leach J.H, Ni. X**, Li. X**, Ü. Özgür, H. Morkoç, Bias dependent two channel conduction in AlInN/AlN/GaN structures, J. Appl. Phys., 107 (2010) 083706. (Times Cited: 4 )
- M. Wu, **X. Li**, Ü. Özgür, and H. Morkoç, *et al.*, AlGaN/GaN dual channel HFET: Impaction on the optimal sheet density, submitted to Appl. Phys. Lett.

- J.H. Leach, M. Wu, **X. Li**, H. Morkoç *et al.*, Effect of lattice mismatch on gate lag in high quality InAlN/AlN/GaN HFET structure, Physica Status Solidi (a), 207, 211 (2010). (Times cited: 12)
- J.H. Leach, M. Wu, X. Ni, **X. Li**, H. Morkoç, *et al.*, Carrier velocity in InAlN/AlN/GaN HFETs on Fe-doped bulk GaN substrates, Appl. Phys. Lett., 96, 102109 (2010). (Times cited: 5)
- C. Kayis, R.A. Ferreyra, M. Wu, **X. Li**, Ü. Özgür, and H. Morkoç, *et al.*, Degradation in AlInN/AlN/GaN HFETs as monitored by low frequency noise measurements: hot phonon effects, Appl. Phys. Lett., 99, 063505 (2011). (Times cited: 3)
- C. Kayis, J.H Leach, C.Y. Zhu, M. Wu, **X. Li**, Ü. Özgür, and H. Morkoç, *et al*, Low frequency noise measurements of AlGaN/GaN metal-oxide-semiconductor heterostructure field effect transistors with HfAlO gate dielectric, IEEE Electron Device Lett., 31, 1041 (2010). (Times cited: 6)